AN EFFICIENT METHOD FOR FRACTURED SHALE RESERVOIR SIMULATION & HISTORY MATCHING: THE cEDFM APPROACH

A Dissertation

by

ZHI CHAI

Submitted to the Office of Graduate and Professional Studies of
Texas A&M University
in partial fulfillment of the requirements for the degree of

DOCTOR OF PHILOSOPHY

Chair of Committee,	John E. Killough
Committee Members,	I. Yucel Akkutlu
	Eduardo Gildin
	Maria A. Barrufet
Head of Department,	Jeff Spath

December 2018

Major Subject: Petroleum Engineering

ABSTRACT

The intricate physics of unconventional reservoir fluid transportation has posed great challenges to traditional simulation approaches. Resources such as shale are usually associated with complex fracture networks generated either naturally as a result of the geo-stress evolution, or artificially during hydraulic fracturing to improve well productivity. In either case, fractures greatly influence the underground fluid transportation, which highlights the importance to accurately simulate the flux with fractures. In this work, a novel discrete fracture model, compartmental EDFM (cEDFM) is developed based on the original EDFM framework. By assuming a linearly distributed pressure near fractures, EDFM can provide a sub-grid resolution that lifts the requirement to perform local refinement. Although efficient, considerable error is reported when applying this method to simulate flow barriers, especially when dominant flux direction is across instead of along the fractures. Therefore, different from the original method, the fracture would split matrix grid blocks when intersecting them in the proposed approach, resulting in a model more similar to an explicit fracture model. The proposed method maintained the high efficiency of the original EDFM, while overcame some of the limitations. The new model is benchmarked for single-phase and multi-phase problems, and the accuracy is evaluated by comparing to multiple reference cases. Results indicate the new model yields much better accuracy even for multi-phase flow simulation with flow barriers.

A major part of the uncertainty for shale reservoirs comes from the distribution and properties of the fracture network. However, explicit fracture models are rarely used in uncertainty quantification due to the high computational cost. The later part of this work explored several

workflows to match the history of reservoirs with fractures. By taking advantage of the efficiency of cEDFM, fractures can be explicitly characterized, and the corresponding uncertainty about the distribution and properties of fractures can be evaluated. No upscaling of the fracture properties is necessary, which is usually a required step in a traditional workflow. A modified two-stage MCMC algorithm as well as the Ensemble Kalman Filter (EnKF) are implemented as the data assimilation algorithms, with the latter preferred for more complex cases with larger parameter space.

DEDICATION

To my family.

ACKNOWLEDGEMENTS

As my study in college station comes to an end, I'd like to express my gratitude to everyone who helped me along the way. It would not have been possible to complete this work without their encouragement and help.

My deepest gratitude goes to my advisor Dr. John E. Killough for his guidance of my research work. His immense knowledge in reservoir simulation cleared up many obstacles for me throughout the progress of this work. He is always supportive and allow me to pursue what I'd like to in my research and study. His support, spiritually as well as financially, makes this work possible.

I would like to thank Dr. Yucel Akkutlu for his valuable feedback at different stages of my research. I would like to thank Dr. Eduardo Gildin for his comment about this work. His numerical reservoir simulation class helped to build the foundation in reservoir simulation for me. I would also like to thank Dr. Maria A. Barrufet for all the suggestions to improve this work.

I would like to express my gratitude for the financial support from Crisman Institute for Petroleum Research for this project.

My special thanks go to all the colleagues in Killough group and all my friends. It is your company that makes life enjoyable here.

Finally, I would like to thank my family, especially my parents, for their unconditional love and support over the years of my study.

CONTRIBUTORS AND FUNDING SOURCES

This work was supported by a dissertation committee consisting of Professor John Killough, Professor I. Yucel Akkutlu and Professor Eduardo Gildin of the Department of Petroleum Engineering and Professor Maria A. Barrufet of the Department of Chemical Engineering.

This study was funded by Crisman Institute for Petroleum Research from the Petroleum Engineering Department of Texas A&M University.

NOMENCLATURE

$d_{f_i l}$: distance to the shared edge from the centroid of the fracture polygon, ft

$\overline{d_{f_i l}}$: average distance to the fracture intersection line, ft

d_{NNC} : characteristic distance of non-neighbor connection, ft

d_{obs} : observed well data

d_{sl} : distance to the fracture intersection line, ft

d_{vf} : distance to the fracture plane, ft

g_n : well data vector

$g(x)$: simulated reservoir response

$g^*(x)$: interpolated reservoir response with proxy model

k_f : fracture permeability, md

k_m : matrix permeability, md

k_r : relative permeability

$\bar{k}_{mn}$: inter-porosity effective permeability, md

k_{NNC} : effective permeability of non-neighbor connection, md

$l_{f_i f_j}$: length of intersection line between two fracture grids, ft

m : model parameters vector

m_i : adsorbed mole of component i per matrix bulk volume, $mole/ft^3$

n : number of normal sets of fractures

n_h : number of components in the oil and gas phase

$nCells$: number of cells of the reservoir model

$nWells$: number of wells of the reservoir model

$q(\cdot)$: proposal distribution at the 1st stage

q_{m-n} : inter porosity flux rate between porosity m and n, $mole/s$

$q_{o/g/w}^{W}$: volumetric production/injection rate of well W per bulk volume, s^{-1}

r_i : residue of component i

$s_{o/g/w}$: phase saturation

t : time, s

u_n : state variable vector

w_f : fracture aperture, ft

x_i : oil phase mole fraction of component i

y_i : gas phase mole fraction of component i

y_n : model state vector

$A_{fracture}$: area of the fracture segment, ft^2

A_{NNC} : area of non-neighbor connection, ft^2

C_D : covariance matrix of observed well data

C_x : covariance matrix of model parameters

F : flow simulation

G : sensitivity matrix of reservoir response to model parameters

K_n : Kalman gain matrix at time step n

L : characteristic length of matrix for the dual porosity model, ft

$M_{i,j}$: adsorbed mole of component i in grid j, $mole$

$N_{i,j}$: mole of component i in grid j, $mole$

N_e : ensemble size

$N_{w,j}$: mole of water in grid j, $mole$

P : posterior probability calculated with $g(x)$

P^* : posterior probability calculated with $g^*(x)$

P_L : Langmuir pressure of a component, $psia$

$P_{o/g/w}$: phase pressure, $psia$

P_{wf} : well bottom-hole pressure, $psia$

PV_j : pore volume of grid j, ft^3

$Q(\cdot)$: proposal distribution at the 2nd stage

$Q_{o/g/w}^W$: volumetric production/injection rate of well W at the perforation grid, ft^3/s

R : covariance matrix of the observation errors

$R_{i,j}$: CVFD format residue of component i in grid j

T_{j-c} : transmissibility between control volume j and c, $md \cdot ft$

T_{m-n} : inter-porosity transmissibility between porosity types m and n, $md \cdot ft$

V_j : bulk volume of grid j, ft^3

V_L : Langmuir volume of a component, ft^3/lb

$V_{o/g/w,j}$: volume of oil/gas/water phase in grid j, ft^3

α : unit conversion coefficient

ϕ : porosity

σ_{mn} : shape factor between porosity type m and n

ρ	:	phase density, lb/ft^3
ρ_s	:	rock bulk mass density, lb/ft^3
$\tilde{\rho}$	:	phase mole density, $mole/ft^3$
$\lambda_{o/g/w}$	:	phase mobility, md/cp
$\lambda_{ro/rg/rw}$	:	relative phase mobility, cp^{-1}
τ_{mf}	:	inter-porosity flux rate per unit bulk volume, $lb/ft^3/s$
μ	:	viscosity, cp
Φ	:	phase potential, $psia$
$\Phi_{no/ng}$	:	oil/gas phase potential for porosity type n, $psia$

Subscripts:

c	:	neighbor index from the connection list
f	:	fracture
g	:	gas phase
i	:	component index
j	:	control volume index
m	:	matrix
n	:	time step index
o	:	oil phase
p	:	phase index
w	:	water phase
x	:	x direction
y	:	y direction
z	:	z direction

Superscripts:

W	:	Index of a well
sc	:	standard condition

ABBREVIATIONS

BHP	:	bottom-hole pressure
cEDFM	:	compartmental embedded discrete fracture model
CVFD	:	control volume finite difference
CPG	:	corner-point grid
DFM	:	discrete fracture model
DFN	:	discrete fracture network
EDFM	:	embedded discrete fracture model
EnKF	:	ensemble Kalman filter
EnRML	:	ensemble randomized maximum likelihood
ES	:	ensemble smoother
GA	:	genetic algorithm
GOR	:	gas-oil ratio
GURU	:	general unstructured reservoir utility
LGC	:	local grid coarsening
LGR	:	local grid refinement
MCMC	:	Markov chain Monte Carlo
MFD	:	mimetic finite difference
MINC	:	multiple interacting continua method
PEBI	:	perpendicular bisector
PVI	:	pore volume injection
SRV	:	stimulated reservoir volume
TPFA	:	two-point flux approximation
VLE	:	vapor-liquid equilibrium

TABLE OF CONTENTS

Page

ABSTRACT ii

DEDICATION iv

ACKNOWLEDGEMENTS v

CONTRIBUTORS AND FUNDING SOURCES vi

NOMENCLATURE vii

ABBREVIATIONS xi

TABLE OF CONTENTS xii

LIST OF FIGURES xv

LIST OF TABLES xxii

CHAPTER I INTRODUCTION 1

1.1 Fractured Reservoir Characterization 1

1.2 Research Objectives 4

1.3 Chapter Overview 4

CHAPTER II LITERATURE REVIEW 6

2.1 Fractured Reservoir Simulation 6

2.2 Fractured Reservoir History Matching 11

CHAPTER III GENERAL UNSTRUCTURED RESERVOIR UTILITY (GURU) 15

3.1 Overview 15

3.2 Governing Equations 16

3.3 Multiple-Porosity Model 18

3.4 Model Definition 20

CHAPTER IV COMPARTMENTAL EMBEDDED DISCRETE FRACTURE MODEL (cEDFM) 22

4.1 Overview 22

4.2 Limitation of EDFM 23

4.3 Compartmental EDFM 24

4.3.1 Model Schematics 24

4.3.2 None-neighbor Connections 27

4.3.3 Generalized Transmissibility for Unstructured Sub-grids 30

4.3.4 Grid Data Structure 32

4.4 Local Grid Coarsening 33

4.5 Corner Point Extension 36

CHAPTER V MODEL VERIFICATION OF cEDFM 38

5.1 Case Benchmarking for Single-Phase Flow Problem 38

5.2 Case Benchmarking for Two-Phase Flow Problem 40

5.2.1 Case with Orthogonal Fractures 43

5.2.2 Case with Skewed Fractures 44

5.3 Complex Horizontal Well Case Benchmarking with PEBI 46

5.4 Sensitivity Analysis 48

CHAPTER VI CASE STUDIES 51

6.1 Naturally Fractured Shale Reservoir 51

6.2 Horizontal Well Optimization with cEDFM 56

6.3 Dynamic Fracture Network 60

CHAPTER VII FRACTURED RESERVOIR HISTORY MATCHING WITH MCMC 66

7.1 Markov Chain Monte Carlo (MCMC) 67

7.2 Two-Stage MCMC 69

7.3 Generate the Proxy Model 70

7.4 Case Study 72
7.5 Summary 81

CHAPTER VIII FRACTURED RESERVOIR HISTORY MATCHING WITH ENKF 83
8.1 The Ensemble Approach for History Matching 83
8.2 Case Study 85
8.2.1 Model Parameterization 85
8.2.2 Case I: Locating Highly Conductive Fractures 87
8.2.3 Case II: Locating Impermeable Flow Barriers 90
8.3 Summary 93

CHAPTER IX DISCUSSIONS & CONCLUSIONS 94

REFERENCES 96

LIST OF FIGURES

Page

Figure 2.1—Idealization of the heterogeneous porous medium, Warren, J. E., & Root, P. J. (1963). 8

Figure 2.2—Discretization of matrix blocks (schematic): (a) MINC (b) dual-porosity (c) explicit discretization. Wu, Y.-S., & Pruess, K. (1988). 9

Figure 3.1—Mass transfer pyramid among different porosity types of shale reservoirs. Modified from Yan, B. et al. (2016). 20

Figure 3.2—Cell and Connection class of GURU in pseudo code, from Yan, B. (2017). 21

Figure 4.1—Schematic of the difference between EDFM and cEDFM for a simple case: single matrix cell intersected by a fracture. The fracture cell is denoted in red, and the background color corresponds to the pressure profile in the matrix. 25

Figure 4.2—Pseudo-fracture extension at the fracture tips. (a) 1×2 grids intersected by 2 fractures. The contact area between M_{12} and M_{21} cannot be defined by any grid faces. (b) Pseudo-fracture added to further split matrix grids into conforming forms. 26

Figure 4.3—Illustration of the cEDFM scheme: (a): discretization of 2×2 grids intersected by 2 fractures; (b): connection map of the model, 5 types of non-neighbor connections (NNCs) defined. $NNC-I$: connection between matrix sub-grid and fracture grid; $NNC-II$: connection between two intersecting fracture grids; $NNC-III$: connection between two neighbor fracture grids of the

same fracture; $NNC - IV$: connection between two sub-grids or one sub-grid and one un-split grid; $NNC - V$: connection between two matrix sub-grids separated by a pseudo-fracture. 27

Figure 4.4—The computation of NNC Type-I is modified by only integrating over the sub-grids to calculate d_{NNC}. 28

Figure 4.5—Tetrahedralization of a partial grid. The polygon at the bottom indicates one of the faces of the grid, with C_f denoting the centroid of the face. C_g denotes the centroid of the entire grid. 5 tetrahedrons are generated, with the four vertices being C_f, C_g, and two vertices of an edge. 28

Figure 4.6—Scheme to establish $NNC - IV$ between neighboring sub-grids from different parent grid blocks. A binary identifier string is generated based on the spatial relationship of the sub-grid centroid and the fractures. Sub-grids with same identifier string are connected, as marked in double arrows. 30

Figure 4.7—Possible intersections of a slant fracture plane and an orthogonal matrix grid. The fracture grid can be a triangle, quadrilateral, pentagon, or hexagon (Modified from Moinfar, A. et al., 2014). 32

Figure 4.8—Data structure of the Grid object in pseudo code. 33

Figure 4.9—Eliminating small cells by merging close-by nodes. 33

Figure 4.10—Automatic local grid coarsening of cEDFM in unfractured areas. 35

Figure 4.11—Well production curves of cEDFM with and without LGC. 36

Figure 4.12—Pressure profile of the synthetic Brugge reservoir with 5 horizontal wells. 6 stages of hydraulic fractures for each well simulated with 1050 discrete fractures in total. 37

Figure 5.1—Case with highly conductive fractures: normalized pressure profile with CO_2 flooding, $PVI = 0.5$. 39

Figure 5.2—Case with highly conductive fractures: error map of normalized pressure with CO_2 flooding, $PVI = 0.5$. 39

Figure 5.3—Case with flow barriers: normalized pressure profile with CO_2 flooding, $PVI = 0.5$. 40

Figure 5.4—Case with flow barriers: error map of normalized pressure with CO_2 flooding, $PVI = 0.5$. 40

Figure 5.5—Logarithmic permeability map of the benchmarking cases. Highly conductive fractures and low conductive flow barriers coexist in both cases. 41

Figure 5.6—Parent Grid of cEDFM for Case I. Locations of the fractures are marked in black. 42

Figure 5.7—Parent Grid of cEDFM for Case II. Locations of the fractures are marked in black. 42

Figure 5.8—Case comparison: normalized pressure profile of orthogonal fracture water flooding, $PVI = 0.5$. 43

Figure 5.9—Case comparison: water saturation profile of orthogonal fracture water flooding, $PVI = 0.5$. 43

Figure 5.10—Error map of normalized pressure, orthogonal fracture water flooding, $PVI = 0.5$. 44

Figure 5.11—Error map of water saturation, orthogonal fracture water flooding, $PVI = 0.5$. 44

Figure 5.12—Case comparison: normalized pressure profile of skewed fracture water flooding, $PVI = 0.4$. 44

Figure 5.13—Case comparison: water saturation profile of skewed fracture water flooding, $PVI = 0.4$. 45

Figure 5.14—Error map of normalized pressure, skewed fracture water flooding, $PVI = 0.4$. 45

Figure 5.15—Error map of water saturation, skewed fracture water flooding, $PVI = 0.4$. 46

Figure 5.16—Pressure Profile for a horizontal well case with 24 stages of hydraulic fractures and 248 natural fractures. Pressure profile after 5 years of production. PEBI model from Sun, J. et al. (2014). 47

Figure 5.17—Well production rate of the 3 different models. 48

Figure 5.18—Sensitivity to parent matrix mesh: C_1 concentration after 12 months of CO_2 flooding. 50

Figure 6.1—Large-scale natural fracture distribution. More active natural fractures within the SRV of the well. 51

Figure 6.2—Pressure profile of micro fractures for a hydraulic fractured horizontal well completed in shale formation. 53

Figure 6.3—Pressure profile of inorganic matrix for a hydraulic fractured horizontal well completed in shale formation. 54

Figure 6.4—Pressure profile of kerogen for a hydraulic fractured horizontal well completed in shale formation. 55

Figure 6.5—Model illustration of the optimization case. 56

Figure 6.6—Horizontal well design optimization workflow with GA. 58

Figure 6.7—Net present value of the optimal case vs. generation. 59

Figure 6.8—Compaction curve of propped fracture conductivity. 61

Figure 6.9—Compaction curve of unpropped fracture conductivity. 61

Figure 6.10—Pressure profile after 10 years of production. 63

Figure 6.11—Cumulative gas production with different compaction coefficient α. 64

Figure 6.12—Cumulative gas production with different percentage of effectively propped fractures. 64

Figure 7.1—Flowchart of history matching and uncertainty quantification of fractured shale reservoirs with cEDFM. 67

Figure 7.2—Example case reservoir model. Single horizontal well with 10 stages of hydraulic fractures (in red) and the interacting natural fractures (in blue). Uncertainty is introduced from the distribution and conductivity of the natural fractures, as well as the properties of the shale matrix. 72

Figure 7.3—Prior PDF and true value for the reference case. 74

Figure 7.4—Tornado plot of cumulative oil production with respect to model parameters. 75

Figure 7.5—Neural Network set-up for training the proxy model. 76

Figure 7.6—Well data mismatch (likelihood) from the proxy model vs. full simulation. 77

Figure 7.7—Objective function along the MCMC chain. 78

Figure 7.8—Boxplot of the parameters along the MCMC chain, with each box representing 100 accepted samples. 79

Figure 7.9—Box plot of the parameters from the prior distribution vs. posterior distribution. True values of the parameters are marked with red asterisks as a reference. 80

Figure 7.10—Histogram of the model parameters from the accepted samples. 80

Figure 7.11—History matching result of the well data. 81

Figure 8.1—History matching case: 9-spot well pattern with 1 injector at the center. 85

Figure 8.2—Case I: Fracture locations at different assimilation time steps of EnKF. 87

Figure 8.3—Case I: Water saturation at T=12 months for 3 random realizations in the ensemble during different assimilation steps. The reference case is shown on the right. 88

Figure 8.4—Case I: Oil and water production rate before and after history matching. Initial results are shown on the left, and the results afterward are shown on the right. The first 8 months of data are used for history matching, shown in red; model prediction results are shown in blue. 89

Figure 8.5—Case II: Fracture locations at different assimilation time steps of EnKF. 90

Figure 8.6—Case II: Water saturation at T=12 months for 3 random cases in the ensemble during different assimilation steps. The reference case is shown on the right. 91

Figure 8.7—Case II: Oil production rate before and after history matching. Initial results are shown on the left, and the results afterward are shown on the right. The first 8 months of data are used for history matching, shown in red; model prediction results are shown in blue. 92

LIST OF TABLES

Page

Table 4.1—EDFM formulation. 23

Table 4.2—cEDFM formulation. 31

Table 4.3—Model parameters for LGC case comparison. 35

Table 5.1—Model parameters for the single-phase flow problem. 38

Table 5.2—Model parameters for the two-phase flow problem. 41

Table 5.3—Model parameters for the complex fracture network problem. 46

Table 5.4—Model parameters for sensitivity analysis. 49

Table 6.1—Model parameters for the multiple-porosity shale problem. 52

Table 6.2—Parameters for NPV calculation. 57

Table 6.3—Well design optimization results. 59

Table 6.4—Model parameters for the dynamic fracture conductivity case. 62

Table 7.1—Prior distribution and reference value of the example case. 73

Table 8.1—Reservoir parameters for the history matching case. 86

CHAPTER I

INTRODUCTION

1.1 Fractured Reservoir Characterization

For unconventional resources such as shale reservoirs, the fracture network critically affects the performance of the wells. Hydraulic fractures greatly increase the contact between the well and the reservoir, and create the stimulated reservoir volume (SRV) near the wellbore. Large-scale natural fractures can further increase the volume of SRV when effectively intersected with hydraulic fractures. These macro fractures largely determine the well production and the final recovery of shale reservoirs. The problem becomes even more imperative for multi-phase flow cases, where fractures may form high conductive flow corridors, which leads to unexpected high water cut and high gas-oil ratio (GOR) for some reservoirs. Therefore, it is essential to accurately simulate the fluid transportation in fractures and between fracture and the shale matrix in order to correctly capture the production dynamics.

Many different approaches have been proposed for the simulation of fractured reservoirs, and one of the earliest and most widely applied models is the dual continuum model. This approach treats fractures as a continuous porosity type. Therefore, instead of representing the fractures explicitly in the reservoir model, fracture properties are upscaled. This approach is very attractive for cases with small-scale fractures that are well connected, since the upscaling procedure simplifies the model greatly and make this approach very efficient. However, obvious errors could be observed for cases with large-scale fractures dominating the flow.

Due to the limited accuracy of the dual continuum models for many field applications, alternative approaches need to be considered. Different discrete fracture models (DFM) have been proposed by many researchers to improve the accuracy. With this type of model, fractures are

represented explicitly, and unstructured grids are usually needed to conform to the geometry of the fractures. Local grid refinement is also necessary for this kind of model to ensure accuracy, as a result, the number of grid blocks is usually very large, especially for 3D cases. The most widely used DFM is usually based on the perpendicular bisector (PEBI) model. This approach ensures the flux direction between neighbor grid blocks is perpendicular to the grid boundary, therefore two-point flux approximation (TPFA) can suffice to ensure the simulation accuracy. DFM has a much-improved accuracy compared to dual continuum approaches, however due to the complexity to generate this type of model, as well as the associated higher computational cost, it hasn't been widely used in the industry.

Another model that has drawn a lot of attention lately is the embedded discrete fracture model (EDFM). This approach represents fractures explicitly, but different from DFMs, no local grid refinement (LGR) is required for this approach. This is because the transmissibility between the fracture grid and the matrix is derived similarly as the well index in conventional reservoir simulation. A sub-grid resolution can be obtained by assuming a linear flow near the fractures perpendicular to the fracture plane, therefore the requirement for LGR is lifted. The matrix can be discretized first without the need to conform to fracture geometry, then the fracture is naturally discretized by the boundary of the matrix grid blocks. The EDFM approach has shown great accuracy and efficiency based on the results from many previous works. However, due to the way fractures are incorporated into the reservoir model, significant errors might occur for cases with across fracture flux, especially for low permeable filled fractures that form flow barriers. Therefore, in this study, we developed a new model named compartmental EDFM (cEDFM) based on the original EDFM framework to improve the accuracy under these circumstances. Meanwhile,

since the original EDFM only work for orthogonal grids, the cEDFM approach is further extended to be applicable to corner-point grid block models.

Due to the large uncertainty of the fracture distribution, especially for natural fractures, the production behavior might differ drastically. Therefore, it is important to understand the uncertainty associated with the fracture networks. A possible way to characterize the fractures is with core data, well logging data, or seismic data. However, these data are either sparse in nature and cannot be used to determine the exact location of fractures, or low in accuracy due to its limited quality. An alternative approach is to use production data and characterize the fractures through history matching. To our best knowledge, almost all previous studies on fractured reservoir history matching require to perform upscaling to generate the reservoir model. However, different upscaling algorithms may lead to a very different upscaled model, and the dual continuum approach has a limited accuracy for cases with large fractures. Therefore, in this study, we try to use explicit model directly in history matching. There are a couple of benefits for doing this. First is that we have a more accurate forward model, and the history matching result is more intuitive to be interpreted. Another is that we can maintain the Gaussian distribution for the parameters that specify the property and geometry of the fractures, which is a prerequisite for many data assimilation algorithms. There are a couple of challenges in terms of fractured reservoir history matching. The first is the efficiency and accuracy of the forward model. The cEDFM approach has demonstrated a good performance and efficiency that thousands or more simulation runs are feasible, which is a common case in history matching. Another problem is that due to the high non-linearity compared to conventional cases without fractures, the performance of many data assimilation algorithm may deteriorate. Multiple approaches have been tested in this work, including an improved Markov chain Monte Carlo (MCMC) approach, as well as the Ensemble

Kalman Filter (EnKF) approach. The MCMC approach works well for cases with a limited number of parameters. For more complex cases, we showed that the EnKF algorithm is more practical and gives good results, even for cases with large uncertainties and poor initial guess. In all cases, the cEDFM approach demonstrated satisfactory robustness to be used directly in history matching.

1.2 Research Objectives

The objectives of this work, based on the problems discussed above, are as follows:

1) Develop a new model based on the original EDFM formulation that has an improved accuracy for across fracture flux.
2) Extend the model to work with corner-point grids so that it is applicable to real field cases. Since the discretization of fractures is only performed after the matrix discretization is performed, the developed cEDFM approach should be applicable to any existing reservoir models that are based on corner-point gridding or simply orthogonal gridding.
3) Further reduce the computational cost for fractured reservoir simulation by incorporating automatic local grid coarsening to the proposed model.
4) Study appropriate algorithms for fractured reservoir automatic history matching, incorporate the proposed explicit model into the workflow.

1.3 Chapter Overview

The organization of the dissertation is as follows: The 1st chapter provides the general background and area of study of this work; The 2nd chapter gives a detailed review of the previous work on fractured reservoir simulation and related history matching techniques; The 3rd chapter introduces the in-house simulator, the equation solved, as well as some adaptation in order to work with the fracture modeling approach discussed in the following chapters; The 4th chapter discusses the limitation of the original EDFM approach, methodology for the cEDFM approach, and the

other improvements made to the model; The 5th chapter shows the result of model benchmarking; The 6th chapter includes several case studies with the new cEDFM approach; The 7th and 8th chapter discuss the application of the model in automatic history matching with different algorithms; Finally, the last chapter summarizes the work and discusses some conclusions drawn from this study.

CHAPTER II

LITERATURE REVIEW

2.1 Fractured Reservoir Simulation

The forward models for fractured reservoir simulation can be generally classified into two categories: the continuum medium approach and the explicit fracture model approach. The continuum medium approach was firstly introduced by Warren, J. E. and Root, P. J. (1963) to reservoir simulation applications. In their work they proposed the classic dual-porosity model for fractured reservoir simulation, and it was later extended to multiple-porosity model by Hinkley, R. et al. (2013) and Yan, B. et al. (2013) to account for more complex physics in shale reservoirs. This type of approach does not represent the geometry of fractures explicitly. Instead, fractures are represented as a continuous medium, and the flux between fracture and the matrix is determined by a "shape factor". As shown in **Figure 2.1**, the actual reservoir is idealized to a sugar cube model, in which matrix acts as the source of the fractures. The mathematical model for the dual continuum approach can be written as:

$$\nabla\left(\rho_p \frac{\alpha k_f k_{rp}}{\mu_p} \nabla\Phi_p\right)_f + \tau_{mf-p} = \frac{\partial}{\partial t}\left(\rho_p \phi s_p\right)_f \quad \text{.....(2.01)}$$

$$\nabla\left(\rho_p \frac{\alpha k_m k_{rp}}{\mu_p} \nabla\Phi_p\right)_m - \tau_{mf-p} = \frac{\partial}{\partial t}\left(\rho_p \phi s_p\right)_m \quad \text{.....(2.02)}$$

where: the first term is the flux term, in which α is the unit conversion coefficient, and the second term is the inter-porosity flux term from the matrix to fracture for phase p. Note that for the original dual-porosity model, the flux is assumed to be zero between different matrix blocks, therefore the first term in the matrix equation is zero. However, in cases where the computational grid is smaller than the matrix grid, this assumption would not be appropriate. Therefore, Blaskovich, F. T. et al. (1983), Hill, A. C., & Thomas, G. W. (1985), and Dean, R. H., & Lo, L. L. (1988) proposed the

dual-permeability model that considered matrix to matrix flow, the flow equations are as shown above with a non-zero first term in the matrix equation.

Multiple approaches have been proposed on how to calculate the shape factor, such as in Warren, J. E. & Root, P. J. (1963), Kazemi, H. et al. (1976, 1992), Coats, K. H. (1989), and Lim, K. T., & Aziz, K. (1994). The Warren and Root shape factor is defined as:

$$\sigma = \frac{4n(n+2)}{L^2} \quad \text{.....(2.03)}$$

where: n is the number of normal sets of fractures, n=1, 2, 3. L is the characteristic length of matrix blocks, defined as:

$$L = L_x, \qquad for\ n = 1 \quad \text{.....(2.04)}$$

$$L = \frac{2L_xL_y}{L_x+L_y}, \qquad for\ n = 2 \quad \text{.....(2.05)}$$

$$L = \frac{3L_xL_yL_z}{L_xL_y+L_xL_z+L_yL_z}, \qquad for\ n = 3 \quad \text{.....(2.06)}$$

where: L_x, L_y, L_z are the size of the matrix blocks in x, y, z directions. Kazemi derived the shape factor for a 3D case with finite difference approach, the formulation is given by:

$$\sigma = 4\left(\frac{1}{{L_x}^2} + \frac{1}{{L_y}^2} + \frac{1}{{L_z}^2}\right) \quad \text{.....(2.07)}$$

Coats considered pseudo-steady state diffusion between matrix and fractures, and the result is exactly twice as Kazemi's, given by:

$$\sigma = 8\left(\frac{1}{{L_x}^2} + \frac{1}{{L_y}^2} + \frac{1}{{L_z}^2}\right) \quad \text{.....(2.08)}$$

By avoiding the pseudo-steady state assumption, Lim & Aziz derived a new shape factor as:

$$\sigma = \pi^2\left(\frac{1}{{L_x}^2} + \frac{1}{{L_y}^2} + \frac{1}{{L_z}^2}\right) \quad \text{.....(2.09)}$$

They showed in their work that the pseudo-steady state assumption isn't appropriate, and by eliminating it, their formulation obtained an improved accuracy.

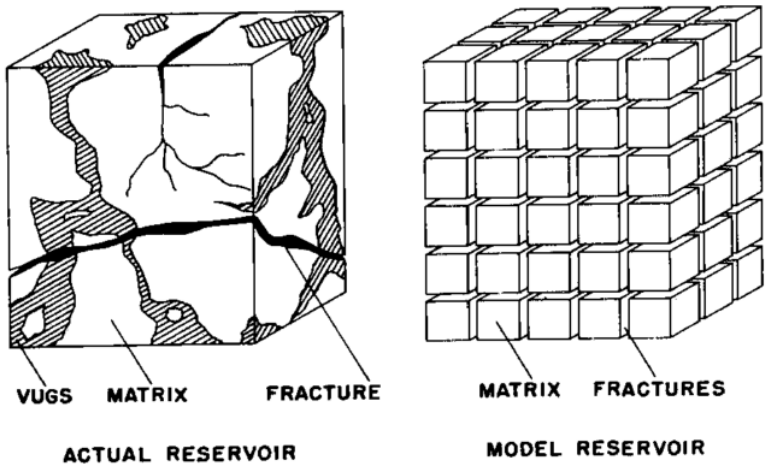

Figure 2.1—Idealization of the heterogeneous porous medium, Warren, J. E., & Root, P. J. (1963).

One problem with the dual-porosity / dual permeability model is that an averaged pressure and saturation are used for all matrix grids within a whole computational grid block, leading to an inaccurate pressure difference between the matrix and the fracture medium. To address this problem, another model named multiple interacting continua method (MINC) was proposed by Pruess, K. & Narasimhan, T.N. (1985). By assuming that the matrix with the same distance to the fracture has the same potential, the reservoir can be discretized into a series of nested volumes. The method permits a full transient flux between the matrix and fracture. Wu, Y.-S., & Pruess, K. (1988) applied MINC to field waterflooding cases in naturally fractured reservoirs, and their result indicates an improved accuracy compared to the dual-porosity approach. A comparison of the discretization schemes of different dual continuum models is shown in **Figure 2.2**.

Since models based on the dual continuum approaches were derived based on very specific assumptions, it is only suitable for cases with more uniform fracture distribution. However, real field data has suggested that these assumptions is far from being accurate in many cases, based on studies such as Gillespie, P. A. et al. (1993), Ouillon, G. et al. (1996), Aarseth, E. S. et al. (1997),

Odling, N. E. et al. (1999) and Gale, J. F. et al. (2014). A significant error might be observed for cases with large-scale fractures dominating the flow.

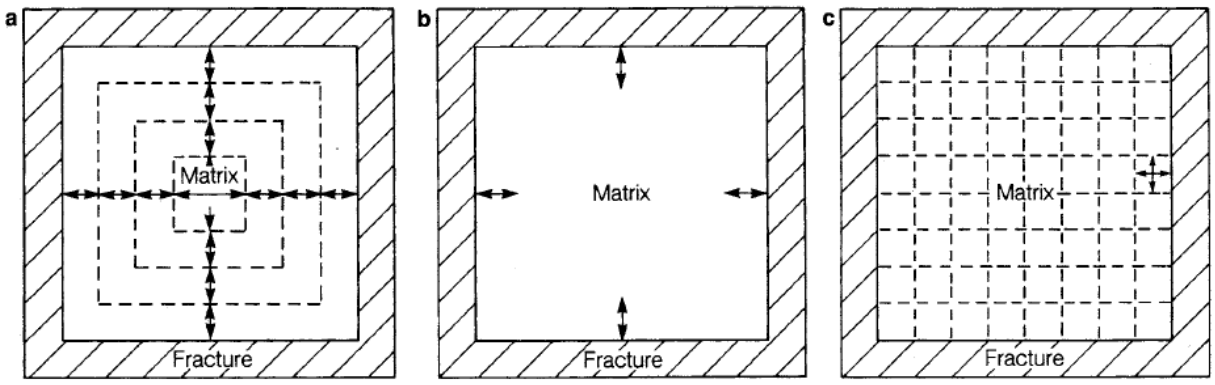

Figure 2.2—Discretization of matrix blocks (schematic): (a) MINC (b) dual-porosity (c) explicit discretization. Wu, Y.-S., & Pruess, K. (1988).

Due to the limited accuracy of the dual continuum approaches, different discrete fracture models (DFM) have been proposed for fractured reservoir simulation. This approach generally requires unstructured grid to conform to the fracture geometry, and grid refinement is usually needed near the fractures. The advantage for DFMs is that the influence of fractures can be directly incorporated in the model, without the need to assume any abstract property of the fracture network. The perpendicular bisector grid (PEBI) model is one common type of DFM. It was introduced to reservoir simulation by Heinemann, Z. E. et al. (1989) and has been a popular approach for fractured reservoir simulation studied by many researchers. The flux direction is ensured to be perpendicular to the grid boundary, therefore the accuracy can be maintained when using two-point flux approximation (TPFA). Sarda, S. et al. (2002) proposed a 2-D discretization scheme for fractured reservoirs. A similar approach was taken for matrix-fracture flux as in the dual-porosity model, and a pseudo-steady state flow assumption is needed for the derivation of the model. Karimi-Fard, M. et al. (2004) proposed a discrete fracture model with unstructured gridding to explicitly represent the fractures, and employed two-point flux approximation to account for the

mass transfer between grid blocks. Sandve, T. H. et al. (2012) extended the method from two-point flux approximation to multiple point approximation and obtained improved accuracy. However, it can be computationally challenging to generate the unstructured grids that conform to the fracture geometry, and Mustapha, H. (2014) has shown that the quality of the mesh is often not good with a large number of tiny grid blocks.

Another explicit model named embedded discrete fracture model (EDFM), which was originally proposed by Lee, S. H. et al. (2000) and Li, L. et al. (2008), recently got more attention due to its high computational efficiency and flexibility. This approach does not require the model grid to conform to fracture geometry. Instead, fractures can just be embedded within a matrix grid block. Therefore, traditional grids can still be used, while the fractures are naturally discretized by the confining matrix grid blocks. By assuming a linearly distributed pressure around the fractures, the pressure drop between the matrix grid and the fracture grid can be estimated. This approach provided a subgrid resolution that lifted the necessity to refine the grids near the fractures. Moinfar, A. et al. (2013) implemented the EDFM model for 3D cases. Jiang, J. et al. (2016) combined traditional MINC and EDFM to simulate reservoirs with fractures at different scales. In their work, the MINC subdivision is not related to the fractures geometry. Ding, D. Y. et al. (2018) recently proposed a model combining the MINC approach with the concept of EDFM. In their model, MINC subdivision is performed with fractures at the center, and the matrix is discretized using a proximity function from the fractures. Yang, D. et al. (2018) added Matrix LGR to the original EDFM when fractures are intersecting for 2D cases. EDFM provides an efficient solution to simulation problems with a complex fracture network. However, there are also some limitations. Tene, M. et al. (2017) reported that when fractures are sealed and form flow barriers, a large error might occur for EDFM. In their work, they proposed a projection based EDFM model by adding

extra connections between fracture grid and neighbor matrix grid, and modified matrix connections that are separated by the fractures.

In this work, we developed the cEDFM reservoir model based on EDFM framework. However, the splitting of matrix grids allows for a more physical representation of the reservoir. The cEDFM approach obtained a much-improved accuracy compared to EDFM for flux across the direction of fractures, which is a common case for inter-well flow.

2.2 Fractured Reservoir History Matching

Hydraulic and natural fractures play a major role in controlling the fluid transportation, especially for low permeable formations such as shale. Therefore, it is essential to understand the distribution and properties of these fractures in order to accurately model the production dynamics. Production data provides invaluable information, based on which the quality of the reservoir model can be improved. However in many cases, due to the limitation of the model assumptions, the well data couldn't be utilized adequately to quantify the property of the fracture networks.

Various approaches have been proposed for automatic history matching and uncertainty quantification. The algorithms can generally be categorized into gradient-based and non-gradient-based methods. Gradient-based algorithms require the calculation or approximation of the gradient matrix. One of the common approaches is to use the adjoint method to calculate the gradient. Some of the early work include Wu, Z. et al. (1998) and Li, R. et al. (2001). Another approach is to use streamline simulation to obtain the sensitivity matrix analytically. Since access and modification to the simulator source code is needed with this type of approach, it's usually not realistic when using a commercial simulator.

For non-gradient-based methods, the ensemble approach is the most well-studied among all the different algorithms. Ensemble Kalman Filter (EnKF) is the most widely used ensemble-based technique in history matching, first proposed by Evensen, G. (2003). With this method, a set of realizations is sampled from the prior distribution of the parameter space, initially unconditioned to the observed data. Updates are then made sequentially to minimize the error between the observed and simulated data. EnKF requires to restart the simulation after each assimilation step, and both model parameters and state variables are updated during the assimilation step. Ensemble Smoother (ES) is a similar approach, but all observed data are assimilated in a single step, therefore it does not require constant restarting of the simulation. Chen, Y. et al. (2013) proposed an iterative ensemble smoother with ensemble randomized maximum likelihood (EnRML) algorithm and added the Levenberg-Marquart term to reduce the number of iterations required.

Another non-gradient-based algorithm to perform history matching and uncertainty quantification is with the Markov chain Monte Carlo (MCMC) algorithm. However, the acceptance rate of MCMC is usually too low to be practical for real applications in reservoir history matching, as discussed in the work of Oliver, D. S. et al. (1997). Therefore, different approaches were proposed to improve the acceptance rate and obtained promising results, such as in Bonet-Cunha, L. et al. (1998) and Ma, X. et al. (2008).

Several more unconventional approaches that are non-gradient-based have also been used in assisted history matching. Ouenes, A. et al. (1993) applied simulated annealing to a gas reservoir history matching problem. Schulze-Riegert, R. W. et al. (2002) implemented a workflow based on genetic algorithm for reservoir history matching, and took advantage of parallel computing that is

compatible with this approach. The benefit of such type of methods is that the solution would not be trapped in a local minimum. However, the application to more complex cases with a larger parameter space can be challenging for these algorithms. For a more complete review of the history matching algorithms, please refer to Oliver, D. S., & Chen, Y. (2010).

Most of the existing works are on history matching techniques in general, however, a few works focus on the application to fractured reservoirs. Gang, T. et al. (2006) proposed an upscaling scheme of fracture properties and generated dual-porosity models for history matching. Nejadi, S. et al. (2014) used a similar workflow to upscale discrete fracture network (DFN) models and used EnKF for history matching. However, Ahmed Elfeel, M. et al. (2013) compared different upscaling schemes, and their results indicate that different upscaling models may lead to very different results, underlining the importance to quantify the upscaling errors and the influence on the results of history matching. Ping, J. et al. (2013) proposed a parameterization method for fractured reservoir history matching with EnKF by using a vector representation. A level-set function, angle, and length of fractures are assigned to the candidate node set, describing the distribution of the fractures. Lu, L. et al. (2015) applied a technique in image compression named Hough transformation, and convert the Non-Gaussian parameters of fractured reservoirs to a Gaussian field in the new domain. Most of the work mentioned above are evaluated with conventional reservoir models through upscaling. That is partially due to the cost of generating explicit fracture models as well as the cost of simulation with them. For fractured reservoirs, especially when using explicit fracture models, the non-linearity is even more significant, therefore challenging the applicability of the existing history matching methods. Ping, J. (2017) recently used an explicit model to perform history matching. A polyhedral mesh with a mimetic finite difference (MFD) is used with EnKF in their workflow.

In this work, we investigated a couple of different history matching algorithms for fractured reservoir history matching. First, we combined two-stage MCMC with a proxy model and cEDFM for history matching, and optimized naturally fractured reservoir production. For more complex cases with larger parameter space, we incorporated cEDFM into the EnKF workflow for history matching. A level-set function is defined to help parameterize the model and represent the uncertainty.

CHAPTER III

GENERAL UNSTRUCTURED RESERVOIR UTILITY (GURU)

3.1 Overview

The complex geology in fractured reservoirs requires a more flexible modeling approach than the conventional cube grids. Therefore, a control volume finite difference (CVFD) formulation is more appropriate in our case than the finite difference approach. This is because with CVFD, the connectivity between cells can be freely defined, without any constraint that certain pattern needs to be followed. In this work, the fractured reservoir modeling code is developed for the in-house reservoir simulator named General Unstructured Reservoir Utility (GURU) developed at Texas A&M University. GURU is a CVFD-based full compositional reservoir simulator, with multiple flow mechanisms incorporated for the modeling of conventional and unconventional reservoirs. Some of the features include:

1) Fully implicit time discretization;
2) Control-volume finite difference (CVFD) space discretization;
3) Two-point flux approximation (TPFA);
4) Consider multi-component adsorption;
5) Flux term consists of Darcy flow and Knudsen diffusion / gas slippage (if defined);
6) Compositional space preconditioning for vapor-liquid equilibrium (VLE) speedup;

Some of the assumptions include:

1) Water remains a separate phase;
2) The solution of other components in water is negligible;
3) VLE is performed for all components (except water) for oil / gas phase properties calculation.

The CVFD approach allows for a more flexible way to model the reservoirs. Different grid blocks can have flux between them as long as corresponding transmissibility term is defined. Note that even though our fracture modeling code is developed for GURU, it can be used for any reservoir simulator that accepts connection list and grid list as inputs.

3.2 Governing Equations

For a compositional model, the mass balance equation for any component in the oil / gas phase can be written as:

$$r_i = \frac{\partial \phi \left(s_o \tilde{\rho}_o x_i + s_g \tilde{\rho}_g y_i\right)}{\partial t} + \frac{\partial (1-\phi) m_i}{\partial t} - \nabla\left(\lambda_o \tilde{\rho}_o x_i \nabla\Phi_o + \lambda_g \tilde{\rho}_g y_i \nabla\Phi_g\right) - \sum_W \left(\tilde{\rho}_o x_i q_o^W + \tilde{\rho}_g y_i q_g^W\right) = 0 \quad \text{.....(3.01)}$$

In which:

$$m_i = \rho_s \tilde{\rho}_g^{sc} \frac{V_{L,i} y_i \frac{P_g}{P_{L,i}}}{1 + \sum_{k=1}^{n_h} y_k \frac{P_g}{P_{L,k}}} \quad \text{.....(3.02)}$$

In Equation (3.01), the first term is the accumulation term, the second term is the adsorption term, the third term is the Darcy flux term, and the right-hand side is the source / sink term. The formulation for the multi-component adsorption is from the work by Cao, Y. et al. (2015). The above equation can be rewritten in the form of control volume finite difference (CVFD) as:

$$R_{i,j} = \frac{1}{\Delta t}\left(N_{i,j}^{n+1} - N_{i,j}^{n}\right) + \frac{1}{\Delta t}\left(M_{i,j}^{n+1} - M_{i,j}^{n}\right) - \sum_c T_{j-c}\left(\lambda_{ro} \tilde{\rho}_o x_i \Delta\Phi_{o,j-c} + \lambda_{rg} \tilde{\rho}_g y_i \Delta\Phi_{g,j-c}\right) - \sum_W \left(\tilde{\rho}_o x_i Q_o^W + \tilde{\rho}_g y_i Q_g^W\right)_j = 0 \quad \text{.....(3.03)}$$

In which:

$$N_{i,j} = V_j \left[\phi\left(s_o \tilde{\rho}_o x_i + s_g \tilde{\rho}_g y_i\right)\right]_j \quad \text{.....(3.04)}$$

$$M_{i,j} = V_j \left[(1-\phi) m_i\right]_j \quad \text{.....(3.05)}$$

$$[Q_{o/g}^{W}]_j = V_j[q_{o/g}^{W}]_j \quad (3.06)$$

For the water phase, the formulation is similar and can be simplified to:

$$r_w = \frac{\partial(\phi s_w \tilde{\rho}_w)}{\partial t} - \nabla(\lambda_w \tilde{\rho}_w \nabla\Phi_w) - \sum_W(\tilde{\rho}_w q_w^W) = 0 \quad (3.07)$$

And the CVFD format can be rewritten as:

$$R_{w,j} = \frac{1}{\Delta t}\left(N_{w,j}^{n+1} - N_{w,j}^{n}\right) - \sum_c T_{j-c}\lambda_{rw}\tilde{\rho}_w \Delta\Phi_{w,j-c} - \sum_W(\tilde{\rho}_w Q_w^W)_j = 0 \quad (3.08)$$

In which:

$$N_{w,j} = V_j[\phi s_w \tilde{\rho}_w]_j \quad (3.09)$$

$$[Q_w^W]_j = V_j[q_w^W]_j \quad (3.10)$$

The relative phase mobility is given by:

$$\lambda_{ro/rg/rw} = \frac{k_{ro/rg/rw}}{\mu_{o/g/w}} \quad (3.11)$$

In addition to the two residue functions for oil / gas phase and the water phase in Equation (3.03) and Equation (3.08), the primary equations also include the volume balance equation and the well residual equation. The volume balance equation is given by:

$$R_{vol,j} = PV_j - V_{o,j} - V_{g,j} - V_{w,j} = 0 \quad (3.12)$$

For the detail of the well equations and other auxiliary equations, please refer to Yan, B. (2017). The primary variables include $N_{i,j}$, $N_{w,j}$, oil phase pressure $P_{o,j}$, as well as well bottom-hole pressure P_{wf}. Therefore, the equation set $\vec{R}$ to be solved has the size of $(n_h + 2) \times nCells + nWells$ and can be written as:

$$\vec{R} = \begin{bmatrix} \vec{R}_{res} \\ \vec{R}_{well} \end{bmatrix} \quad (3.13)$$

$$\vec{R}_{res} = \begin{bmatrix} \vec{R}_{i,j} \\ R_{w,j} \\ R_{vol,j} \end{bmatrix}_{i=1,\cdots,n_h;\ j=1,\cdots,nCells} \quad \text{.....(3.14)}$$

$$\vec{R}_{well} = [R_W]^T_{W=1,\cdots,nWells} \quad \text{.....(3.15)}$$

The primary variables $\vec{X}$ has the same size as $\vec{R}$, comprising of the grid variables and well variables:

$$\vec{X} = \begin{bmatrix} \vec{X}_{res} \\ \vec{X}_{well} \end{bmatrix} \quad \text{.....(3.16)}$$

$$\vec{X}_{res} = \begin{bmatrix} \vec{N}_{i,j} \\ N_{w,j} \\ P_{o,j} \end{bmatrix}_{i=1,\cdots,n_h;j=1,\cdots,nCells} \quad \text{.....(3.17)}$$

$$\vec{X}_{well} = [P_{wf,W}]^T_{W=1,\cdots,nWells} \quad \text{.....(3.18)}$$

The linear function set can be finally written as:

$$J\vec{\delta} = \vec{R} \quad \text{.....(3.19)}$$

In which:

$$J = \begin{bmatrix} \frac{\partial \vec{R}_{res}}{\partial \vec{X}_{res}} & \frac{\partial \vec{R}_{res}}{\partial \vec{X}_{well}} \\ \frac{\partial \vec{R}_{well}}{\partial \vec{X}_{res}} & \frac{\partial \vec{R}_{well}}{\partial \vec{X}_{well}} \end{bmatrix} \quad \text{.....(3.20)}$$

$$\vec{\delta} = \begin{bmatrix} \overrightarrow{\Delta X}_{res} \\ \overrightarrow{\Delta X}_{well} \end{bmatrix} \quad \text{.....(3.21)}$$

3.3 Multiple-Porosity Model

Shale reservoirs have a much more complex lithology and pore structures compared to conventional resources. Studies such as Wang, F. P., & Reed, R. M. (2009), Sondergeld, C. H. et al. (2010), Ambrose, R. J. et al. (2010) have shown that different porosity types coexist in shale reservoirs and each demonstrates a very distinct property. In this work, we implemented the

multiple-porosity model similar as in Yan, B. et al. (2013) and Hinkley, R. et al. (2013). There can be three or more porosity types in total, and mass transfer can take place between any two different porosity types and within any individual porosity type. Here we are only giving a general formulation without assuming any structure of the micro model as in the two publication mentioned above. However, for any given micro model, the transfer function can be calculated accordingly between different porosity types.

For the shale matrix, three porosity types are defined in total, including organic matrix (kerogen), inorganic matrix, and micro fracture. All fractures smaller than the grid dimension are considered micro fractures, and the properties of the micro-fracture continuum are calculated through upscaling same as in Lee, S. H. et al. (2000) or Nejadi, S. et al. (2014) when data is available. While all fractures larger than the dimension of a grid can be modeled with cEDFM discussed in the next chapter.

The model for shale matrix is a multiple-porosity multiple-permeability model, in which the Darcy flux term for inter-porosity mass transfer can be expressed as:

$$q_{m-n,ij} = T_{m-n,j}[\lambda_{ro}\tilde{\rho}_o x_i(\Phi_{no} - \Phi_{mo}) + \lambda_{rg}\tilde{\rho}_g y_i(\Phi_{ng} - \Phi_{mg})]_j \quad (3.22)$$

$$T_{m-n,j} = \bar{k}_{mn}\sigma_{mn}\mathrm{V}_j \quad (3.23)$$

$$\bar{k}_{mn} = \frac{1}{3}\left(\frac{k_{mx}k_{nx}}{k_{mx}+k_{nx}} + \frac{k_{my}k_{ny}}{k_{my}+k_{ny}} + \frac{k_{mz}k_{nz}}{k_{mz}+k_{nz}}\right) \quad (3.24)$$

When k_n is much larger than k_m, the equation above can be simplified to:

$$\bar{k}_{mn} = \frac{1}{3}(k_{mx} + k_{my} + k_{mz}) \quad (3.25)$$

From the equations above, the inter-porosity flux per unit rock bulk volume can be expressed as:

$$\overline{q_{m-n,ij}} = \bar{k}_{mn}\sigma_{mn}[\lambda_{ro}\tilde{\rho}_o x_i(\Phi_{no} - \Phi_{mo}) + \lambda_{rg}\tilde{\rho}_g y_i(\Phi_{ng} - \Phi_{mg})]_j \quad \text{.....(3.26)}$$

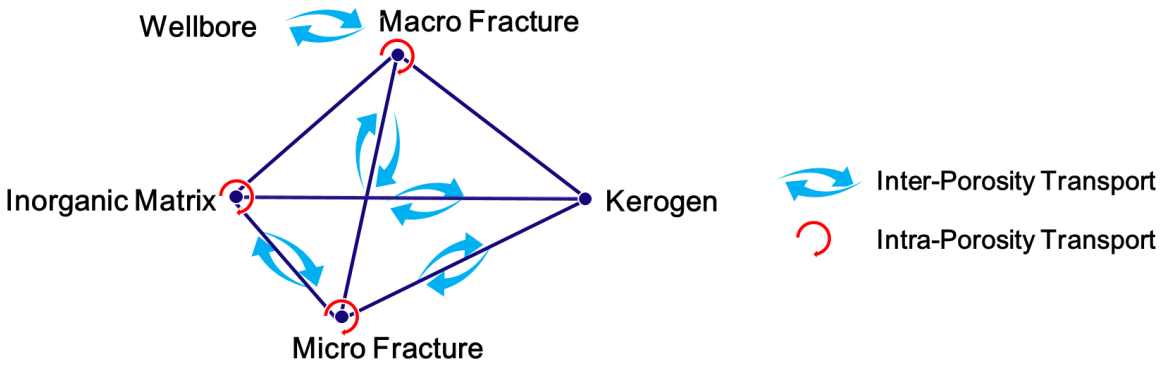

Figure 3.1—Mass transfer pyramid among different porosity types of shale reservoirs. Modified from Yan, B. et al. (2016).

It can be noticed that the value is independent of the size of the grid blocks. The flux between inorganic matrix, kerogen and micro fracture can be represented with the formulation above, while the flux between macro fractures and other porosity types are calculated explicitly, which we will discuss in detail in the next chapter. Therefore in shale reservoirs, flux can be expressed with the mass transfer pyramid as shown in **Figure 3.1**, adapted from Yan, B. et al. (2016).

3.4 Model Definition

Due to the flexibility of the CVFD approach, model definition in GURU is performed by a preprocessing module independent of the main calculation package. In addition to all the other conventional reservoir parameters, GURU reads in a cell list as well as a connection list to define the model. The data structures of the two classes are shown in **Figure 3.2**.

```
Class Cell
    Integer id;
    Integer rockType;
    Double poreVolume;
    ...
End
```

```
Class Connection
    Integer id;
    Integer cell_A;
    Integer cell_B;
    Double Transmissibility;
    ...
End
```

Figure 3.2—Cell and Connection class of GURU in pseudo code, from Yan, B. (2017).

The original preprocessing code only generates multiple-porosity model with orthogonal grid blocks described in Yan, B. et al. (2013). Here we first extended the capability of the package in the following aspects:

1) Different LGR may be defined for different porosity types;
2) Generalized formulation for multiple-porosity model;
3) Corner-point model generation (without fractures);
4) Model refining and upscaling.

CHAPTER IV [1]

COMPARTMENTAL EMBEDDED DISCRETE FRACTURE MODEL (cEDFM)

4.1 Overview

The concept of EDFM was first proposed by Lee, S. H. et al. (2000) and Li, L. et al. (2008). In their work, the matrix is first discretized without the need to consider the fractures. Fractures are then naturally discretized by the boundary of the matrix grid blocks. The transmissibility between fracture and the matrix is calculated in a manner similar to the well index. For the case of the well index, the relationship between well cell pressure and bottom-hole pressure can be derived based on the radial flow assumption. Similarly, by assuming a linearly distributed pressure near the fractures, an analytical expression of the transmissibility can be obtained between the fracture cell and the matrix cell. Therefore, no LGR is required near the fractures, which greatly reduced the computational cost of this approach.

Since the matrix grids do not need to conform to the geometry of the fractures, the approach can be easily used in any randomly generated fracture distribution. Compared to PEBI model, the expensive procedure such as the Delaunay triangulation can be avoided, and the obtained model is a lot smaller. Compared to dual-continuum models, this approach has a much-improved accuracy.

In original EDFM implementation, three types of non-neighbor connections (NNCs) are considered to connect the fracture grids with the rest of the reservoir, including the connections: 1) between fracture and the matrix grid it's intersecting; 2) between two intersecting fracture grids; 3) between two neighbor fracture grids from the same fracture. The formulations to calculate the

[1] Part of this chapter is reprinted with permission from "Chai, Z., Tang, H., He, Y., Killough, J., & Wang, Y. Uncertainty Quantification of the Fracture Network with a Novel Fractured Reservoir Forward Model." Copyright [2018] by Society of Petroleum Engineers.

transmissibility for each of the types are summarized in **Table 4.1**. Notice that not all parameters are applicable to each of the NNC types.

Table 4.1—EDFM formulation.

$NNC\ Type$	T_{NNC}	A_{NNC}	k_{NNC}	d_{NNC}	T_i	$\overline{d_{f_i l}}$
I	$\frac{A_{NNC}k_{NNC}}{d_{NNC}}$	$A_{fracture}$	$\frac{2}{{k_f}^{-1}+{k_m}^{-1}}$	$\frac{1}{V}\int_{\Omega_v} d_{vf}dv$	--	--
II	$\frac{1}{{T_1}^{-1}+{T_2}^{-1}}$	$l_{f_1f_2}\min(w_{f_1}, w_{f_2})$	--	--	$\frac{k_{f_i}A_{NNC}}{\overline{d_{f_i l}}}$	$\frac{1}{S}\int_{\Omega_S} d_{sl}ds$
III	$\frac{1}{{T_1}^{-1}+{T_2}^{-1}}$	$l_{f_1f_2}\min(w_{f_1}, w_{f_2})$	--	--	$\frac{k_{f_i}A_{NNC}}{d_{f_i l}}$	--

Note that: for $NNC-I$, A_{NNC} is calculated as the area of the fracture segment, d_{NNC} is the average distance to the fracture plane from the grid; for $NNC-II$ and $NNC-III$, T_{NNC} is calculated by two half-transmissibility terms, and an surface integration over the fracture segment is needed for $NNC-II$ to calculate the characteristic distance $\overline{d_{f_i l}}$.

4.2 Limitation of EDFM

Although there are many desirable properties for the EDFM approach, a few limitations do exist that hinder its broader application.

Few previous publications have validated the accuracy of EDFM in simulating highly conductive fractures, such as in Moinfar, A. et al. (2013), Jiang, J. et al. (2016), Chai, Z. et al. (2016). However, for low permeable fractures, large errors are observed for both single and multi-phase flow problem, mostly due to the inability of this method to constrain the flow within the matrix when flow barrier is present. Tene M. et al. (2017) proposed the projection-based EDFM (pEDFM) to modify matrix-matrix transmissibility. The method is easy to apply based on existing

EDFM framework, and the result indicates an improved accuracy. However, errors can be introduced to the pore volume at two sides of the fractures with the approach.

In addition, the current implementation is based on the assumption that the models have orthogonal grids. This assumption greatly simplifies the calculation of intersection points between fracture and matrix, as well as between different fractures. However, in order to apply this model to real field cases, in which models are usually built using corner-point grids, we have to remove the assumption and develop a model that is more general. In theory, EDFM can work with not only orthogonal and corner-point grids, but also any type of unstructured grids, as long as the necessary model parameters can be calculated.

Furthermore, since a consistent mesh needs to be used throughout the reservoir for the original EDFM implementation, the number of grids can be unnecessarily large, especially for cases with only sparse fractures. In the following sections, we will discuss the improvement made for the new model that lift these limitations mentioned above.

4.3 Compartmental EDFM

4.3.1 Model Schematics

Figure 4.1 illustrates the difference between EDFM and cEDFM. For a simple case of a single matrix grid intersected by a fracture, two grids are defined for the EDFM approach: one matrix grid and one fracture grid. It can be noticed that since there are only two grids, the flux is either from the matrix grid to the fracture grid, or the other way around. For cases such as fractured well production (or injection), the fracture network overall has a lower (or higher) pressure than the matrix, and the representation works fine.

However, for cases with flux across the fractures, which can be common for inter-well flux, the EDFM representation is no longer physical. Therefore, with the cEDFM approach, instead of

having a fracture grid embedded within a matrix grid block, the fracture grid would split the matrix grid that it's intersecting, and multiple matrix sub-grids would be generated. By performing matrix splitting, all fracture grids are at the boundary of matrix grid blocks. The model can be thought of as a variation of the discrete fracture model (DFM), except the fracture discretization approach and the transmissibility formulation between fracture grid and matrix grid are inherited from the original EDFM.

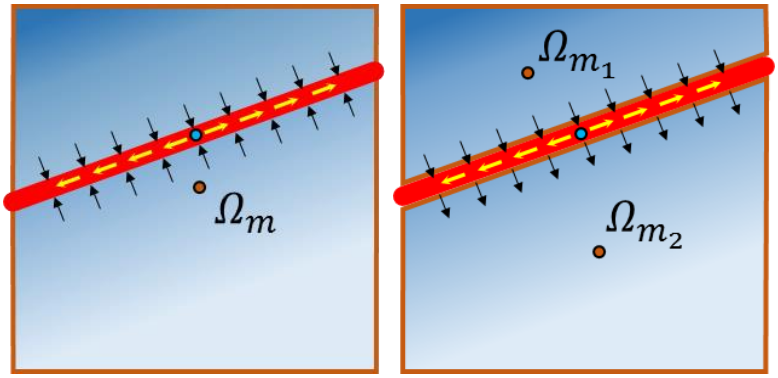

(a) EDFM (b) cEDFM

Figure 4.1—Schematic of the difference between EDFM and cEDFM for a simple case: single matrix cell intersected by a fracture. The fracture cell is denoted in red, and the background color corresponds to the pressure profile in the matrix.

As multiple fractures are defined, cases might occur where the contact area of the connection cannot be defined by any face of the sub-grids, such as between grid M_{12} and M_{21} as illustrated in **Figure 4.2 (a)**. It happens when two neighbor grids are split by two different fractures but not by both. This makes it especially complex to determine the connectivity among the sub-grids.

However, it can be noticed that this scenario only takes place near the tip of the fractures, therefore the problem can be solved by extending the fracture with "pseudo-fractures" one more grid beyond the original fracture tip, as shown in **Figure 4.2 (b)**. The matrix would be further split, which enables the contact area to be one of the surfaces of the new sub-grids. This also helps to

improve the orthogonality of the grid system, which is vital for two-point flux approximation to maintain its accuracy. Note that for pseudo-fractures, no additional fracture grid is generated, the sub-grids created have direct connections with each other, for example, between M_{23} and M_{24} in **Figure 4.2 (b)**.

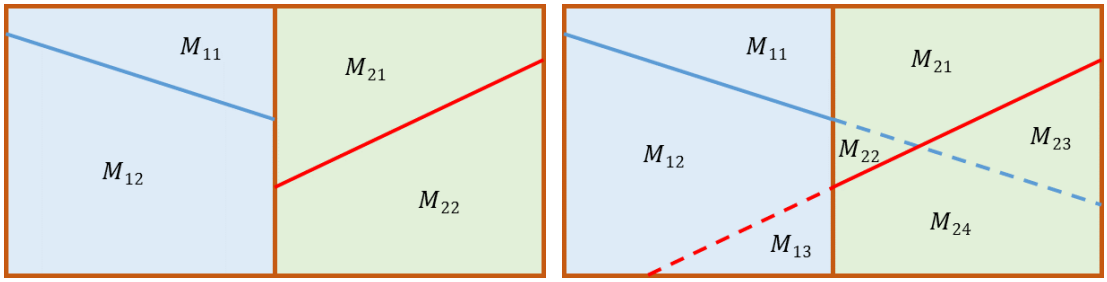

Figure 4.2—Pseudo-fracture extension at the fracture tips. (a) 1×2 grids intersected by 2 fractures. The contact area between M_{12} and M_{21} cannot be defined by any grid faces. (b) Pseudo-fracture added to further split matrix grids into conforming forms.

Figure 4.3 (a) demonstrated an example case with a 2×2 grid model intersected by 2 fractures. Note that one of the fractures only penetrates one of the matrix grid in the model. Pseudo-fracture is generated for this fracture, which extends it by one more grid block. Note that for ease of implementation and faster calculation, all fractures are automatically extended by pseudo-fractures one more grid block beyond its original bounds, without checking if conditions such as in **Figure 4.2** exists. Firstly, it would be tricky and time-consuming to perform the check; Meanwhile, by extending every single fracture, the problem can be automatically solved without adding much computational cost if any. In the example of **Figure 4.3**, the model is discretized into 3 fracture grids, 1 un-split matrix grid, as well as 8 sub-grids by splitting 3 matrix grids.

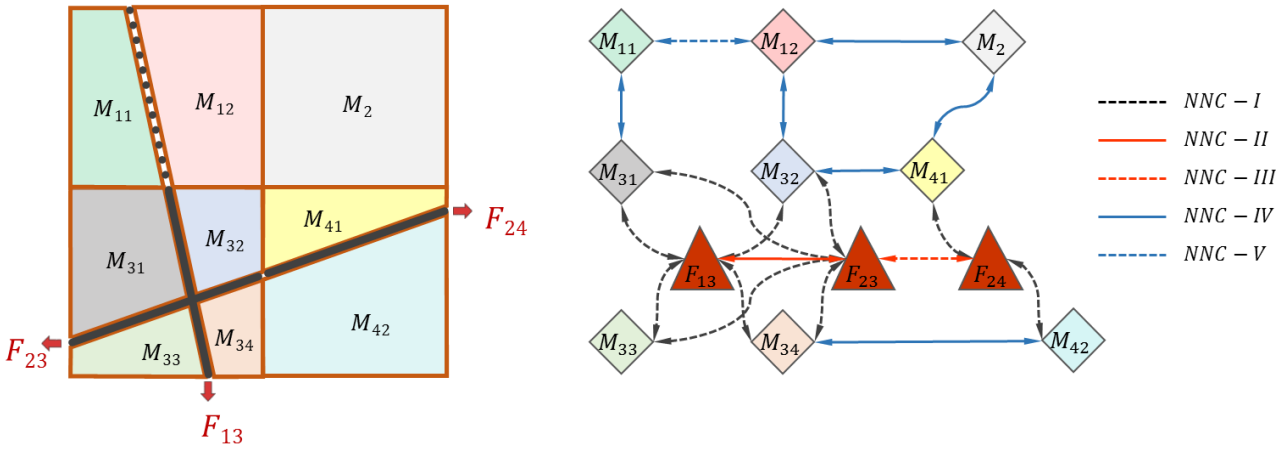

(a) Model discretization (b) Connection map

Figure 4.3—Illustration of the cEDFM scheme: (a): discretization of 2×2 grids intersected by 2 fractures; (b): connection map of the model, 5 types of non-neighbor connections (NNCs) defined. $NNC - I$: connection between matrix sub-grid and fracture grid; $NNC - II$: connection between two intersecting fracture grids; $NNC - III$: connection between two neighbor fracture grids of the same fracture; $NNC - IV$: connection between two sub-grids or one sub-grid and one un-split grid; $NNC - V$: connection between two matrix sub-grids separated by a pseudo-fracture.

4.3.2 None-neighbor Connections

For cEDFM, five types of non-neighbor connections (NNCs) needs to be defined, as shown in the connection map of **Figure 4.3 (b)**:

$NNC - I$: Connection between the matrix sub-grid and the fracture grid. As fracture grid f splits matrix grid m into multiple sub-grids, the $NNC - I$ needs to be modified as:

$$d_{NNC} = \frac{1}{V}\int_{\Omega_V} d_{vf} dv \ \left(\Omega_V = \Omega_{m_i}\right) \quad \text{.....(4.01)}$$

$$T_{NNC-I} = \frac{A_{NNC} k_{NNC}}{d_{NNC}} \quad \text{.....(4.02)}$$

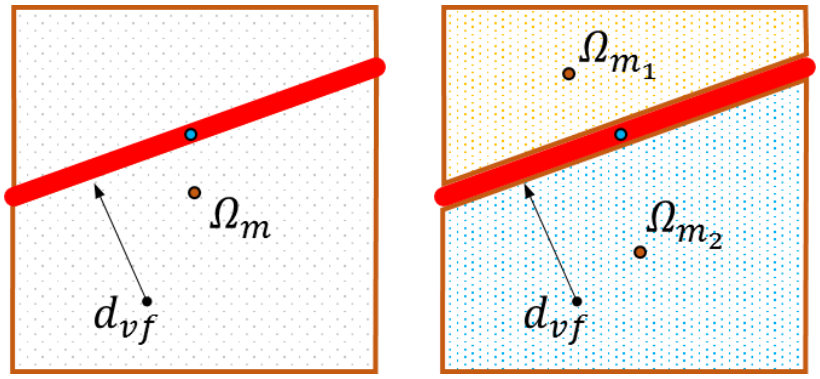

(a) Original T_{NNC-I} (b) Modified T_{NNC-I}

Figure 4.4—The computation of NNC Type-I is modified by only integrating over the sub-grids to calculate d_{NNC}.

This expression can be derived by assuming a linearly distributed pressure profile within the matrix near the fractures. The difference in pressure between the matrix grid and the fracture grid is therefore given by the pressure drop within the matrix. As shown in **Figure 4.4**, d_{NNC} is calculated with a volumetric average over the sub-grid instead of the whole grid as in EDFM, while k_{NNC} and A_{NNC} are the same as in **Table 4.1**.

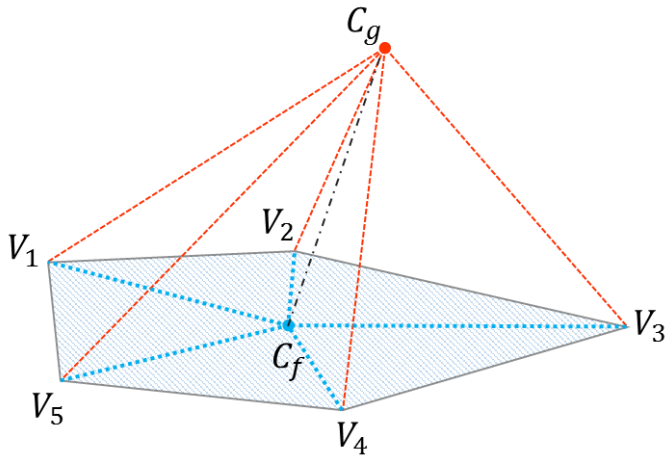

Figure 4.5—Tetrahedralization of a partial grid. The polygon at the bottom indicates one of the faces of the grid, with C_f denoting the centroid of the face. C_g denotes the centroid of the entire grid. 5 tetrahedrons are generated, with the four vertices being C_f, C_g, and two vertices of an edge.

Note that in Equation (4.01), the value of d_{NNC} is obtained by a volumetric integration. It would be both difficult and inefficient to integrate over an unstructured sub-grid in cEDFM. Therefore, an analytical solution is obtained instead by first performing tetrahedralization to the sub-grid, as shown in **Figure 4.5**. Since all fracture grids are at the boundary of the sub-grids, Equation (4.01) can be rewritten in a weighted volumetric average form as:

$$d_{NNC} = \frac{1}{V_{grid}} \sum_{i=1}^{nFaces} \sum_{j=1}^{nEdges} d_{c_{ijf}} V_{ij} \ \left(\Omega_{T_{ij}} \in \Omega_{m_i} \right) \quad \text{.....(4.03)}$$

where: T_{ij} is the tetrahedron corresponds to the j^{th}edge on the i^{th} surface, with a bulk volume of V_{ij}. $d_{c_{ijf}}$ is the distance of its centroid to the fracture plane, and V_{grid} is the bulk volume of the entire grid.

$NNC - II$: Connection between two intersected fracture grids. Here two intersected fracture grids do not split each other, therefore the original formulation in **Table 4.1** is still valid.

$$T_{NNC-II} = \frac{1}{{T_1}^{-1} + {T_2}^{-1}} \quad \text{.....(4.04)}$$

$$T_i = \frac{k_{f_i} A_{NNC}}{\overline{d_{f_i l}}} \quad \text{.....(4.05)}$$

$NNC - III$: Connection between two neighbor fracture grids that are from the same fracture. Similar as $NNC - II$, formulation is the same as in **Table 4.1**.

$$T_{NNC-III} = \frac{1}{{T_1}^{-1} + {T_2}^{-1}} \quad \text{.....(4.06)}$$

$$T_i = \frac{k_{f_i} A_{NNC}}{d_{f_i l}} \quad \text{.....(4.07)}$$

$NNC - IV$: Connection between two sub-grids or one sub-grid and one un-split matrix grid. This type of NNC is only between two grids that are from different parent grids. As illustrated in **Figure 4.6**, a binary identifier string is used to help identify the connections. The length of the string equals to the number of fractures intersecting any of the two grids, and each of the binary

identifiers corresponds to on which side of the fracture the sub-grid centroid is located at. Sub-grids with the same identifier string are then connected, otherwise sub-grids are separated by fractures and no direct connection exists between them.

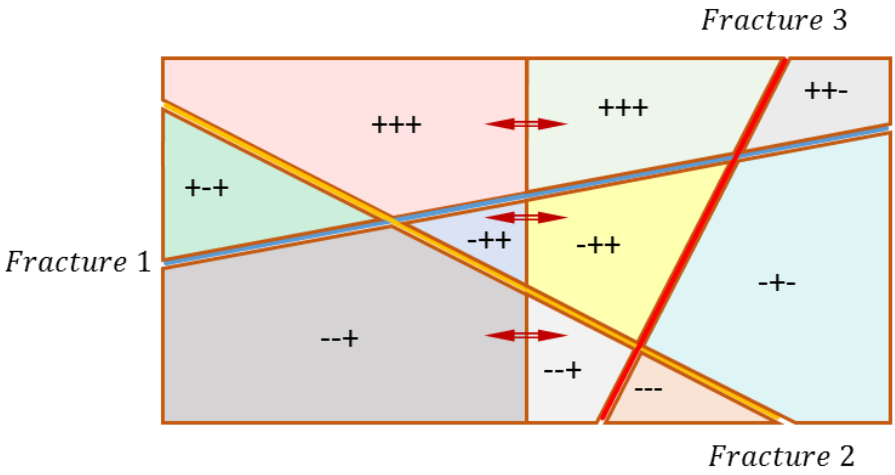

Figure 4.6—Scheme to establish $NNC-IV$ between neighboring sub-grids from different parent grid blocks. A binary identifier string is generated based on the spatial relationship of the sub-grid centroid and the fractures. Sub-grids with same identifier string are connected, as marked in double arrows.

$NNC-V$: Connection between two sub-grids that are separated by a pseudo-fracture. Sub-grids from the same parent grid do not have direct connections, unless they are separated by a pseudo-fracture. Therefore, only when one of the faces of the sub-grid is in contact with a pseudo-fracture, $NNC-V$ is defined. For both $NNC-IV$ and $NNC-V$, since the sub-grids are unstructured, a generalized formulation needs to be used to calculate the transmissibility, which will be discussed in the next section.

4.3.3 Generalized Transmissibility for Unstructured Sub-grids

To calculate the transmissibility between the sub-grids ($NNC-IV$ and $NNC-V$), we used the same inter-cell formulation as implemented in several commercial simulators, as shown below.

$$T = \frac{1}{{T_1}^{-1}+{T_2}^{-1}} \quad (4.08)$$

$$T_1 = \frac{A_x(x_C-x_1)+A_y(y_C-y_1)+A_z(z_C-z_1)}{(x_C-x_1)^2+(y_C-y_1)^2+(z_C-z_1)^2} \quad (4.09)$$

$$T_2 = \frac{A_x(x_C-x_2)+A_y(y_C-y_2)+A_z(z_C-z_2)}{(x_C-x_2)^2+(y_C-y_2)^2+(z_C-z_2)^2} \quad (4.10)$$

Here $A_{x/y/z}$ is the projected area of the shared face on x/y/z direction, (x_1, y_1, z_1) and (x_2, y_2, z_2) are the centroid of the two grid blocks, while (x_c, y_c, z_c) is the centroid of the shared face. Note that strictly speaking, multiple point flux approximation (MPFA) is needed if the grid system do not have perfect orthogonality, and the above equation is primarily for hexahedron grids that has a shape roughly resembles a cuboid. For simplicity, we used this formulation for the sub-grids as well which is unstructured and can have any geometry. However, measures have been taken to avoid grids that are too irregular by using pseudo-fractures, and the benchmarking results from the next chapter have shown that the formulation maintains a good accuracy compared to the reference cases. **Table 4.2** summarizes the formulation used to calculate the 5 types of NNCs in cEDFM.

Table 4.2—cEDFM formulation.

NNC	T_{nnc}	T_i	A_{nnc}	k_{nnc}	d_{nnc}	$\overline{d_{f_i l}}$
I	$\frac{A_{NNC}k_{NNC}}{d_{NNC}}$	--	$A_{fracture}$	$\frac{2}{{k_f}^{-1}+{k_m}^{-1}}$	$\frac{1}{V}\int_{\Omega_V} d_{vf}dv$	--
II		$\frac{k_{f_i}A_{NNC}}{\overline{d_{f_i l}}}$	$l_{f_1 f_2}\min(w_{f_1}, w_{f_2})$	--	--	$\frac{1}{S}\int_{\Omega_S} d_{sl}ds$
III	$\frac{1}{{T_1}^{-1}+{T_2}^{-1}}$	$\frac{k_{f_i}A_{NNC}}{d_{f_i l}}$	$l_{f_1 f_2}\min(w_{f_1}, w_{f_2})$	--	--	--
IV/V		$\frac{A_x(x_C-x_i)+A_y(y_C-y_i)+A_z(z_C-z_i)}{(x_C-x_i)^2+(y_C-y_i)^2+(z_C-z_i)^2}$	--	--	--	--

4.3.4 Grid Data Structure

For the EDFM approach, the discretized fracture grid can have either 3, 4, 5 or 6 edges, as shown in **Figure 4.7**. However, as matrix grids are split into multiple sub-grids in cEDFM, it is no longer feasible to enumerate all possible intersections, which can have any number of edges above 3. Therefore, a generalized data structure is needed to perform grid splitting automatically.

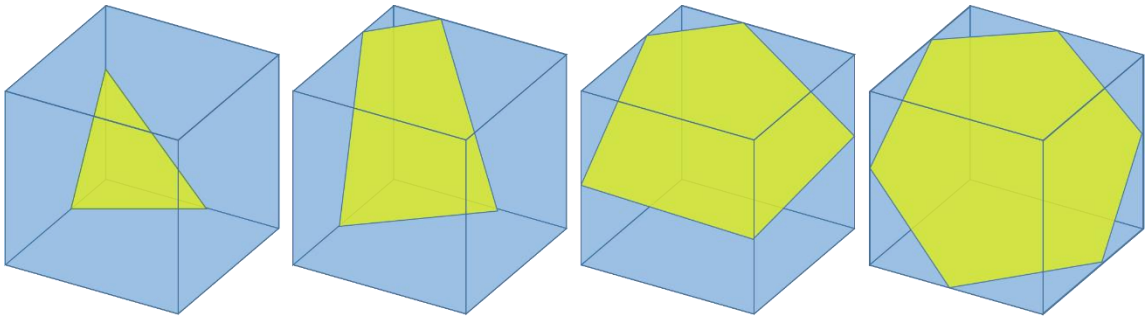

Figure 4.7—Possible intersections of a slant fracture plane and an orthogonal matrix grid. The fracture grid can be a triangle, quadrilateral, pentagon, or hexagon (Modified from Moinfar, A. et al., 2014).

The data structure as shown in **Figure 4.8** is defined for the Grid class. For each Grid object, it would have 3 properties (among others): a node set, an edge set, as well as a surface set. The node set keeps track of all the vertices of the grid, which is a $n \times 4$ matrix (n is the number of vertices). Each row represents a different vertex, including the unique ID of the node, as well as the x, y, z coordinates. The edge set specifies all edges of this grid, which is a $m \times 2$ matrix (m is the number of edges). Each row includes the two node IDs of this edge. Finally, the surface set keeps a record of all the surfaces of the grid, with each row representing a different surface. Since surfaces can have any number of nodes above 2, each row is defined as a list including an identifier as well as all vertices IDs of the surface. As a fracture intersects a grid, these properties would be updated accordingly. The initial Grid object before splitting is initialized with its 8 nodes, 12 edges and 6 surfaces.

```
Class Grid
    List<Array<Double>> node;
    List<Array<Integer>> edge;
    List<List<Integer>> surface;
    Array<Double> centroid;
    ...
End
```

Figure 4.8—Data structure of the Grid object in pseudo code.

Note that when there are multiple fractures intersecting within the same parent grid block, more than two sub-grids can be generated. Since a full 3D model is implemented for the cEDFM approach, tiny grid with small volume might be generated especially when the fracture network is complex. This would result in convergence issue and increase the computation time. Therefore, as shown in **Figure 4.9**, when calculating the intersection between a fracture and a matrix grid, close-by vertices around the intersection would be automatically detected. If the intersection is too close to an existing node within a certain tolerance, no new node would be generated. This prevents tiny grids from being created and ensures the numerical stability of the generated model.

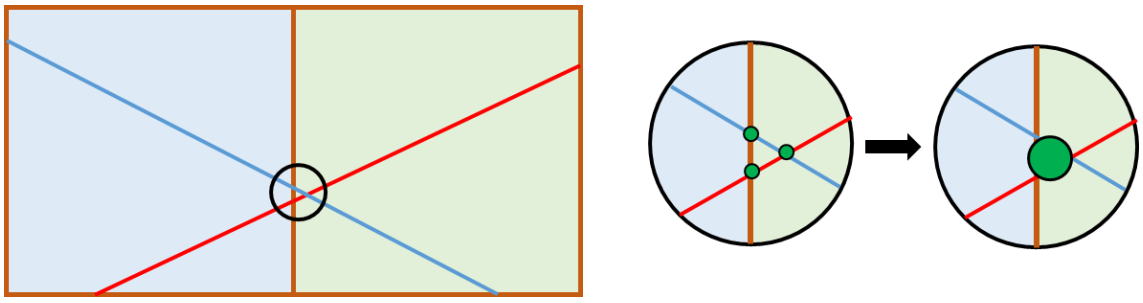

Figure 4.9—Eliminating small cells by merging close-by nodes.

4.4 Local Grid Coarsening

As discussed above, one advantage of the EDFM approach is that LGR is not necessary near the fractures. However, a consistent mesh needs to be used throughout the reservoir to

facilitate the generation of the model, which can be suboptimal in many cases. Ideally, a coarser mesh can be used in areas without any fractures to further reduce the number of cells. Therefore, in the implementation of cEDFM, a varied mesh is allowed, and an automatic local grid coarsening (LGC) algorithm is incorporated to detect areas with no fractures. The workflow is as follows:

1) A coarse mesh is first generated, based on the location of the fractures, the grids intersected by fractures are identified.
2) An indicator matrix with the same shape as the coarse grid is generated based on the result from the first step. For instance, the intersected grids have an indicator value of 1, their immediate neighbors not intersected by fractures can have a value of 2, the surrounding grids even further can have a value of 3, etc.
3) Larger indicator corresponds to a coarser mesh, with the mesh size a multiple of the next finer one.
4) Note that in order to generate a model with LGC, the code needs to be run twice. The first run solely generates the indicator map based on the coarse grid; the second run uses the indicator map as an input for matrix discretization, and generates the final model.

Without LGC, cEDFM would need more grids than EDFM due to matrix partitioning. However, with LGC, it can have a smaller grid number than EDFM. **Figure 4.10** shows a comparison case of cEDFM with and without automatic LGC. In the model is a horizontal well with 24 stages of hydraulic fractures, as well as 248 natural fractures scattered around the SRV, other model parameters are listed in **Table 4.3**. For this particular case, 22670 grids are needed without LGC, while only 15570 girds are needed with LGC for cEDFM, which is a reduction of 31.32%.

Table 4.3—Model parameters for LGC case comparison.

$Model$	$cEDFM\ (w/o\ LGC)$	$cEDFM\ (w/\ LGC)$
$Parent\ Grid\ Mesh$	$200\ ft$	$200/400/800\ ft$
$nCells$	22670	15570
$Reservoir\ dimension$	$12000\ ft \times 3200\ ft \times 32\ ft$	
ϕ	0.06	
k_{matrix}	$1.4 \times 10^{-3} md$	
$k_{fracture}$	$5 \times 10^{1} md$	
$w_{fracture}$	$0.05\ ft$	
$Reservoir\ fluid$	$black\ oil$	
$Wellbore\ radius$	$0.38\ ft$	
BHP	$4000\ psi$	
Pi	$8000\ psi$	
T	$180\ F^o$	

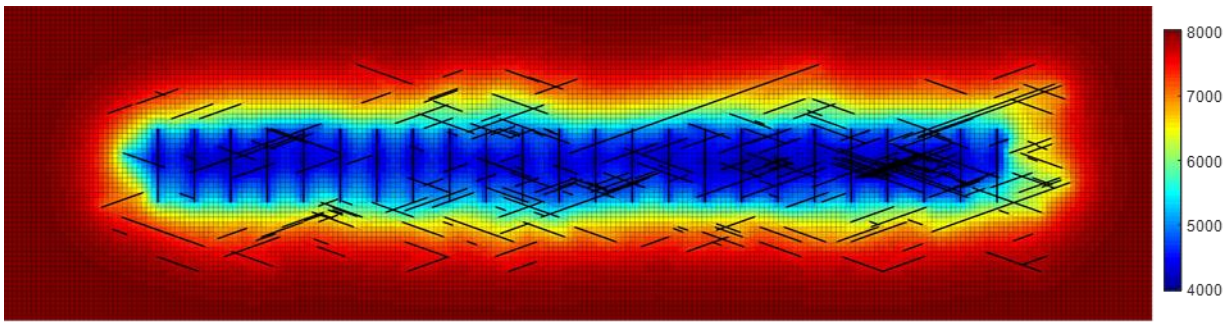

(a) w/o Local Grid Coarsening

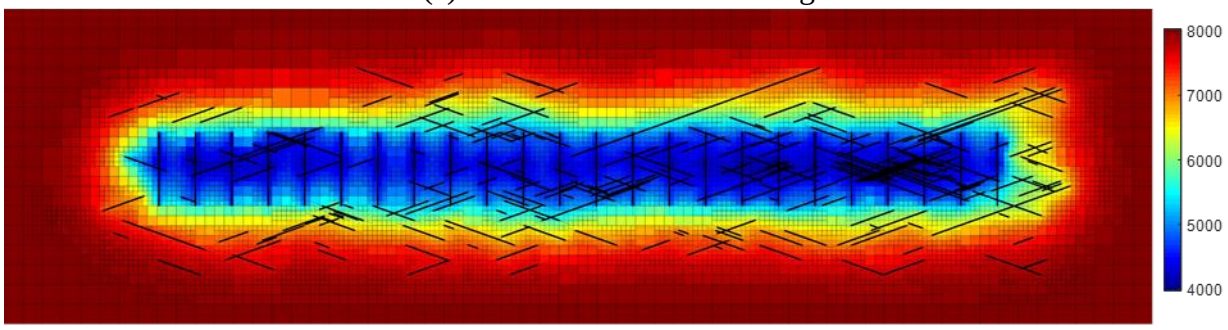

(b) w/ Local Grid Coarsening

Figure 4.10—Automatic local grid coarsening of cEDFM in unfractured areas.

Figure 4.11 shows the well production curve of the two models with and without LGC. The two models have a perfect match, hence no observable error is introduced by introducing LGC. Note that LGC is the most helpful when fractures are sparse and intersect only part of the reservoir. This case would also be used later for model benchmarking.

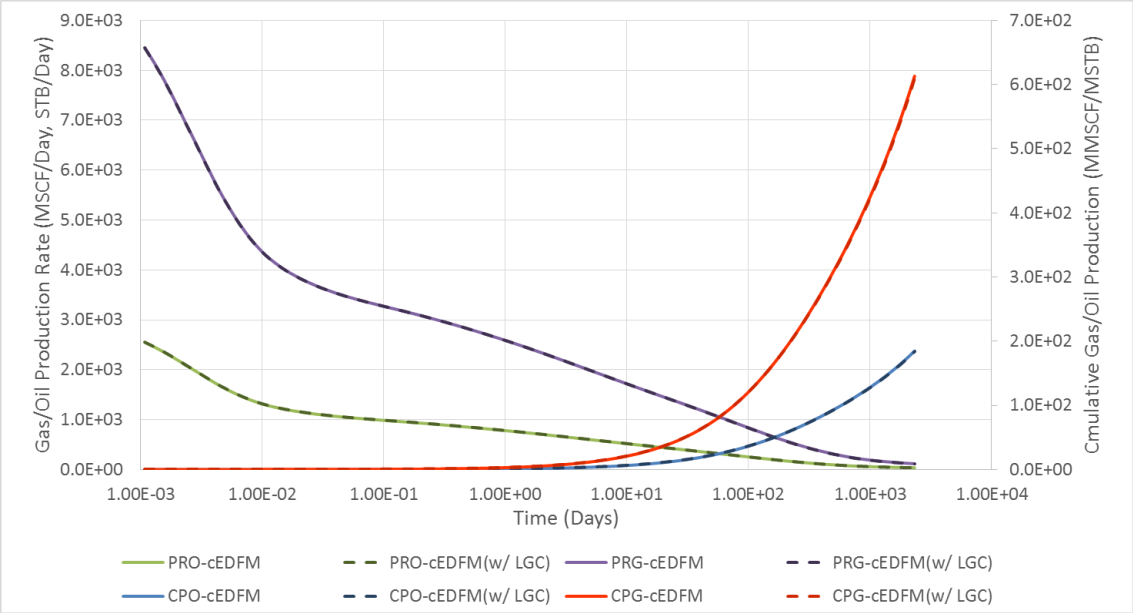

Figure 4.11—Well production curves of cEDFM with and without LGC.

4.5 Corner Point Extension

Another limitation of the original EDFM is that the application is restricted to orthogonal mesh. In order to improve the applicability of the model to real field cases, here we extended the implementation of cEDFM to be able to work with a full 3D corner-point grid system. When generalizing the implementation from orthogonal grids to corner-point grids, the assumptions that can be used to simplify the calculation of fracture-matrix and fracture-fracture intersections are no longer valid, therefore the whole program needs to be rewrite accordingly. With the generalized model, fractures can be easily incorporated into existing reservoir models, which makes cEDFM more practical for field applications.

Different approaches have been proposed to calculate the transmissibility between corner point grids. Here the same formulation as specified in Equation (4.07) – (4.09) is used. It is widely implemented in most commercial simulators, therefore has a good compatibility for case benchmarking.

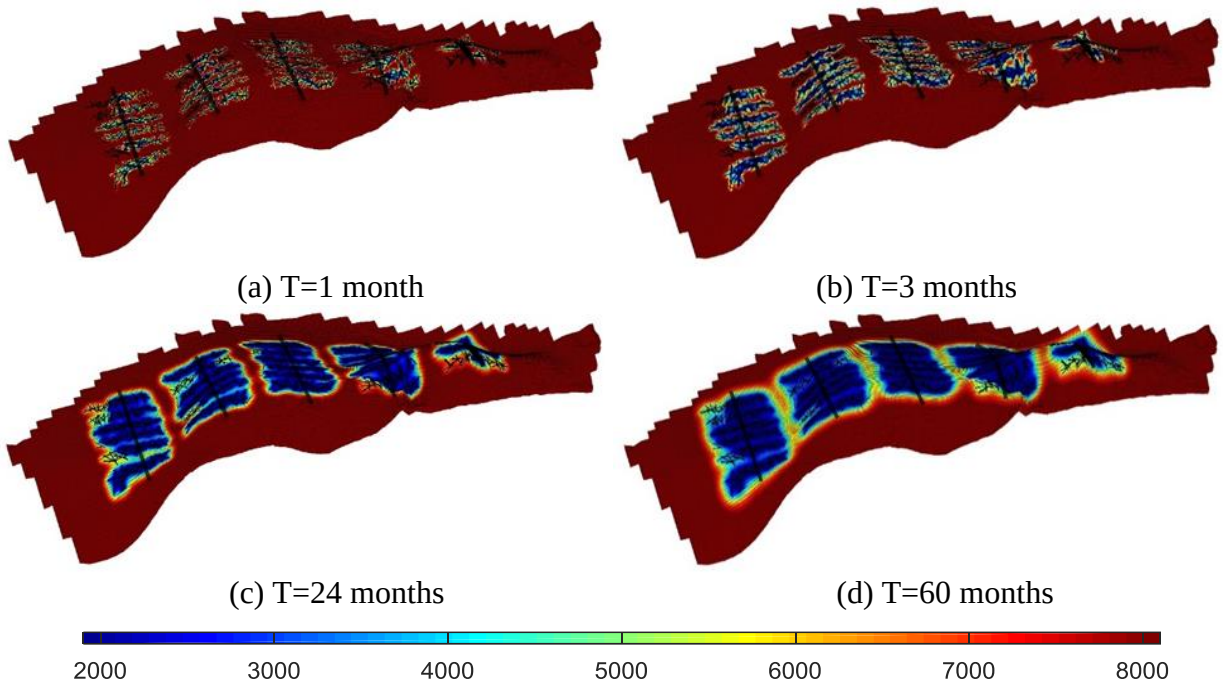

Figure 4.12—Pressure profile of the synthetic Brugge reservoir with 5 horizontal wells. 6 stages of hydraulic fractures for each well simulated with 1050 discrete fractures in total.

Figure 4.12 shows a synthetic case with 5 multi-stage hydraulic fractured horizontal wells completed in the Brugge reservoir. Each well has 6 stages of hydraulic fractures, with a total of 1050 discrete fractures in this model. Given the fracture locations and properties, the cEDFM approach can easily work with any existing reservoir models without the need to regenerate the mesh for the matrix.

CHAPTER V[2]

MODEL VERIFICATION OF cEDFM

5.1 Case Benchmarking for Single-Phase Flow Problem

In the first case, the cEDFM approach is compared to other models for a single-phase flow problem. CO_2 is injected from the left boundary of the square reservoir at a constant pressure of 12000 psi, and gas is produced from the right boundary at a constant pressure of 8000 psi.

Table 5.1—Model parameters for the single-phase flow problem.

$Mesh$	cEDFM	pEDFM	EDFM	Explicit
	11×11	11×11	11×11	251×251
$Model\ size$	$50\ ft\ \times 50\ ft$			
ϕ	0.10			
k_{matrix}	$1.0 \times 10^{-1} md$			
$k_{fracture}$	$1 \times 10^{3} md$			
$k_{barrier}$	$0\ md$			
$w_{fracture}$ / $w_{barrier}$	$0.05\ ft$			
$Reservoir\ composition$	$100\%\ methane$			
BHP_{inj}	12000 psi			
BHP_{prd}	8000 psi			
Pi	8000 psi			
T	$100\ F^{o}$			

[2] Part of this chapter is reprinted with permission from "Chai, Z., Tang, H., He, Y., Killough, J., & Wang, Y. Uncertainty Quantification of the Fracture Network with a Novel Fractured Reservoir Forward Model." Copyright [2018] by Society of Petroleum Engineers.

Two intersecting fractures are placed at the center of the model, and two scenarios are considered: 1) the fractures are highly permeable; 2) the fractures are non-permeable and form flow barriers. The results are compared to pEDFM, EDFM as well as the fine explicit model. The model parameters are as listed in **Table 5.1**. A couple of previous studies such as Tene, M. et al. (2017) used a relatively fine EDFM mesh for case comparison. However, models based on EDFM are rarely used with fine mesh in practice so as to take advantage of their efficiency. Here we used a much coarser mesh for cEDFM, pEDFM and EDFM compared to the fine explicit model.

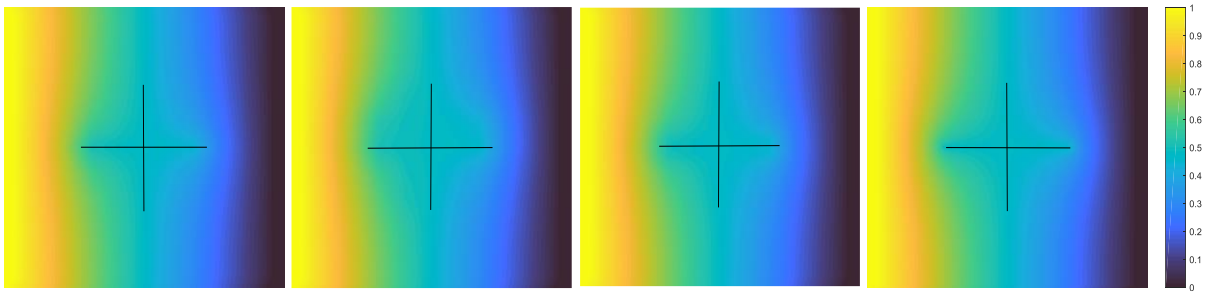

(a) EDFM (b) pEDFM (c) cEDFM (d) Fine Explicit Model

Figure 5.1—Case with highly conductive fractures: normalized pressure profile with CO_2 flooding, $PVI = 0.5$.

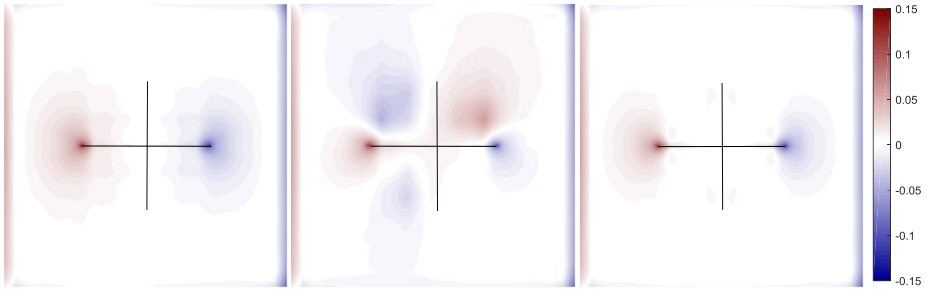

(a) EDFM (b) pEDFM (c) cEDFM

Figure 5.2—Case with highly conductive fractures: error map of normalized pressure with CO_2 flooding, $PVI = 0.5$.

For the case with highly conductive fractures, all three models can have a good match with the reference solution, as can be seen from **Figure 5.1** and **Figure 5.2**. cEDFM has the smallest error, but the results of the other two models are comparable. For the case when the fractures are non-permeable, EDFM yields an incorrect profile, as shown in **Figure 5.3**. pEDFM can improve

the result to some extent, but with a coarse mesh like used in this case, errors are still obvious in some of the regions. cEDFM is able to greatly reduce the error and reproduce the reference solution, as shown in **Figure 5.4**.

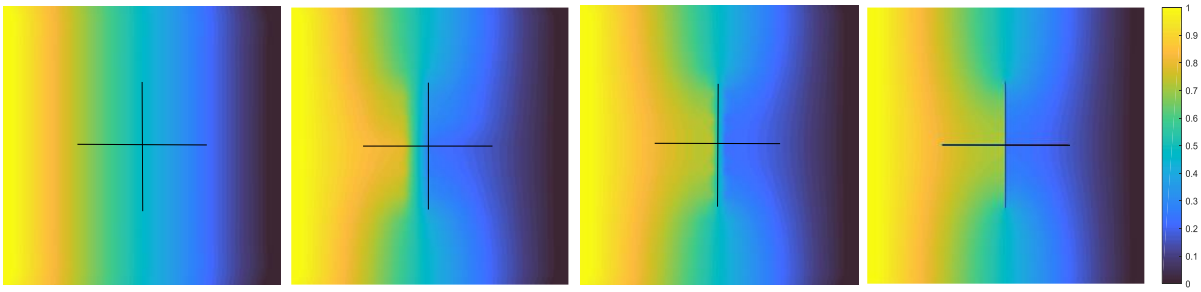

(a) EDFM (b) pEDFM (c) cEDFM (d) Fine Explicit Model

Figure 5.3—Case with flow barriers: normalized pressure profile with CO_2 flooding, $PVI = 0.5$.

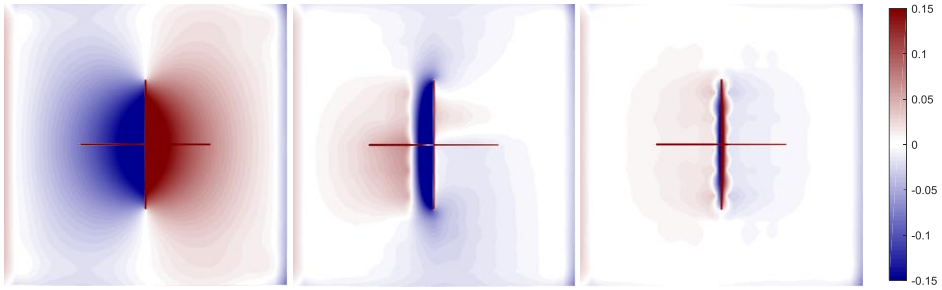

(a) EDFM (b) pEDFM (c) cEDFM

Figure 5.4—Case with flow barriers: error map of normalized pressure with CO_2 flooding, $PVI = 0.5$.

5.2 Case Benchmarking for Two-Phase Flow Problem

The model is then benchmarked for a two-phase flow problem. Both orthogonal fracture case and skewed fracture case are compared with the explicit model. **Figure 5.5** shows the map of the logarithmic permeability field ($log_{10}k$) of the benchmark models. Flow barriers exist as well as highly conductive fractures for both cases. The model parameters are listed in **Table 5.2**. Water is injected from the left boundary at a constant pressure of 12000 psi, and gas is produced from the right boundary at a constant pressure of 8000 psi, which is the same as the initial reservoir pressure.

Table 5.2—Model parameters for the two-phase flow problem.

$Mesh$	$cEDFM$ 100×100	$EDFM$ 100×100	$Explicit\ Model$ 1600×1600
$Grid\ Size$	2 ft	2 ft	0.125 ft
ϕ	0.1		
k_{matrix}	$5 \times 10^{-3} md$		
$k_{fracture}$	$1 \times 10^{3} md$		
$w_{fracture}$	$0.05\ ft$		
$k_{barrier}$	$1 \times 10^{-8} md$		
$w_{barrier}$	$0.05\ ft$		
$Reservoir\ composition$	$100\%\ methane$		
Pi	8000 psi		
T	$100\ F^{o}$		

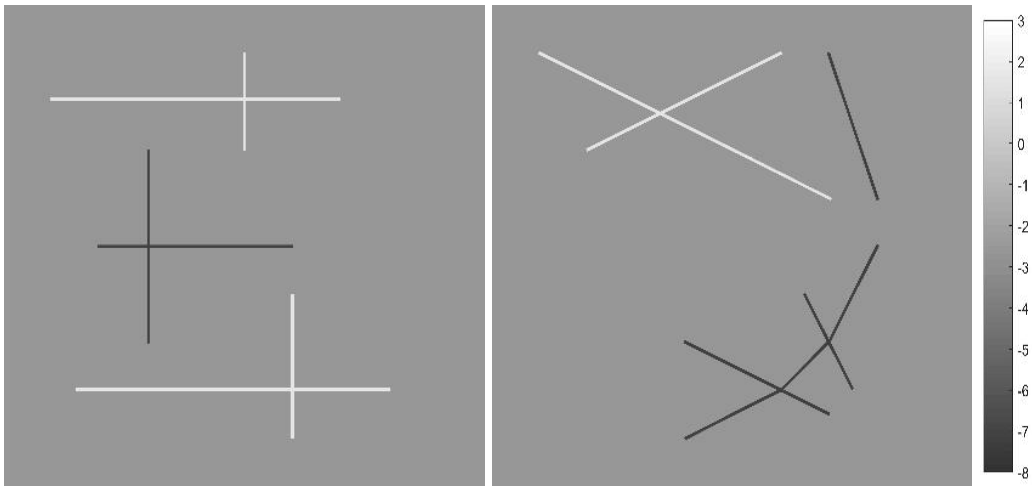

(a) Case I: Orthogonal Fractures (b) Case II: Skewed Fractures

Figure 5.5—Logarithmic permeability map of the benchmarking cases. Highly conductive fractures and low conductive flow barriers coexist in both cases.

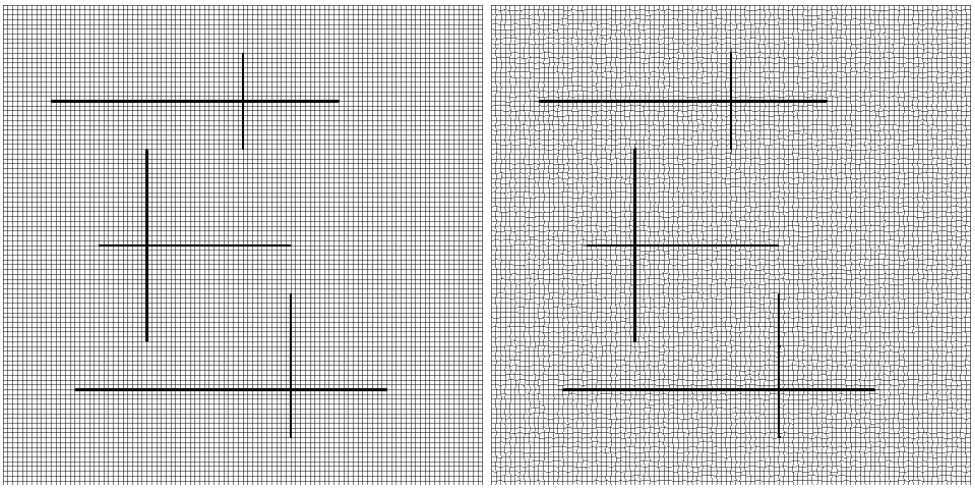

(a) Orthogonal Grids (b) Corner-Point Grids

Figure 5.6—Parent Grid of cEDFM for Case I. Locations of the fractures are marked in black.

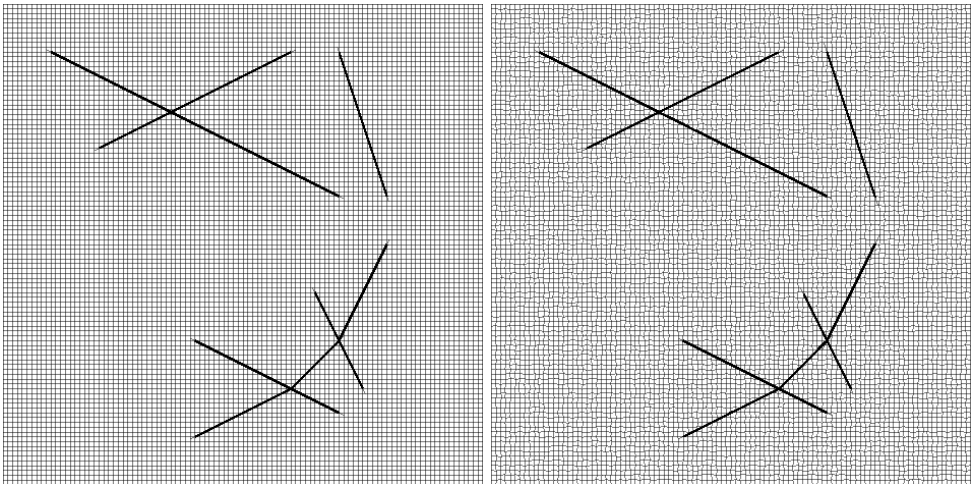

(a) Orthogonal Grids (b) Corner-Point Grids

Figure 5.7—Parent Grid of cEDFM for Case II. Locations of the fractures are marked in black.

Here we compared the results of cEDFM for both the orthogonal mesh as well as the corner-point mesh. The models are as shown in **Figure 5.6** and **Figure 5.7** for the two cases. The corner-point model has a rectangular outer boundary, therefore can still be compared with the same reference solution.

5.2.1 Case with Orthogonal Fractures

Below the pressure and water saturation profiles are compared against the fine reference solution ($PVI = 0.5$) for 3 models: EDFM, cEDFM and cEDFM (CPG), as shown in **Figure 5.8** and **Figure 5.9**. The corresponding errors are plotted in **Figure 5.10** and **Figure 5.11**. We can see for the EDFM case, a large discrepancy is observed in areas where flow barriers are present for both the pressure solution and the saturation solution. The pressure and water saturation front can freely pass the barriers. While the cEDFM solution gives an almost identical pressure solution as the reference case even when flow barriers are present. The saturation profile also has a much better match with the reference case, with a marginal error near the saturation front. For the cEDFM case with CPG mesh, the result is very comparable with the orthogonal grid case, with a slightly larger error as expected.

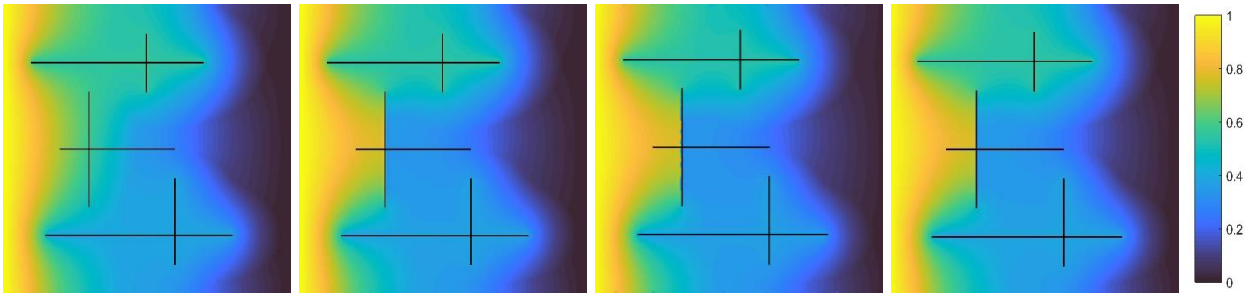

(a) EDFM (b) cEDFM (c) cEDFM(CPG) (d) Fine Explicit Model

Figure 5.8—Case comparison: normalized pressure profile of orthogonal fracture water flooding, $PVI = 0.5$.

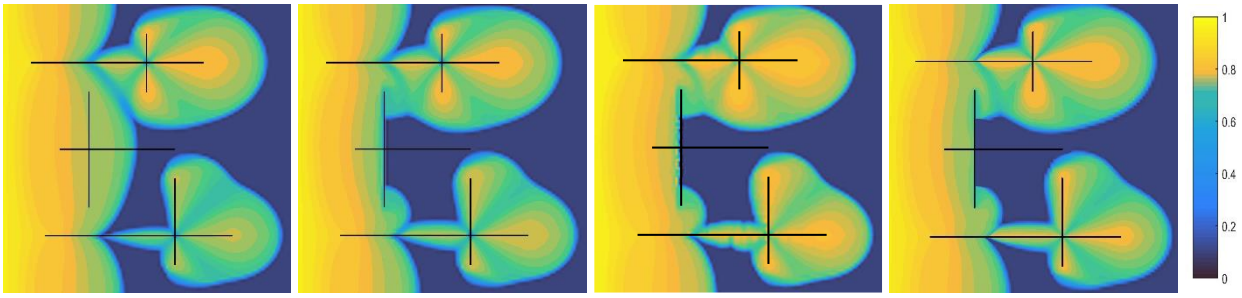

(a) EDFM (b) cEDFM (c) cEDFM(CPG) (d) Fine Explicit Model

Figure 5.9—Case comparison: water saturation profile of orthogonal fracture water flooding, $PVI = 0.5$.

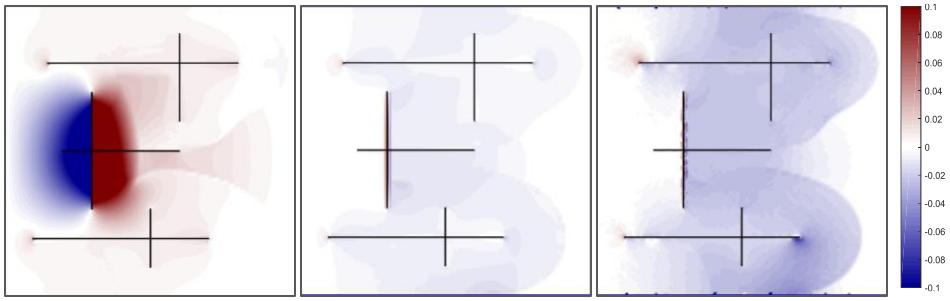

(a) EDFM (b) cEDFM (c) cEDFM (CPG)

Figure 5.10—Error map of normalized pressure, orthogonal fracture water flooding, $PVI = 0.5$.

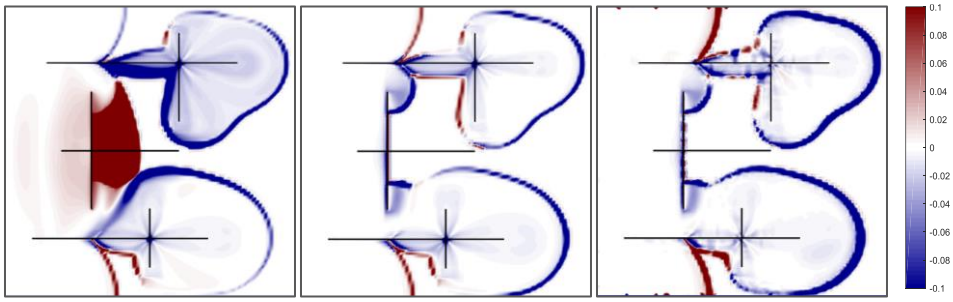

(a) EDFM (b) cEDFM (c) cEDFM (CPG)

Figure 5.11—Error map of water saturation, orthogonal fracture water flooding, $PVI = 0.5$.

5.2.2 Case with Skewed Fractures

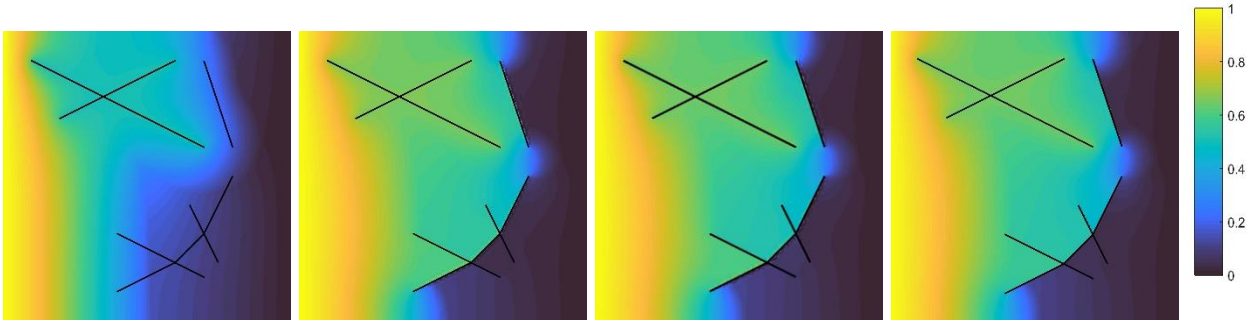

(a) EDFM (b) cEDFM (c) cEDFM(CPG) (d) Fine Explicit Model

Figure 5.12—Case comparison: normalized pressure profile of skewed fracture water flooding, $PVI = 0.4$.

For the case with skewed fractures, the pressure and water saturation profiles of the 3 models are again compared against the reference solution ($PVI = 0.4$), as shown in **Figure 5.12** and **Figure 5.13**. The errors are mapped as shown in **Figure 5.14** and **Figure 5.15**.

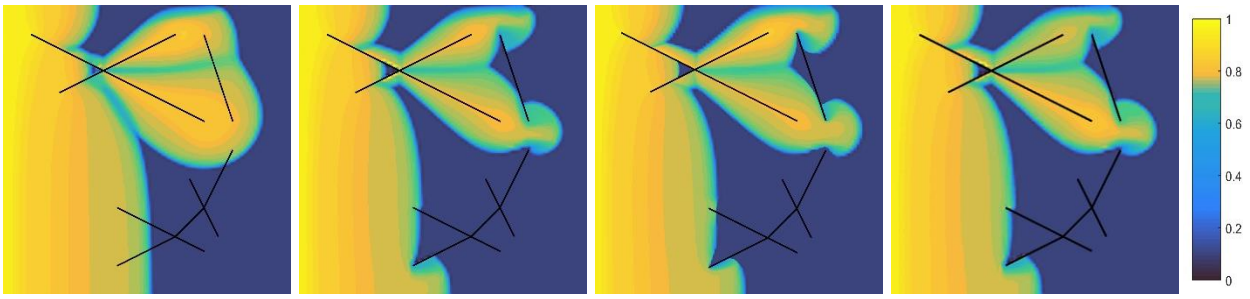

(a) EDFM (b) cEDFM (c) cEDFM(CPG) (d) Fine Explicit Model

Figure 5.13—Case comparison: water saturation profile of skewed fracture water flooding, $PVI = 0.4$.

It can be noticed that for the EDFM case, the added barriers do not change the pressure or the saturation profile at all. The simulation result would be exactly the same for the EDFM case if we only define the two highly conductive fractures at the top. This is due to the fact that in EDFM, the matrix is always continuous even when flow barriers are defined. While cEDFM is able to rectify the errors in these areas, and the errors are greatly reduced for both pressure and saturation solutions. Again, the cEDFM case with CPG mesh gives a comparable solution as with orthogonal grids, which validates the accuracy of the implementation.

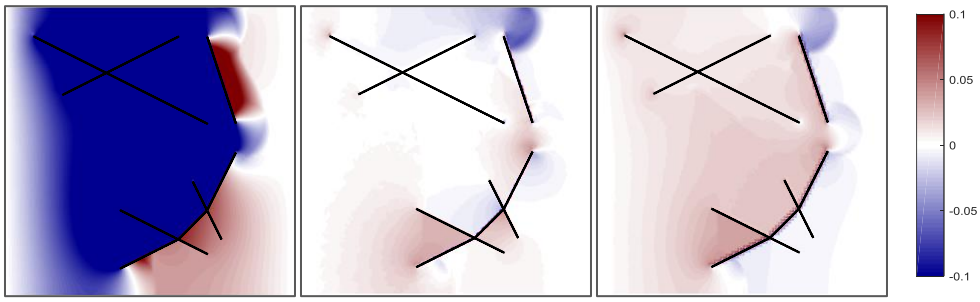

(a) EDFM (b) cEDFM (c) cEDFM (CPG)

Figure 5.14—Error map of normalized pressure, skewed fracture water flooding, $PVI = 0.4$.

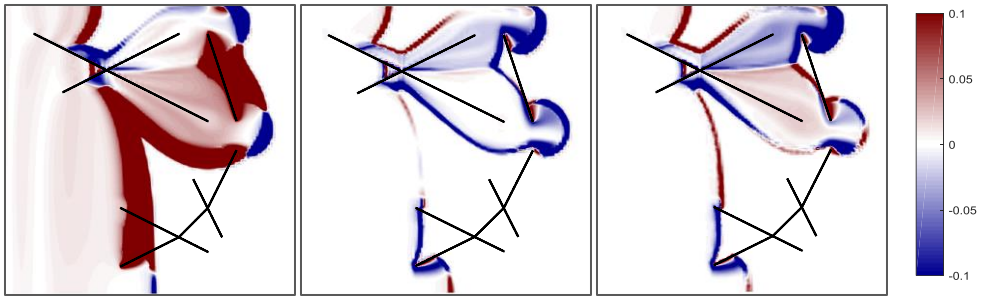

(a) EDFM (b) cEDFM (c) cEDFM (CPG)

Figure 5.15—Error map of water saturation, skewed fracture water flooding, $PVI = 0.4$.

5.3 Complex Horizontal Well Case Benchmarking with PEBI

Table 5.3—Model parameters for the complex fracture network problem.

Model	*PEBI*	*EDFM*	*cEDFM*
nCells	26393	17367	15570
Reservoir dimension	$12000\ ft \times 3200\ ft \times 32\ ft$		
ϕ	0.06		
k_{matrix}	$1.4 \times 10^{-3} md$		
$k_{fracture}$	$5 \times 10^{1} md$		
$w_{fracture}$	$0.05\ ft$		
Reservoir fluid	*black oil*		
Wellbore radius	$0.38\ ft$		
BHP	$4000\ psi$		
Pi	$8000\ psi$		
T	$180\ F^o$		

The cEDFM results are also compared against the PEBI model for more complex cases. Here a horizontal well with 24 stages of hydraulic fractures is producing at a constant bottom-hole pressure. There are 248 natural fractures randomly scattered near the SRV. The model parameters are listed in **Table 5.3**. The results of three models, PEBI, EDFM and cEDFM are compared. **Figure 5.16** shows the pressure profile after 5 years of production, and **Figure 5.17** shows the

production curve of the well for the 3 models. Note that the production curves are plotted on semi-log axes.

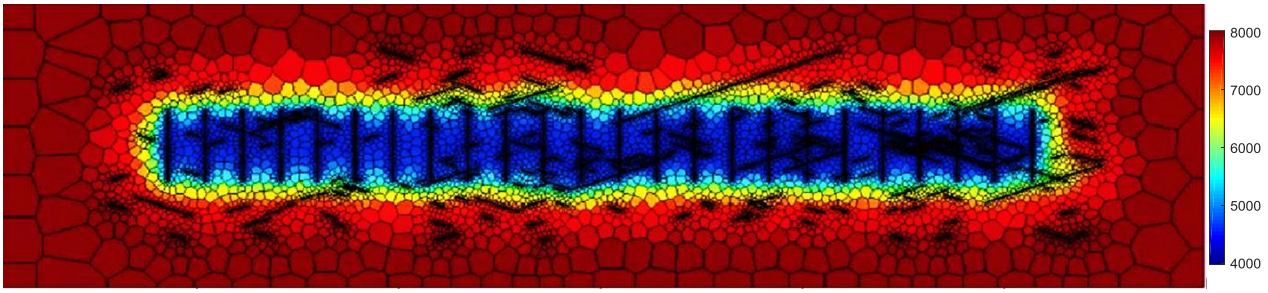

(a) PEBI

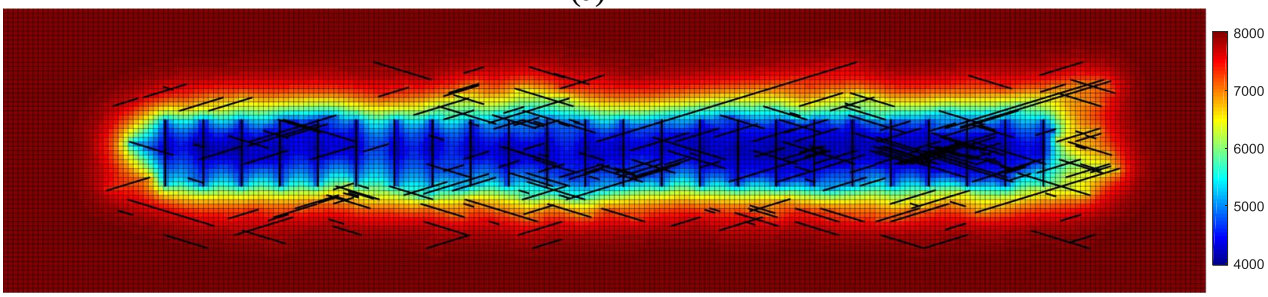

(b) EDFM

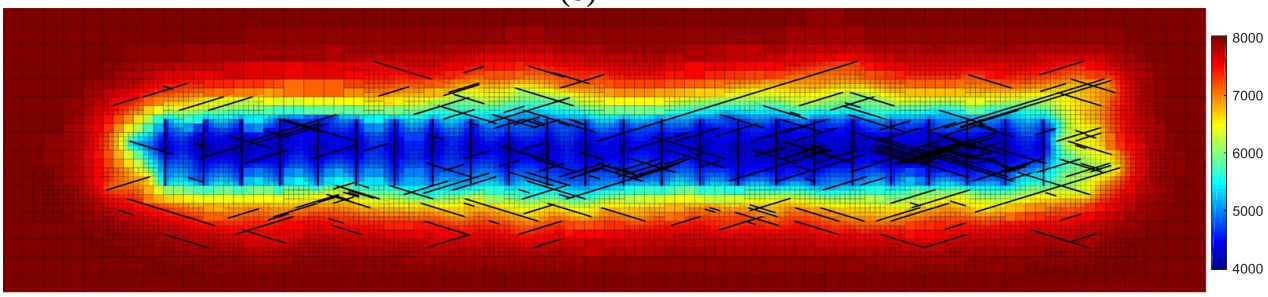

(c) cEDFM with LGC

Figure 5.16—Pressure Profile for a horizontal well case with 24 stages of hydraulic fractures and 248 natural fractures. Pressure profile after 5 years of production. PEBI model from Sun, J. et al. (2014).

We can see that both the pressure profile and the production reached a good match with the PEBI model. The discrepancy of the production curve is only at the very early stage within 1 day of production. Therefore, the model has a good accuracy for most applications. However, cautions need to be taken when a higher accuracy for the early transient stage is desired, such as in well-testing cases. LGR can be used under these circumstances to further improve the accuracy.

With the PEBI model as the reference solution, we can see cEDFM get a slightly better accuracy in the early stage compared to EDFM.

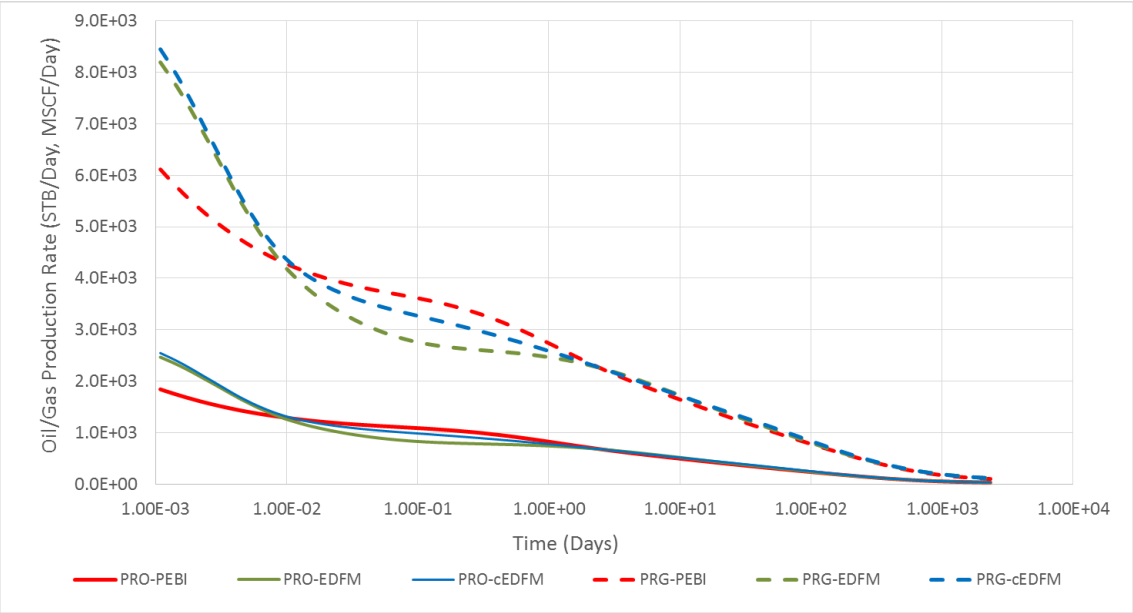

Figure 5.17—Well production rate of the 3 different models.

5.4 Sensitivity Analysis

Sensitivity analysis is also conducted for the cEDFM approach when using different mesh for the matrix. In the following demonstration case, CO_2 is injected into a gas reservoir from one corner and a producer located diagonally from the injector is producing at a constant bottom-hole pressure. Results from different mesh sizes are compared, as listed in **Table 5.4**. A total of 12 fractures are defined in the reservoir, and for all cases, the two wells are perforated within the matrix grids.

Figure 5.18 shows the C_1 concentration after 12 months of CO_2 flooding ($PVI \approx 0.2$). The coarse mesh could not capture the C_1 concentration profile for a relatively complex model like this, and a 6.20 % of relative error in cumulative C_1 production is observed. A much better result can

be obtained by using the medium mesh, with a 2.21 % of relative error in cumulative C_1 production. The three cases are also simulated without the fractures. The relative error in cumulative C_1 production is 3.53% for the coarse mesh, and 1.10% for the medium mesh. From the results, we can see that it is definitely more challenging to simulate a fractured reservoir. However, when the mesh is too coarse, the error persists even without any fracture as expected. A moderate refinement is usually adequate for the cEDFM approach without the need to perform additional LGR near the fractures.

Table 5.4—Model parameters for sensitivity analysis.

$Mesh$	$Coarse$ 10×10	$Medium$ 30×30	$Fine$ 90×90
$Grid\ Size$	50 ft	50/3 ft	50/9 ft
ϕ	0.12		
k_{matrix}	$1.5 \times 10^{-2} md$		
$k_{fracture}$	$5 \times 10^{3} md$		
$w_{fracture}$	$0.05\ ft$		
$Reservoir\ composition$	$100\%\ methane$		
BHP_{inj}	12000 psi		
BHP_{prd}	8000 psi		
Pi	8000 psi		
T	$100\ F^o$		
Relative Error	6.20 %	2.21 %	--
Relative Error (w/o fractures)	3.53 %	1.10 %	--

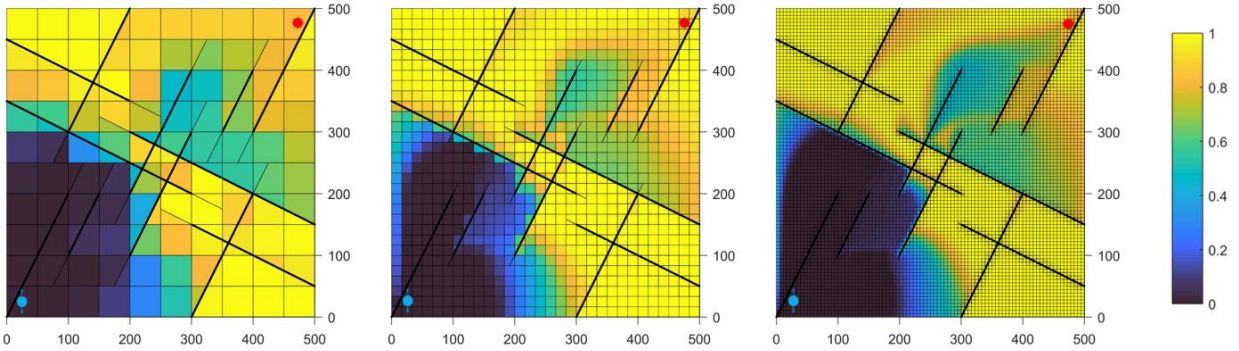

(a) 10 × 10 (b) 30 × 30 (c) 90 × 90

Figure 5.18—Sensitivity to parent matrix mesh: C_1 concentration after 12 months of CO_2 flooding.

CHAPTER VI

CASE STUDIES

6.1 Naturally Fractured Shale Reservoir

The first case demonstrates the simulation of a stimulated horizontal well with complex natural fracture network in a shale reservoir. A triple porosity model is defined to characterize the shale matrix, including organic matrix (kerogen), inorganic matrix, and micro fractures. The micro fracture porosity type only represents part of the natural fractures that are too small (below the mesh size of the matrix) to be represented explicitly. The large-scale natural fractures as well as the hydraulic fractures are modeled with cEDFM. In **Table 6.1** the model parameters are listed. It is a compositional model with an initial pressure of 8000 psi.

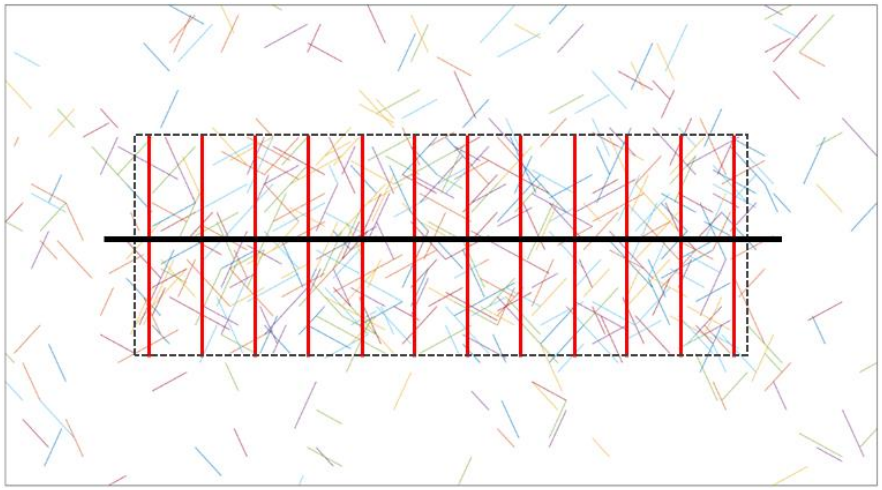

Figure 6.1—Large-scale natural fracture distribution. More active natural fractures within the SRV of the well.

Figure 6.1 shows the distribution of the natural fractures in the model. We are assuming a larger fracture density within the SRV, which is marked in the dashed box area. There are 512 macro fractures in this model: 500 large-scale natural fractures, and 12 hydraulic fractures.

The well produces at a constant BHP for 5 years. **Figure 6.2** to **Figure 6.4** shows the pressure profile of the 3 porosity types of matrix at different time steps. We can see a clear pressure difference between the different porosity types. Here a constant shape factor is used without any assumption of the micro model structure. It is obvious that the drainage area is limited by the part of the fracture network that is connected to the well, which highlights the importance of the fractures network in controlling the performance of the well.

Table 6.1—Model parameters for the multiple-porosity shale problem.

Porosity Type	*Kerogen*	*Inorganic Matrix*	*Micro Fracture*
Permeability	$2.5 \times 10^{-5} md$	$5.0 \times 10^{-5} md$	$7.5 \times 10^{-5} md$
Porosity	0.03	0.02	0.005
Reservoir dimension	$12000\ ft \times 3200\ ft \times 32\ ft$		
Matrix mesh	$101 \times 51 \times 1$		
$k_{hydraulic\ fracture}$	$5 \times 10^{3} md$		
$k_{natural\ fracture}$	$1 \times 10^{2} md$		
$w_{hydraulic\ fracture}$	$2 \times 10^{-2} ft$		
$w_{natural\ fracture}$	$5 \times 10^{-3} ft$		
$\phi_{fracture}$	0.35		
Reservoir fluid	8 *components*		
Wellbore radius	0.38 ft		
BHP	4000 psi		
Pi	8000 psi		
T	180 F^{o}		

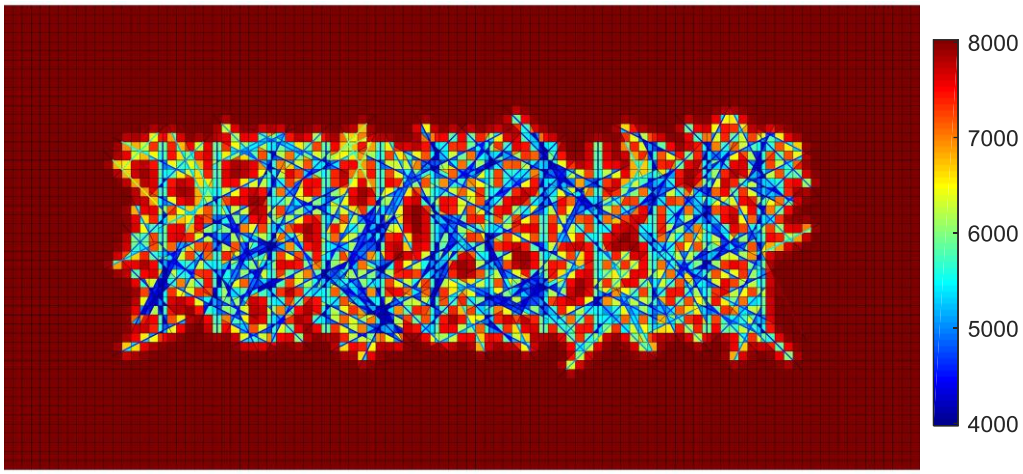

(a) t=1 months

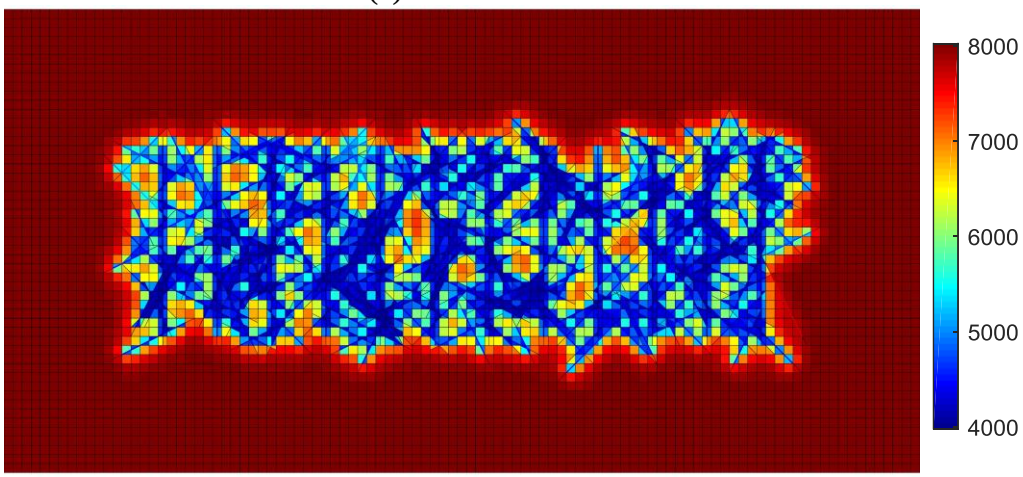

(b) t=12 month

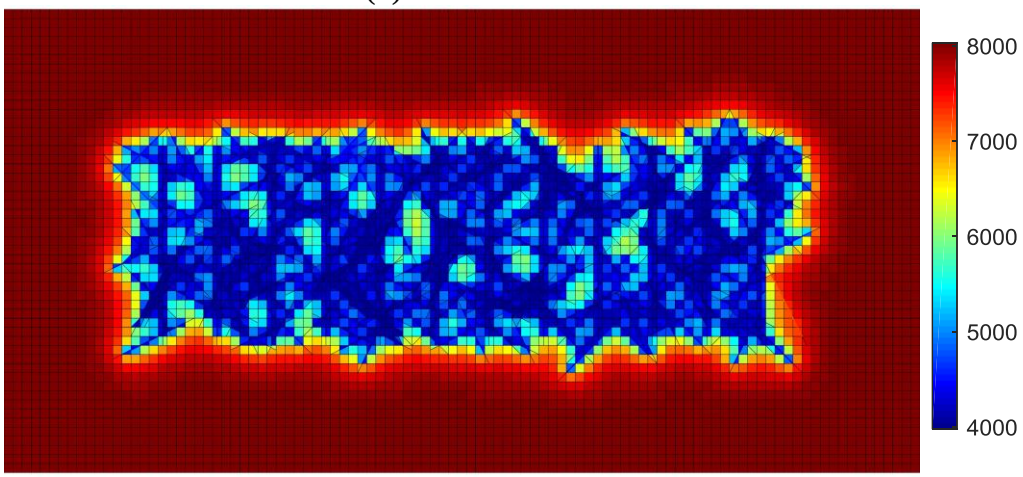

(c) t=60 months

Figure 6.2—Pressure profile of micro fractures for a hydraulic fractured horizontal well completed in shale formation.

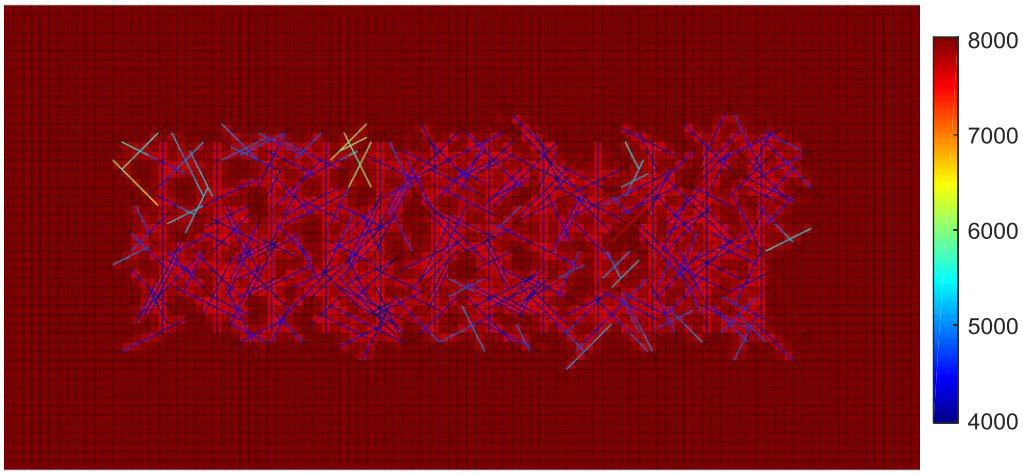

(a) t=1 months

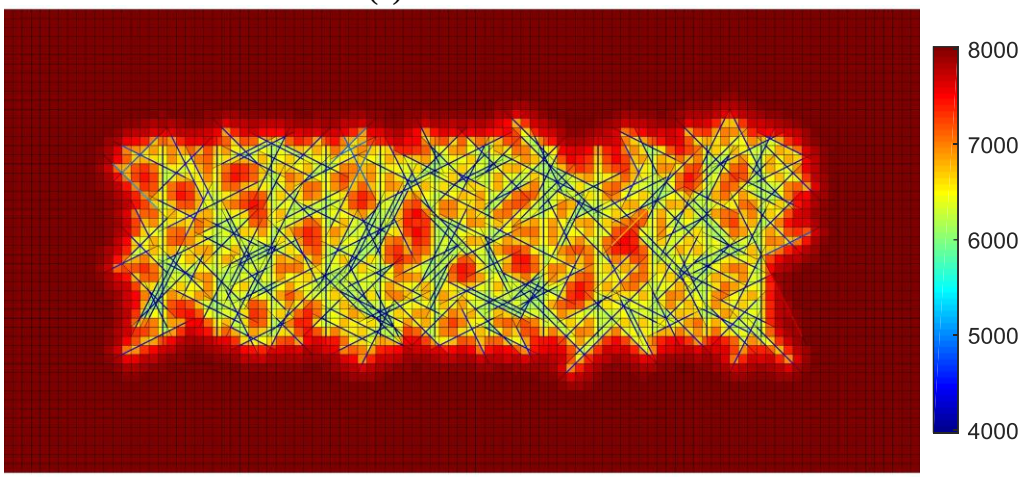

(b) t=12 month

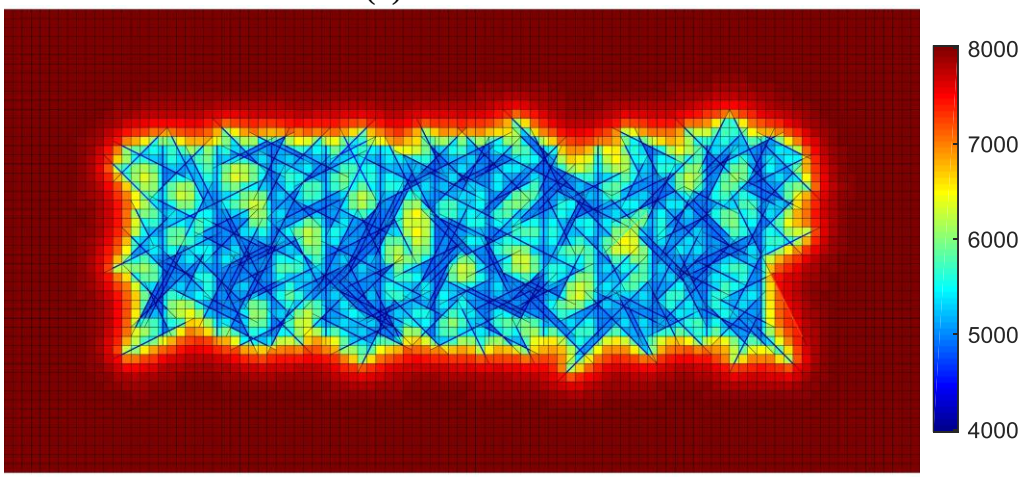

(c) t=60 months

Figure 6.3—Pressure profile of inorganic matrix for a hydraulic fractured horizontal well completed in shale formation.

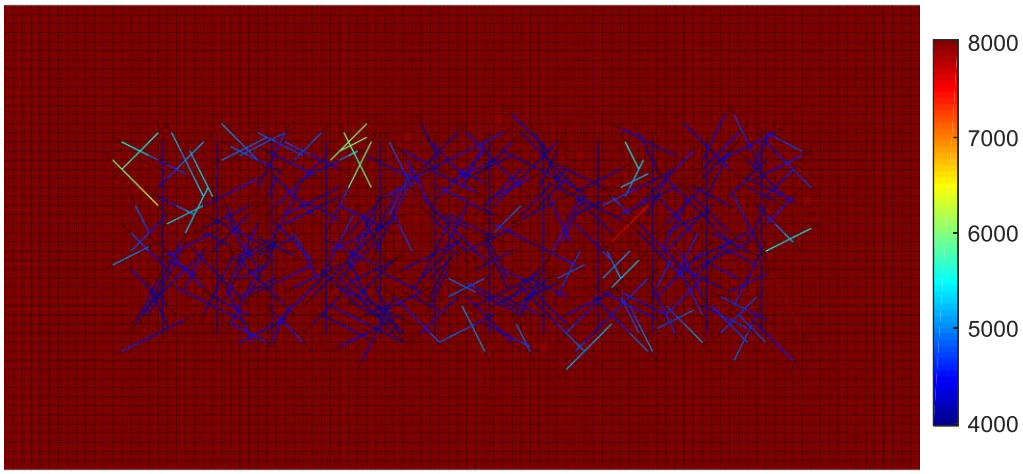

(a) t=1 months

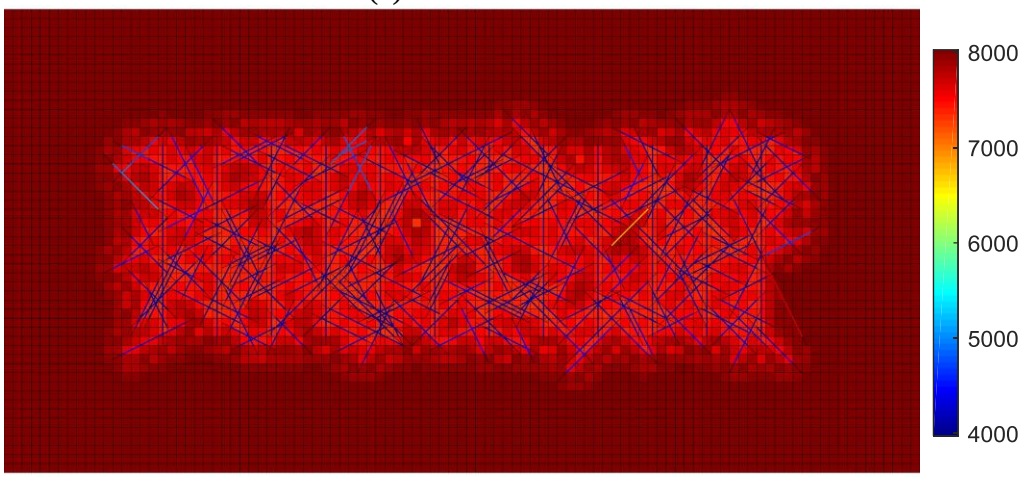

(b) t=12 month

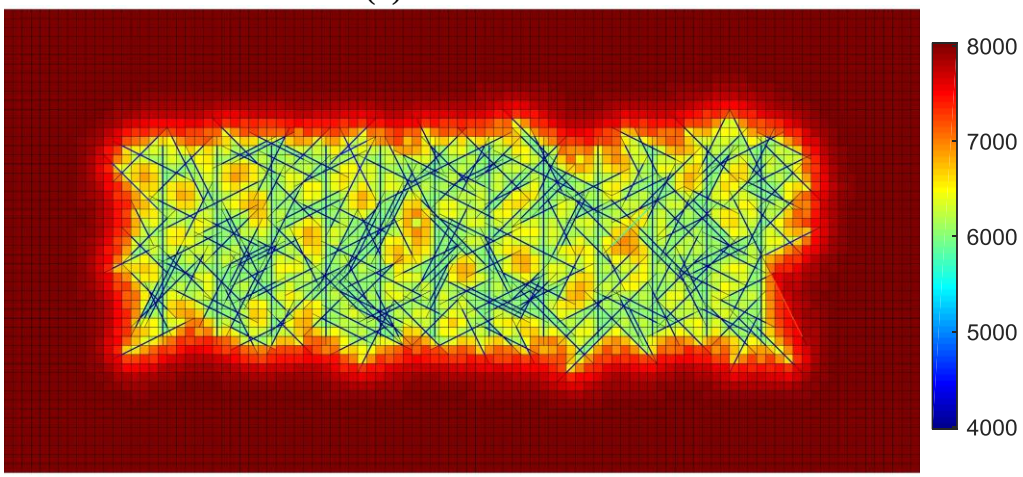

(c) t=60 months

Figure 6.4—Pressure profile of kerogen for a hydraulic fractured horizontal well completed in shale formation.

6.2 Horizontal Well Optimization with cEDFM

The well placement and completion design are vital factors that directly impact the profitability of the well. Here we take advantage of the flexibility of the cEDFM approach, and perform optimization to well completion design and well spacing. **Figure 6.5** shows the horizontal well model for the optimization problem. The dimension along the x axis of the reservoir is fixed at 5000 ft, which stands for the assumed maximum obtainable wellbore length for the horizontal section. The dimension along the y axis is adjustable, which stands for the well spacing perpendicular to the direction of the wellbore. We assume the hydraulic fractures are evenly spaced with the first and the last stage passing the heel and toe of the horizontal interval respectively. The wellbore length as well as the number of hydraulic fracturing stages are both parameters to be optimized. The half-length of the hydraulic fractures is fixed at 500 ft. It is a gas filed and the objective function for the optimization is the NPV of the well after 20 years of production. The parameters to calculate the objection function are listed in **Table 6.2**.

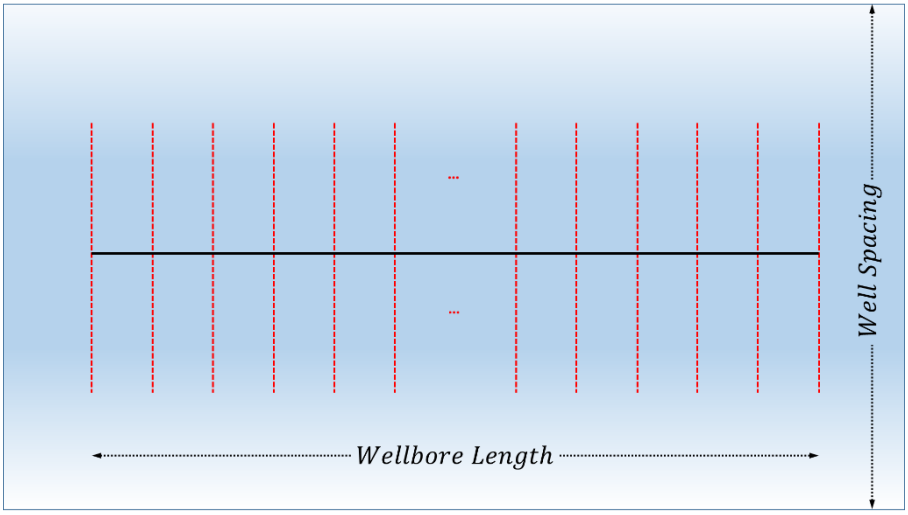

Figure 6.5—Model illustration of the optimization case.

The objective function is defined as:

$$Obj = revenue - C_{lease} - C_{drilling} - C_{completion} \quad (6.01)$$

$$revenue = \sum_{t=1}^{n_t}(1 - r_{tax}) \times \frac{(CPG_t - CPG_{t-1}) \times I_{gas} \times (1 - r_{royalty}) - S_m}{(1 + r_{discount})^t} \quad (6.02)$$

where: I_{gas} is the unit gas price, S_m is the monthly maintenance fee of the well, and CPG_t is the cumulative gas production at the end of time step t.

Table 6.2—Parameters for NPV calculation.

$reservoir\ depth$	8000 ft
$lease\ cost$	1000 \$/$acre$
$drilling\ cost - vertical\ section$	200 \$/ft
$drilling\ cost - horizontal\ section$	280 \$/ft
$completion\ cost -\ hydraulic\ fracturing$	1.0×10^5 \$/$stage$
$gas\ price$	3.0×10^3 \$/$mmscf$
$well\ maintenance\ cost$	150 \$/day
$discount\ rate, monthly$	0.01
$royalty$	15%
$tax\ rate$	30%
$well\ maintenance\ cost$	150 \$/day

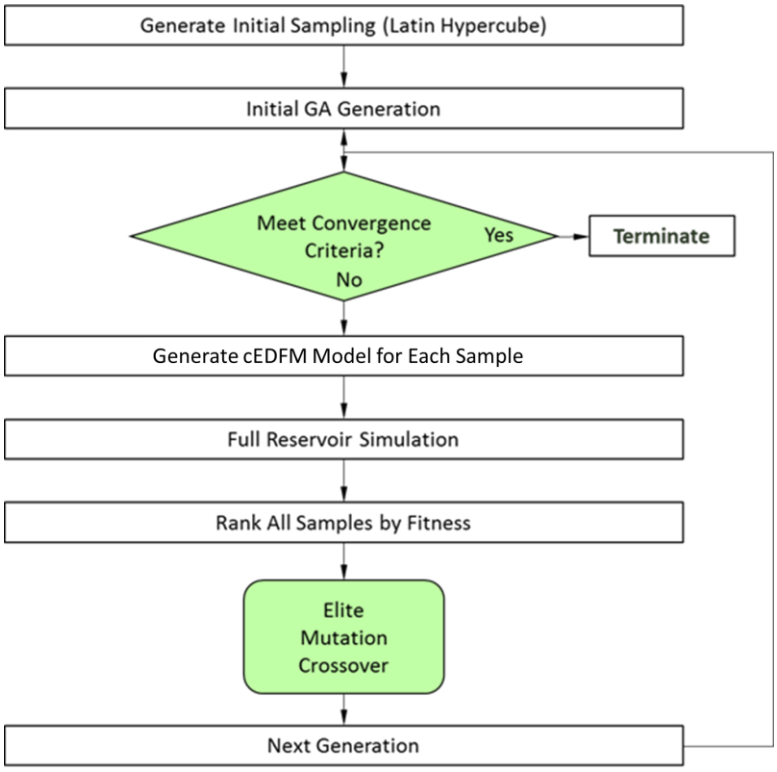

Figure 6.6—Horizontal well design optimization workflow with GA.

The workflow of the GA optimization is illustrated in **Figure 6.6**. An initial generation of samples is first generated from Latin Hypercube design to fully cover the parameter space. The reservoir models are then generated and the simulation is performed for each of the cases. The population would then be ranked by "fitness", which is the NPV after 20 years of production. Finally, the next generation of samples is generated. The process is repeated until a convergence criterion is met, which is when the increase of NPV for the best case is below 2% for two consecutive generations.

A population of 50 is used for this problem, among which, 20% of the "elite" samples with the highest NPVs are preserved to the next generation, 20% are generated by directly mutating from the previous generation, and the rest 60% are generated by performing "crossover" among the previous generation samples. The numerical value for each of the parameters is converted to a

binary string, a length of 7 is chosen in this case to control the granularity of the values. The "chromosome" of each case is then generated by concatenating all the binary strings.

Table 6.3—Well design optimization results.

	Base Case	Optimal Case
Well spacing	2500 ft	3315 ft
HF stages	12	16
Wellbore length	3500 ft	4440 ft
NPV	3.61 Million $	4.62 Million $

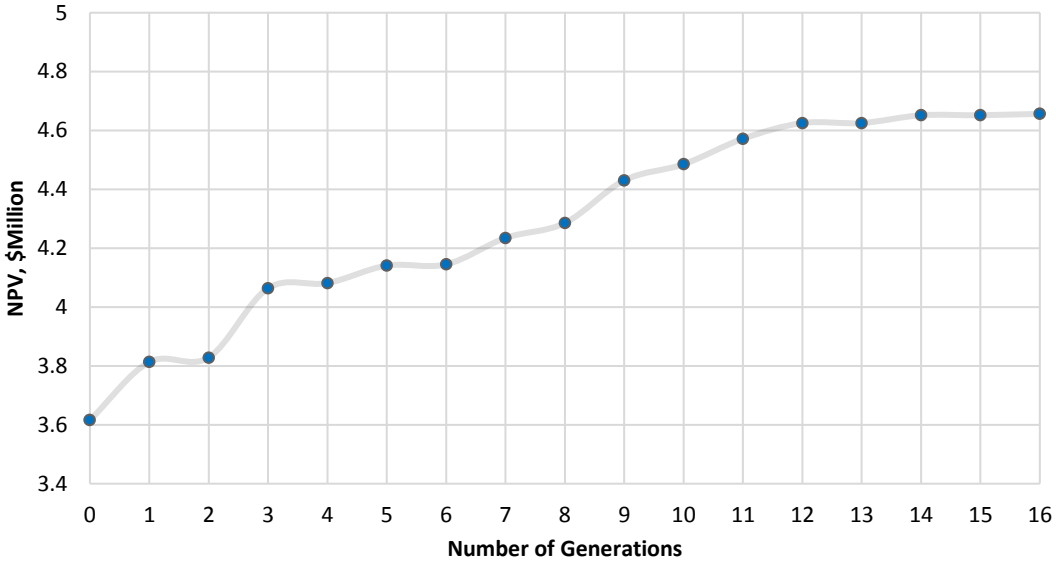

Figure 6.7—Net present value of the optimal case vs. generation.

After the next generation is generated, the parameter values are obtained by a reverse conversion from the binary strings. It took 16 generations before the solution reaches convergence, and the NPV of the best case in each of the generations is plotted in **Figure 6.7**. The results of the optimization are listed in **Table 6.3**. Compared to the base case design, an optimal development can be obtained by increasing the well spacing from 2500 ft to 3315 ft, increase the wellbore length from 3500 ft to 4440 ft, and increase the hydraulic fractures from 12 stages to 16 stages.

6.3 Dynamic Fracture Network

Studies such as Suarez-Rivera, R. et al. (2013) and El Sgher, M. et al. (2018) have shown that the conductivity of the fractures changes greatly as the effective stress changes. For low permeable resources such as shale, the reservoir is usually developed by depletion without maintaining the reservoir pore pressure. As a result, the effective pressure gradually increases and impairs the conductivity of the fracture network.

From the work of Zhang, J. et al. (2014), the relationship between the pore pressure drop and the conductivity can be generalized to:

$$C_d = \delta \times e^{-\beta\alpha\Delta P} \quad (6.03)$$

where: δ, β and α are all constant coefficients. The normalized fracture conductivity is therefore:

$$\overline{C_{d,p}} = \frac{\delta \times e^{-\beta\alpha\Delta P}}{\delta \times e^{0}} = e^{-\beta\alpha\Delta P} \quad (6.04)$$

where: α is the fracture compaction coefficient that is formation specific, and β account for the properties of the proppant, or when the fractures are unpropped.

By assigning different values for α, the normalized conductivity for propped and unpropped fracture are plotted in **Figure 6.8** and **Figure 6.9**. Here we assume $\beta_{up} = 1$ and $\beta_p = 0.5$ for unpropped and propped fractures respectively, and an initial pore pressure of 8000 psi.

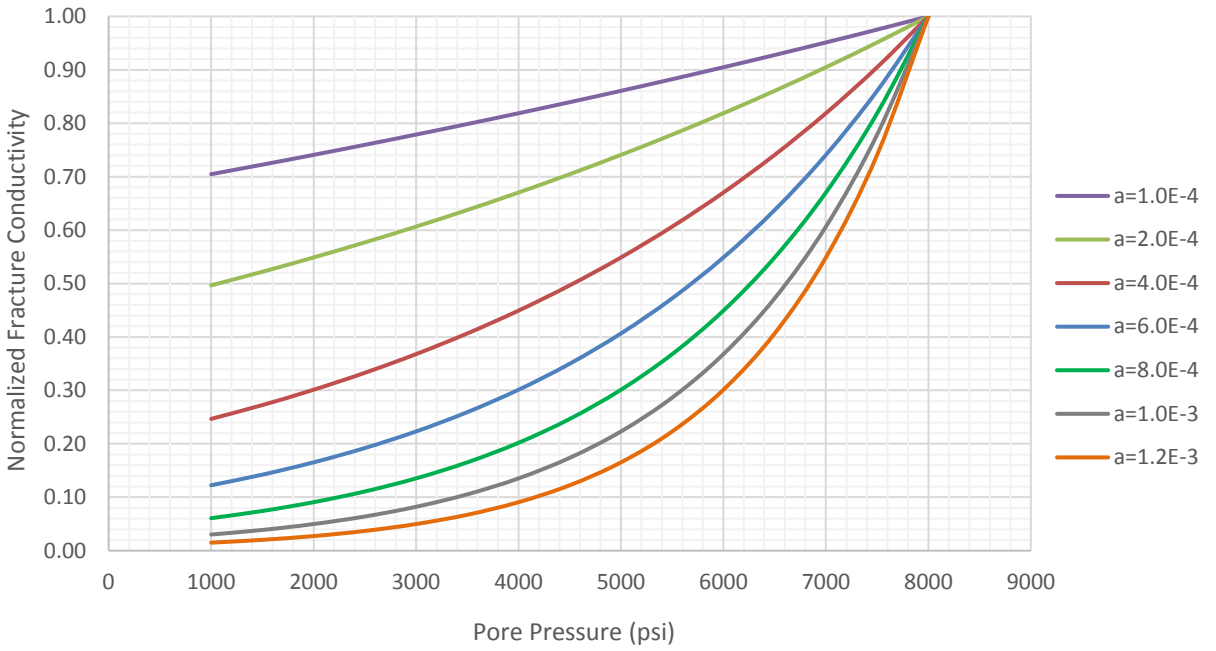

Figure 6.8—Compaction curve of propped fracture conductivity.

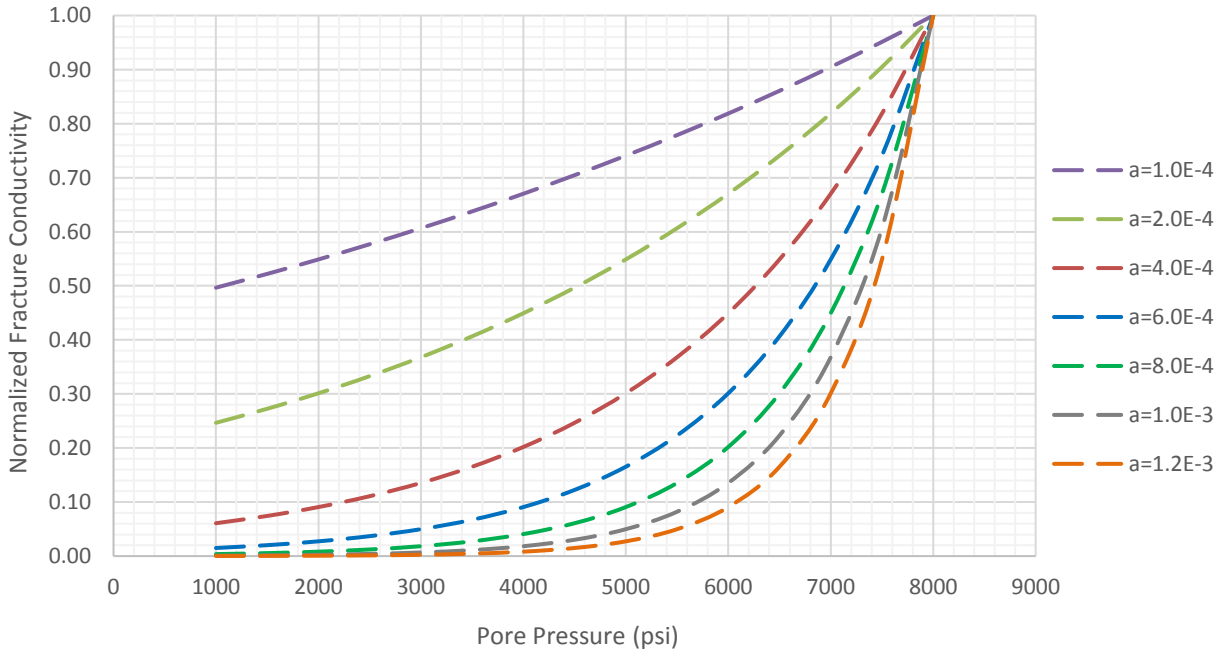

Figure 6.9—Compaction curve of unpropped fracture conductivity.

Table 6.4—Model parameters for the dynamic fracture conductivity case.

$Reservoir\ dimension$	$8640\ ft \times 2430\ ft \times 30\ ft$
$Parent\ matrix\ mesh$	$288 \times 81 \times 1$
ϕ	0.10
k_{matrix}	$5.0 \times 10^{-3} md$
$k_{fracture}$	$1.0 \times 10^{3} md$
$w_{fracture}$	$0.05\ ft$
$Reservoir\ fluid$	$100\%\ methane$
$Wellbore\ radius$	$0.25\ ft$
BHP	$2500\ psi$
Pi	$8000\ psi$
T	$180\ F^{o}$

Below we studied the influence of fracture compaction on well production. The model parameters for this case study are listed in **Table 6.4**. A horizontal well is producing at a constant BHP from a gas reservoir, with 12 stages of hydraulic fractures. Here we randomly select 50% of the fractures to be effectively propped, and the rest to be unpropped. The transmissibility between the fracture grids and other grids would be updated dynamically based on the value of $\overline{C_{d,p}}$ and $\overline{C_{d,up}}$, which is determined by the current pore pressure and the value of the compaction coefficient.

Figure 6.10 shows the pressure profile after 10 years of production with different values of the compaction coefficient. It is obvious that the drainage is much less effective for the case with a larger α value. The production is greatly affected, as can be seen in **Figure 6.11**. Therefore, fracture compaction is an important factor to be considered for fractured reservoir simulation to have an accurate estimation of the well performance.

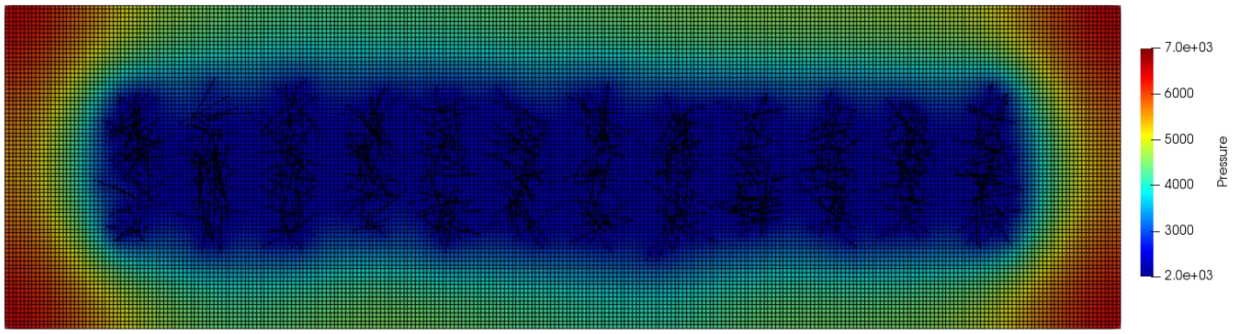

(a) $\alpha = 1.0E-4$

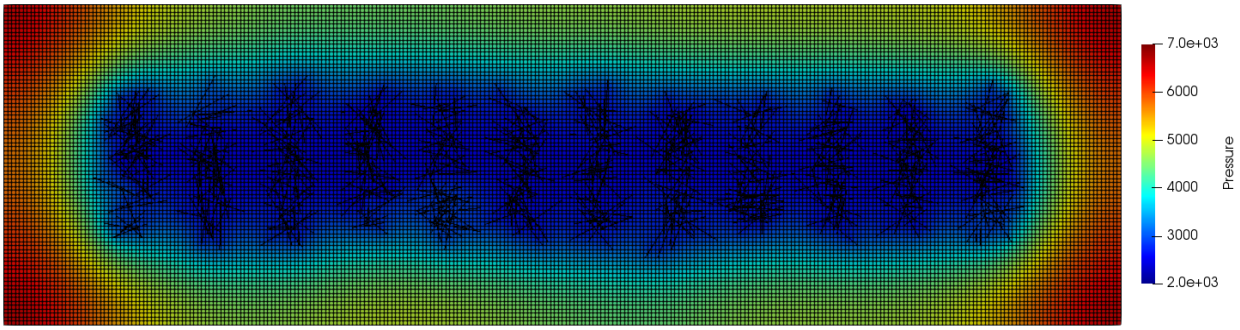

(b) $\alpha = 6.0E-4$

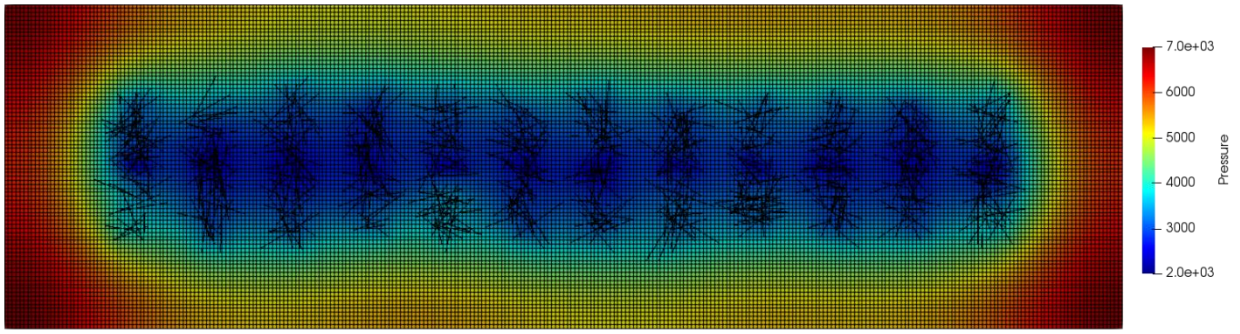

(c) $\alpha = 1.2E-3$

Figure 6.10—Pressure profile after 10 years of production.

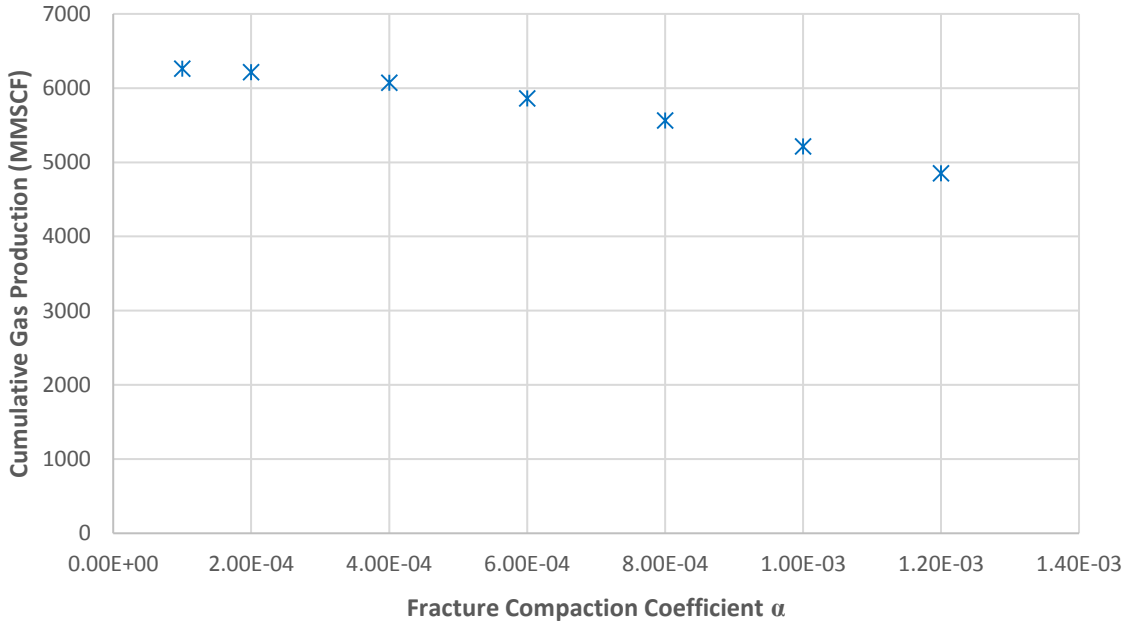

Figure 6.11—Cumulative gas production with different compaction coefficient α.

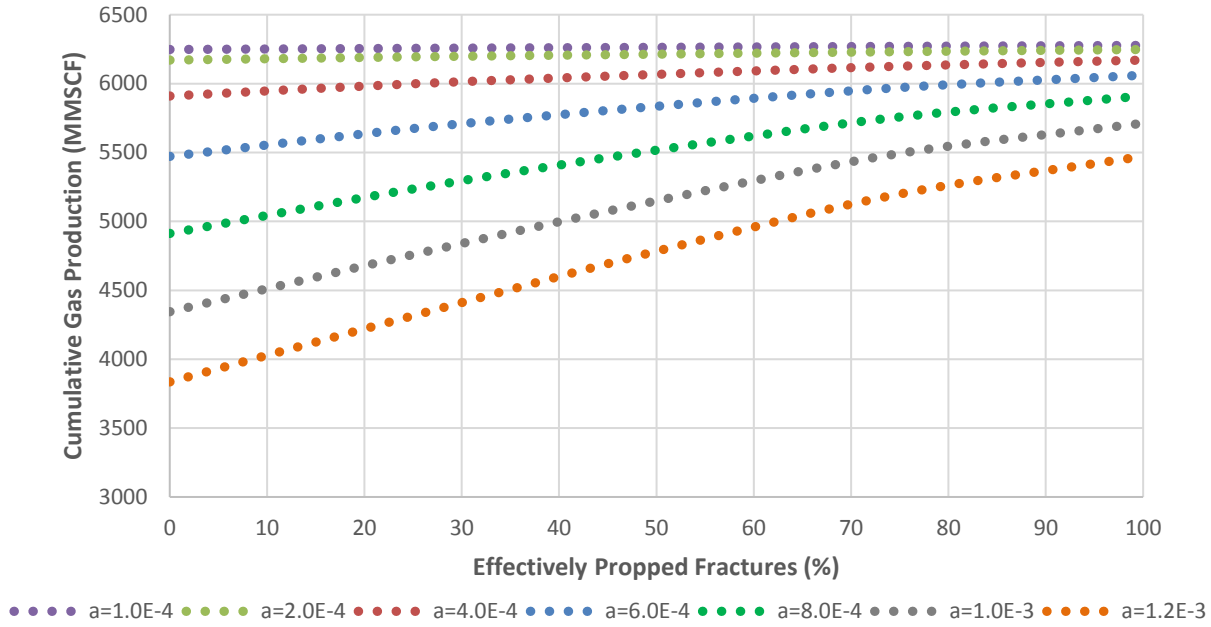

Figure 6.12—Cumulative gas production with different percentage of effectively propped fractures.

Figure 6.12 shows the influence to cumulative production of gas when the percentage of effectively propped fracture changes. For formations with a small fracture compaction coefficient,

the influence is minor. However, for formations with a larger fracture compaction coefficient, the production is more significantly influenced by fracture compaction. Therefore, it is more important for these reservoirs to effectively prop the fractures in order to maintain a high recovery rate.

CHAPTER VII[3]

FRACTURED RESERVOIR HISTORY MATCHING WITH MCMC

Quantifying the uncertainty of the fracture network is a vital part to really understand the reservoir dynamics for fractured reservoirs. In this chapter, a workflow based on Markov chain Monte Carlo (MCMC) is proposed to perform history matching for this type of reservoirs. All cases evaluated here use cEDFM as the forward model. The method allows for fast model generation and efficient reservoir simulation without losing accuracy, which ensured the performance of the history matching algorithms. Since no upscaling is needed, the result can be interpreted much more intuitively.

The MCMC algorithm is solely based on sampling. One advantage is that no gradient matrix needs to be calculated, which can be expensive to obtain. However, in order to avoid the low accept ratio of MCMC, we implemented and modified the approach of two-stage MCMC, which was first proposed by Ma, X. et al. (2008). The algorithm would greatly increase the accept rate of the proposed samples for simulation, and therefore reduce the cost for history matching.

The flowchart for the history matching process with the two-stage MCMC is shown in **Figure 7.1**. A stochastic sample is generated from the prior PDF as the starting point of the MCMC chain. In the first stage of the MCMC sampling, a proxy model is used to estimate the posterior probability of the proposal, and the proposal is either accepted or rejected based on the Metropolis-Hastings criterion. Only the proposals that are accepted in the first stage would generate the reservoir model and run the full simulation. In the second stage, the proposal is either accepted or

[3] Part of this chapter is reprinted with permission from "Chai, Z., Yan, B., Killough, J., & Wang, Y. An efficient method for fractured shale reservoir history matching: The embedded discrete fracture multi-continuum approach." Copyright [2017] by Elsevier.

rejected based on the same Metropolis-Hastings criterion, the only difference is that the posterior probability is calculated with the actual simulation result.

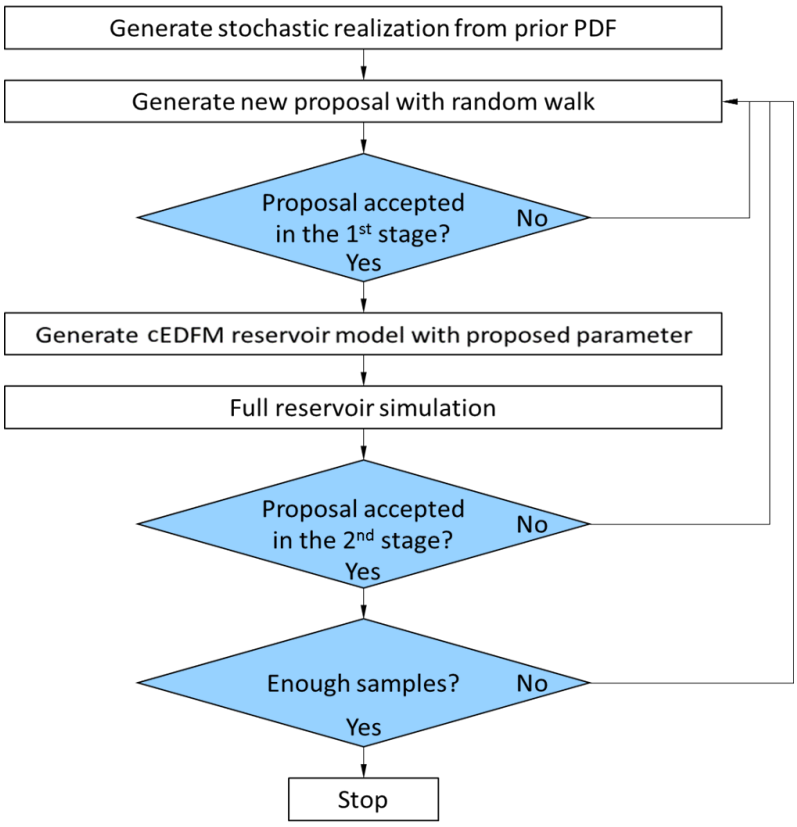

Figure 7.1—Flowchart of history matching and uncertainty quantification of fractured shale reservoirs with cEDFM.

7.1 Markov Chain Monte Carlo (MCMC)

MCMC is a class of method for sampling that aims to generate samples from a target probability distribution for which direct sampling is difficult. Here, history matching and uncertainty quantification are performed through the sampling of model parameters. Samples are generated along the Markov chain, where the next state on the chain (x_{t+1}) depends only on the current one (x_t):

$$P(x_{t+1} = s_j | x_0 = s_0, \dots, x_t = s_t) = P(x_{t+1} = s_j | x_t = s_t) \quad (7.01)$$

MCMC has been applied in reservoir engineering to solve the inverse problem by sampling a posterior distribution that contains information from both a prior distribution of the parameters and observed well production data. The posterior distribution is defined as:

$$P(x|d_{obs}) \propto \exp\left\{-\frac{1}{2}[(x-\mu_x)^T C_x^{-1}(x-\mu_x) + (g(x)-d_{obs})^T C_D^{-1}(g(x)-d_{obs})]\right\} = \pi(x) \quad (7.02)$$

In such problems, a sequence of samples is generated in the Markov chain whose stationary density represents the updated reservoir description. Metropolis Hasting (M-H) is one of the sampling algorithms that could generate an MCMC chain. The advantage of M-H is that it does not require knowing the normalizing constant of the target distribution. The steps to generate an MCMC chain using M-H algorithm can be summarized as follows:

1) The chain starts by drawing a random state x_n.
2) A candidate state x is then drawn from a proposal distribution $q(\cdot)$.
3) With the current value x_n and the candidate value x, the probability of the move α from x_n to x is calculated by:

   $$\alpha(x_n, x) = \min\left(1, \frac{\pi(x)\, q(x_n|x)}{\pi(x_n)\, q(x|x_n)}\right) \quad (7.03)$$

4) The candidate is accepted with a probability of α and rejected with a probability of $1-\alpha$.

When the candidate is accepted, it is retained in the chain and its value is used to determine the next member in the chain. Otherwise, the candidate is discarded and the previous steps are repeated. After a sufficient burn-in period, the Markov chain reaches a stationary distribution, and it could represent the target distribution when enough samples are generated. If a symmetric

proposal distribution is used, which is usually the case, the ratio of the proposal distributions in the equation above is equal to 1, and the acceptance probability is simply:

$$\alpha(x_n, x) = \min\left(1, \frac{\pi(x)}{\pi(x_n)}\right) \quad (7.04)$$

A drawback of the application of original MCMC in reservoir history matching is that it is computationally expensive. The burn-in stage could be long before the Markov chain could converge to a stationary distribution. Additionally, since each iteration requires running a full reservoir simulation, and the rejection ratio related to such problems are usually high, the process becomes highly inefficient as a large part of the simulations are discarded.

7.2 Two-Stage MCMC

To deal with the high cost of computation associated with the original MCMC, a two-stage MCMC algorithm is implemented. The idea is to add an additional selection process to filter away poor proposals that are not likely to be accepted before passing it to the reservoir simulator. The algorithm is first proposed by Ma, X. et al. (2008) and the steps can be summarized as:

1) The simulation result is first estimated by a linear approximation based on the parameter values of the proposal in the first stage. The sample is accepted by the M-H acceptance criteria using the approximated model response.

   $$\alpha(x_n, x) = \min\left(1, \frac{\pi^*(x)}{\pi^*(x_n)}\right) \quad (7.05)$$

2) If the sample is accepted in the 1st stage, a full reservoir simulation is then performed and the sample is accepted by the following probability in the 2nd stage:

   $$\rho(x_n, x) = \min\left(1, \frac{Q(x_n|x)\pi(x)}{Q(x|x_n)\pi(x_n)}\right) \quad (7.06)$$

where: $Q(x|x_n)$ is the proposal distribution at the 2nd stage, and we have:

$$Q(x_n|x) = \alpha(x, x_n)q(x_n|x) \quad (7.07)$$

Using the equation above, with a symmetric proposal distribution, it can be shown that the acceptance probability at the second stage is simply:

$$\rho(x_n, x) = min\left(1, \frac{\pi(x)\pi^*(x_n)}{\pi(x_n)\pi^*(x)}\right) \quad (7.08)$$

For $x = x_n$ this is obviously true. For $x \neq x_n$, it can be proven as follows:

$$Q(x_n|x) = \min\left(1, \frac{q(x|x_n)\pi^*(x_n)}{q(x_n|x)\pi^*(x)}\right) q(x_n|x) = \min\left(q(x_n|x), \frac{q(x|x_n)\pi^*(x_n)}{\pi^*(x)}\right) \quad (7.09)$$

$$Q(x_n|x) = \frac{1}{\pi^*(x)} \min\left(q(x_n|x)\pi^*(x), q(x|x_n)\pi^*(x_n)\right) \quad (7.10)$$

$$Q(x_n|x) = \frac{q(x|x_n)\pi^*(x_n)}{\pi^*(x)} \min\left(\frac{q(x_n|x)\pi^*(x)}{q(x|x_n)\pi^*(x_n)},\ 1\right) = \frac{\pi^*(x_n)}{\pi^*(x)} Q(x|x_n) \quad (7.11)$$

$$\frac{Q(x_n|x)}{Q(x|x_n)} = \frac{\pi^*(x_n)}{\pi^*(x)} \quad (7.12)$$

7.3 Generate the Proxy Model

The original approach for the two-stage MCMC is to assume local linearity of the model and estimate model response at the perturbed parameter value using:

$$g^*(x) = g(x_n) + G\delta x \quad (7.13)$$

where: G is the sensitivity matrix, with G_{ij} being the partial derivative of the observed data i to model parameter j.

The result above would be used to calculate the estimated posterior:

$$P^*(x|d_{obs}) \propto \exp\left\{-\frac{1}{2}[(x-\mu_x)^T C_x^{-1}(x-\mu_x) + (g^*(x)-d_{obs})^T C_D^{-1}(g^*(x)-d_{obs})]\right\} \ldots (7.14)$$

The extra layer of filter of the two-stage MCMC is supposed to filter away the majority of the poor proposals and increase the percentage of promising proposals in the second stage where full simulation is performed. However, in our case the poor accuracy of the sensitivity matrix G calculated with perturbation may lead to a poor performance of the two-stage MCMC for the following reasons:

1) Since the whole purpose of the two-stage MCMC is to reduce the simulation cost, the G matrix is not updated for each of the proposals.
2) The value at which the parameters are perturbed would greatly affect the value of G, especially when the parameters are fracture properties. At different base parameter values, the calculated G varies greatly, therefore it is inaccurate for most cases, leading to a poor estimation of the model response.

The original two-stage MCMC did not effectively improve the acceptance ratio in our application, and sometimes may even be counterproductive. Therefore to improve the performance of the algorithm, we used a proxy model instead to estimate the model response, with the response defined as the mismatch of the data (corresponding to the likelihood):

$$response = (g^*(x)-d_{obs})^T C_D^{-1}(g^*(x)-d_{obs}) \ldots\ldots (7.15)$$

Therefore, the proxy model would estimate the likelihood without running an actual simulation. To build the proxy model, a training dataset needs to be created first for regression analysis, as would be discussed in the following case study.

7.4 Case Study

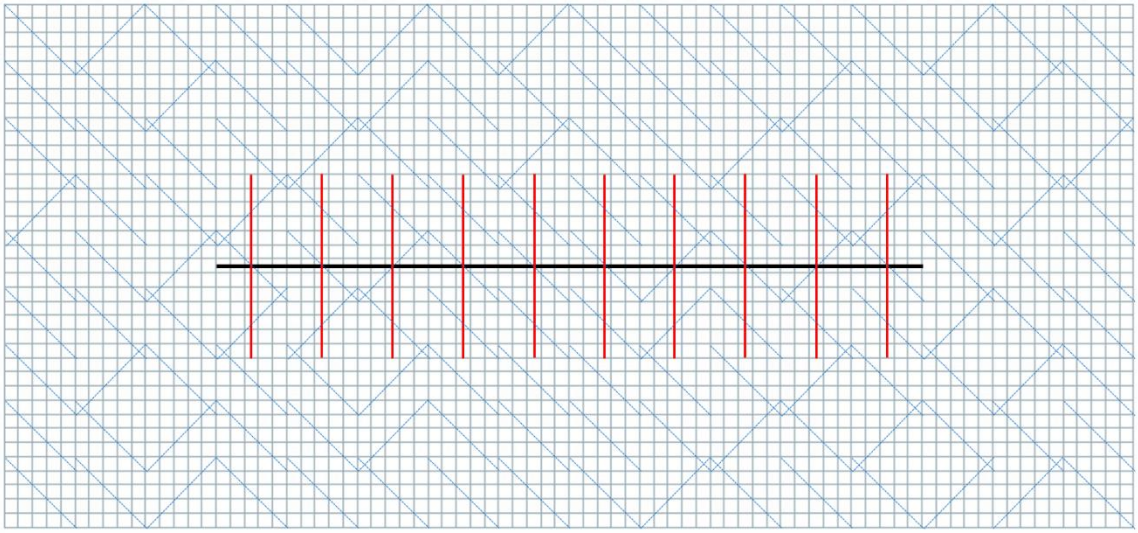

Figure 7.2—Example case reservoir model. Single horizontal well with 10 stages of hydraulic fractures (in red) and the interacting natural fractures (in blue). Uncertainty is introduced from the distribution and conductivity of the natural fractures, as well as the properties of the shale matrix.

The workflow can be illustrated with the following example case. A horizontal well with 10 stages of hydraulic fractures is producing at a constant BHP, as shown in **Figure 7.2**. Natural fractures are uniformly distributed throughout the reservoir. Here we assume natural fractures are distributed with certain pattern, and statistical averages of the fracture properties are assigned to all natural fractures, such as length, width and conductivity. Previous outcrop and core studies of naturally fractured reservoirs such as Nelson, R. (2001) have indicated that natural fractures follow a dominant strike angle as well as a secondary strike angle in general, which correspond to the directions of maximum and minimum geo-stress. Therefore here we define the strike angle of the natural fractures in one of two dominant directions, and the uncertainty of the fracture network can be described by the percentage of the fractures in the secondary strike angle. Its value as well as the fracture length and conductivity would control the fracture network connectivity, therefore

determine the performance of the well. For this case with a single well drainage problem, matrix grid splitting is skipped since the simulation result would not be affected.

Since in this model, all parameters can be directly set as history matching parameters, and no upscaling is needed, we can assume all parameters conform to a truncated Gaussian distribution, with the prior distribution specified in **Table 7.1**. The prior PDF and the true value of all parameters in the reference case are plotted in **Figure 7.3**.

Table 7.1—Prior distribution and reference value of the example case.

Parameter	Mean	Standard Deviation	True Value
Fracture length / ft	75	30	55
Matrix permeability / md	5×10^{-5}	2.0×10^{-5}	7.0×10^{-5}
Secondary strike angle percentage	0.25	0.1	0.15
Natural fracture conductivity / md-ft	4	1.5	3.2

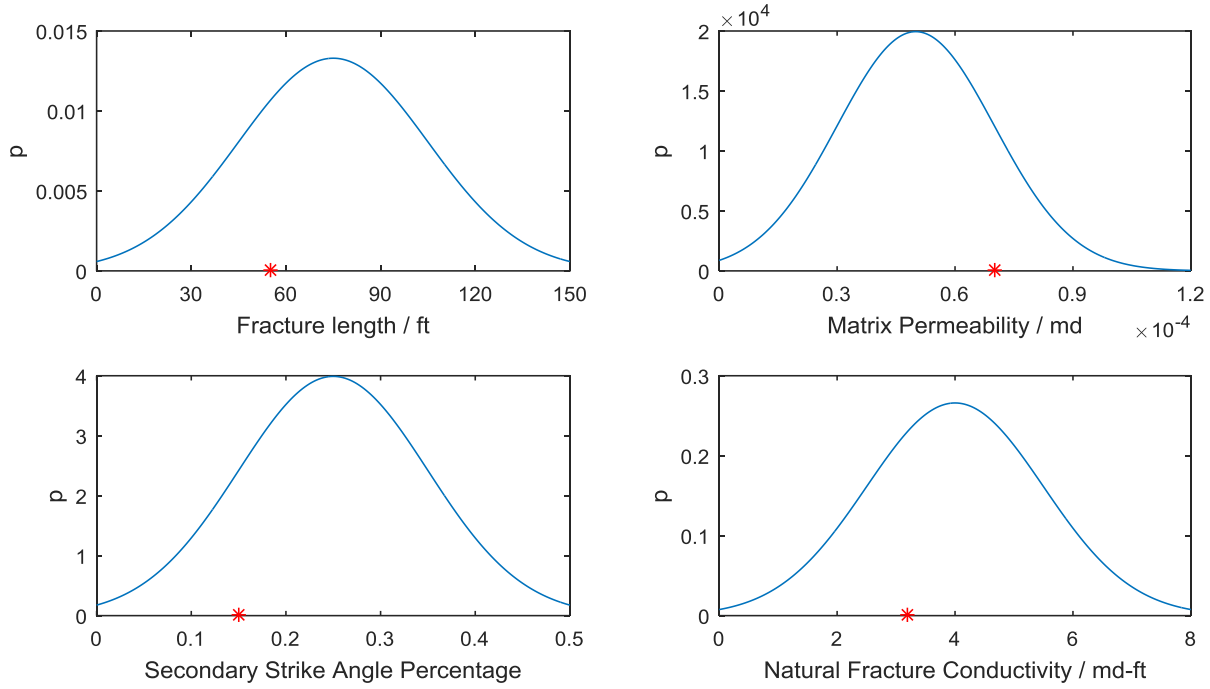

Figure 7.3—Prior PDF and true value for the reference case.

A sensitivity analysis is performed on the model parameters to optimize parameters for history matching. Below in **Figure 7.4** is the tornado plot of the cumulative oil production with each parameter perturbed by its corresponding single standard deviation according to the prior PDF. The results indicate that the production is sensitive to fracture length and secondary strike angle percentage, which both have direct impact to the fracture network connectivity. Increasing the two parameters would enhance the connectivity of the fracture network, which increases the drainage volume. And a higher matrix permeability is also conducive to a higher well production rate as expected. However, the conductivity of natural fractures does not have a noticeable impact on well production, since the bottleneck for mass transfer from the matrix to the fracture system is the permeability of the matrix. Even though a large uncertainty exists for the conductivity of the natural fractures, it cannot be resolved with a case such as this one, which has an ultra-low permeability for the shale matrix. Therefore, length and secondary strike angle percentage of

natural fractures and matrix permeability are chosen as history matching parameters, and fracture conductivity is set to be a constant value due to its negligible impact. Note that natural fracture strike angles are randomly assigned to each fracture to better describe the uncertainty of the fracture distribution.

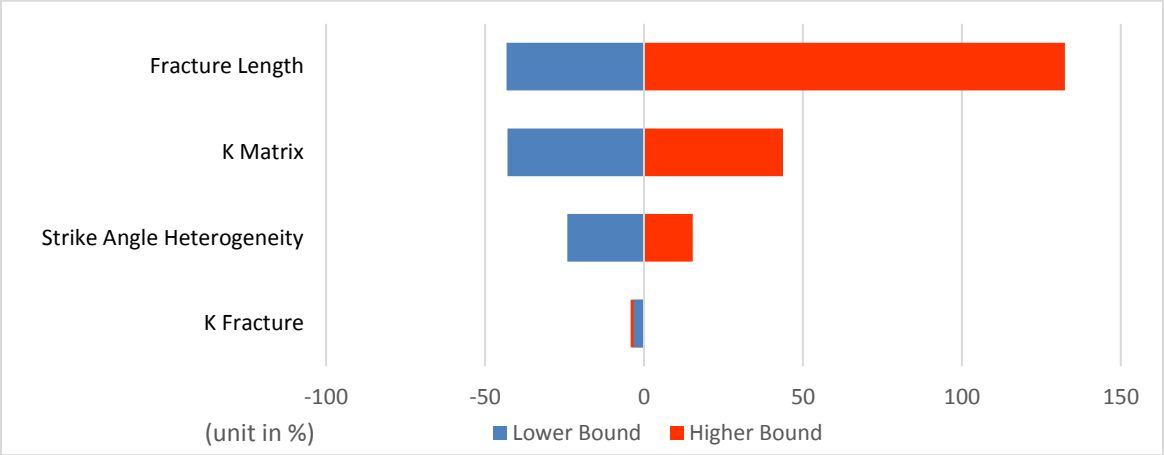

Figure 7.4—Tornado plot of cumulative oil production with respect to model parameters.

A training dataset is first created by sampling from the parameter space based on full factorial design. 150 data points are generated, with the corresponding reservoir models generated and the simulations performed. Here neural network is used as the regression model to get the approximated relationship between the reservoir parameters (i.e. the input) and the well data mismatch measured by the likelihood (i.e., the output). **Figure 7.5** shows the structure of the neural network, with a single hidden layer besides the input and the output layers. One third of the data is kept for testing and two thirds for training. The result of the testing cases is shown in **Figure 7.6**, with an accuracy of around 0.93 obtained on the testing data. The number of hidden layers and the number of neurons in each layer are optimized based on the testing result through grid search. It shows that a more complexed structure tends to over-fit the data, while the simple

configuration in **Figure 7.5** proved to be adequate to provide an estimation with an acceptable accuracy, therefore able to select promising proposals for simulation.

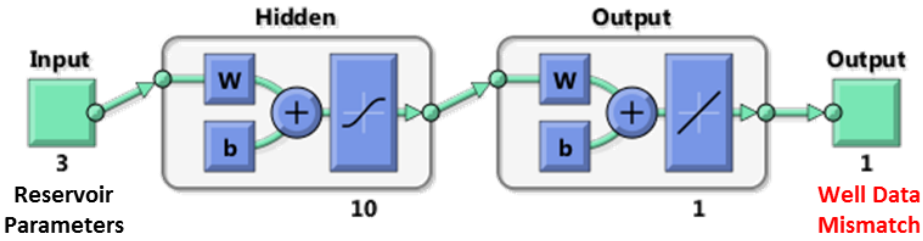

Figure 7.5—Neural Network set-up for training the proxy model.

To start the Markov chain, a stochastic sample is generated from the prior PDF, then a new proposal is generated with random walk, which can be calculated as:

$$x = x_n + \sigma\varepsilon \quad (7.16)$$

where: ε is a random perturbation, and σ is a positive number to control the step size. σ should be large enough to fully explore the whole range of the parameters, while small enough so as to obtain a reasonable acceptance rate. Here, ε is sampled from a normal distribution with a mean of 0 and a standard deviation same as in the prior probability density function of the parameters. To control the step size, a value of $\sigma^2 = 0.05$ is used here. The proposal is accepted with the possibility of:

$$\alpha(x_n, x) = \min\left(1, \frac{\pi^*(x)}{\pi^*(x_n)}\right) \quad (7.17)$$

If the proposed sample is accepted in the first stage, the parameter values would be used to generate a new reservoir model, and a full simulation is carried out to obtain the exact reservoir response. After completion of the simulation, the proposal is accepted in the second stage with the probability of:

$$\rho(x_n, x) = min\left(1, \frac{\pi(x)\pi^*(x_n)}{\pi(x_n)\pi^*(x)}\right) \quad (7.18)$$

In which:

$$\pi(x) = \exp\left\{-\frac{1}{2}[(x-\mu_x)^T C_x^{-1}(x-\mu_x) + (g(x)-d_{obs})^T C_D^{-1}(g(x)-d_{obs})]\right\} \quad (7.19)$$

$$\pi^*(x) = \exp\left\{-\frac{1}{2}[(x-\mu_x)^T C_x^{-1}(x-\mu_x) + (g^*(x)-d_{obs})^T C_D^{-1}(g^*(x)-d_{obs})]\right\} \quad (7.20)$$

Note that $g^*(x)$ is the estimated reservoir response calculated with the proxy model, and $g(x)$ is the simulated reservoir response.

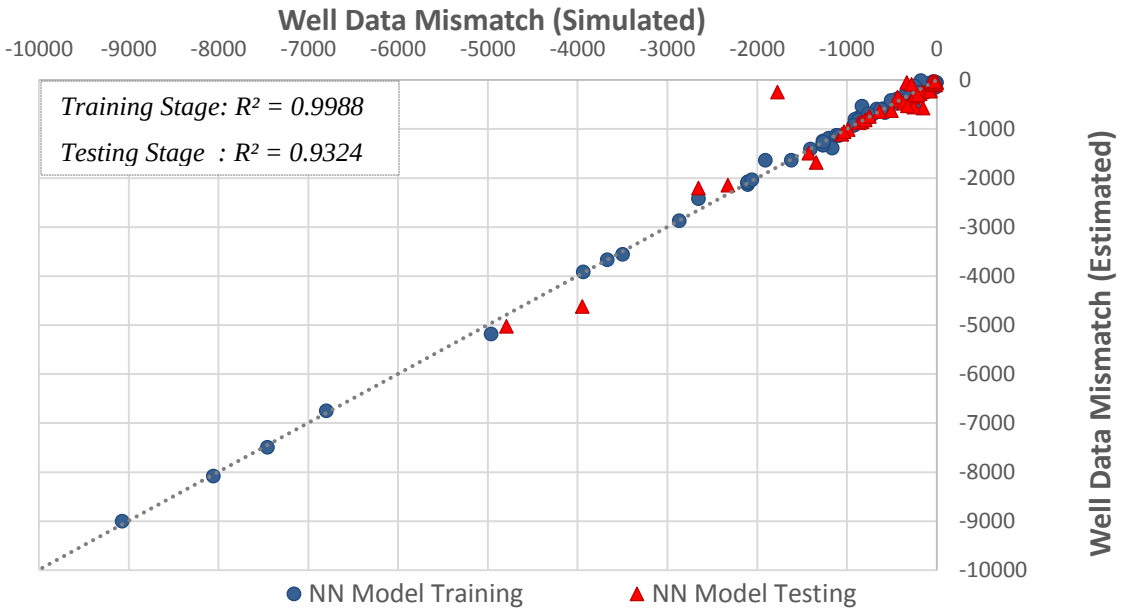

Figure 7.6—Well data mismatch (likelihood) from the proxy model vs. full simulation.

If the proposal is rejected in the first or the second stage, new parameter values are proposed until the proposal is accepted. The objective function of the accepted samples along the MCMC chain are plotted in **Figure 7.7**, with the objective function defined as:

$$Obj = \frac{1}{2}[(x-\mu_x)^T C_x^{-1}(x-\mu_x) + (g(x)-d_{obs})^T C_D^{-1}(g(x)-d_{obs})] \quad (7.21)$$

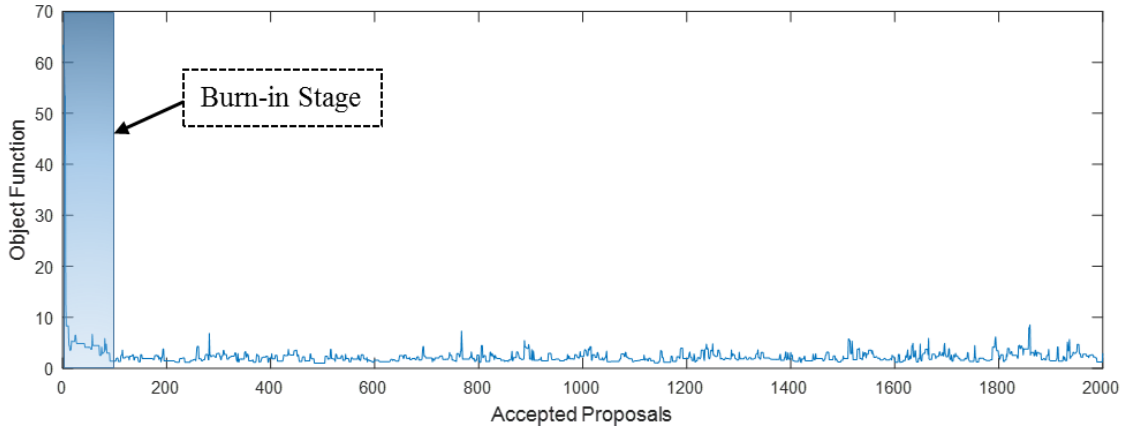

Figure 7.7—Objective function along the MCMC chain.

The burn-in stage is observed to be relatively short, after which the objective function reaches a relatively stationary state. There are 13,000 samples proposed in the run, and 15.50% of them are accepted in the first stage, among which 33.79% are accepted in the second stage. A relatively moderate step size is used in this case to avoid being trapped in a local minimum, while obtaining a reasonable acceptance rate at the same time in the first stage. The first 100 accepted samples are discarded, since the burn-in stage roughly ends there before the objective function reaches a stationary state. The boxplots of the parameters for the accepted proposals are shown in **Figure 7.8.** There is no noticeable fluctuation of the median along the chain, and the MCMC chain maintains in stationary.

The distribution of the accepted proposals is used to represent the posterior PDF and the updated reservoir description, as shown in **Figure 7.9** and **Figure 7.10**. Compared to the prior PDF, a much more concentrated distribution is obtained for the posterior PDF. The uncertainty for all parameters is significantly reduced, with the median of the posterior PDF moving towards the true value compared to the prior PDF.

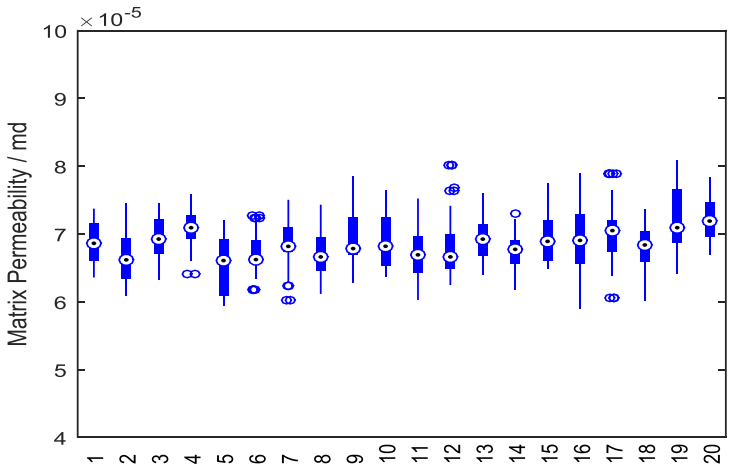

(a) Matrix Permeability

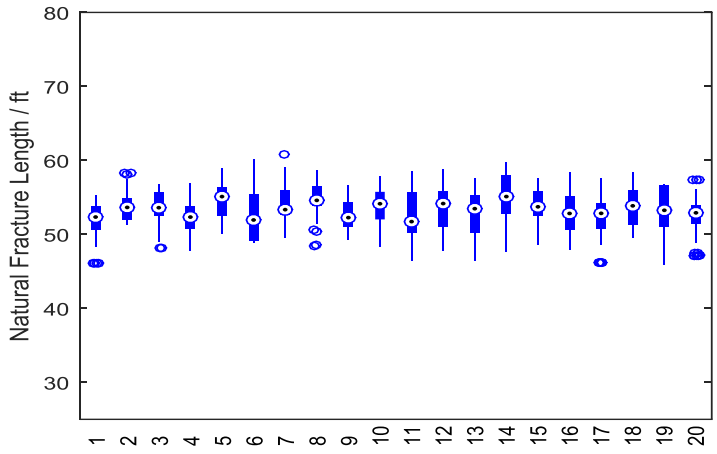

(b) Natural Fracture Length

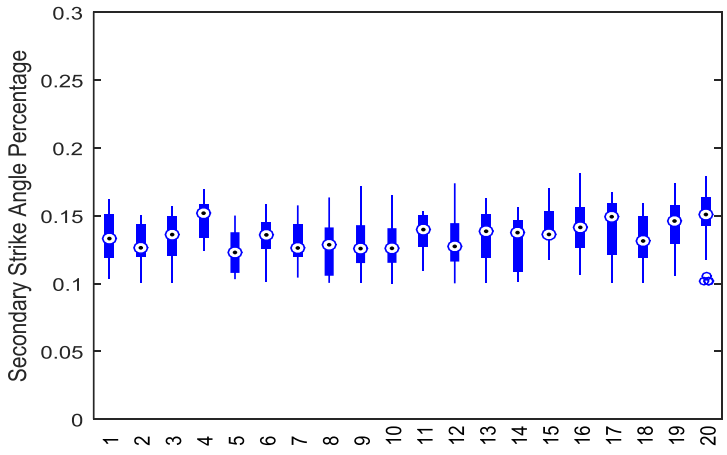

(c) Strike Angle Heterogeneity

Figure 7.8—Boxplot of the parameters along the MCMC chain, with each box representing 100 accepted samples.

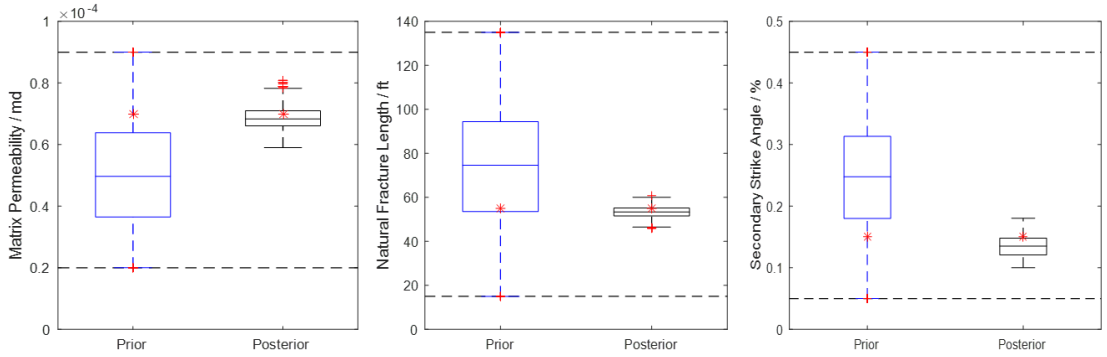

Figure 7.9—Box plot of the parameters from the prior distribution vs. posterior distribution. True values of the parameters are marked with red asterisks as a reference.

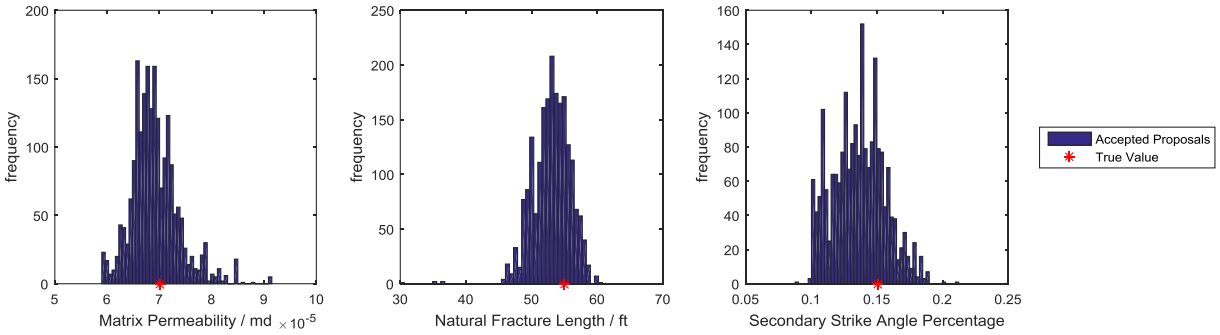

Figure 7.10—Histogram of the model parameters from the accepted samples.

Figure 7.11 illustrates the reduction of mismatch from the initial model to the updated models. The 50 best proposals are plotted against the observed data. An obvious improvement of the matching result is obtained for all the well data that are included in the objective function. In this case, the incorporated data includes the production rate and cumulative production of oil and gas.

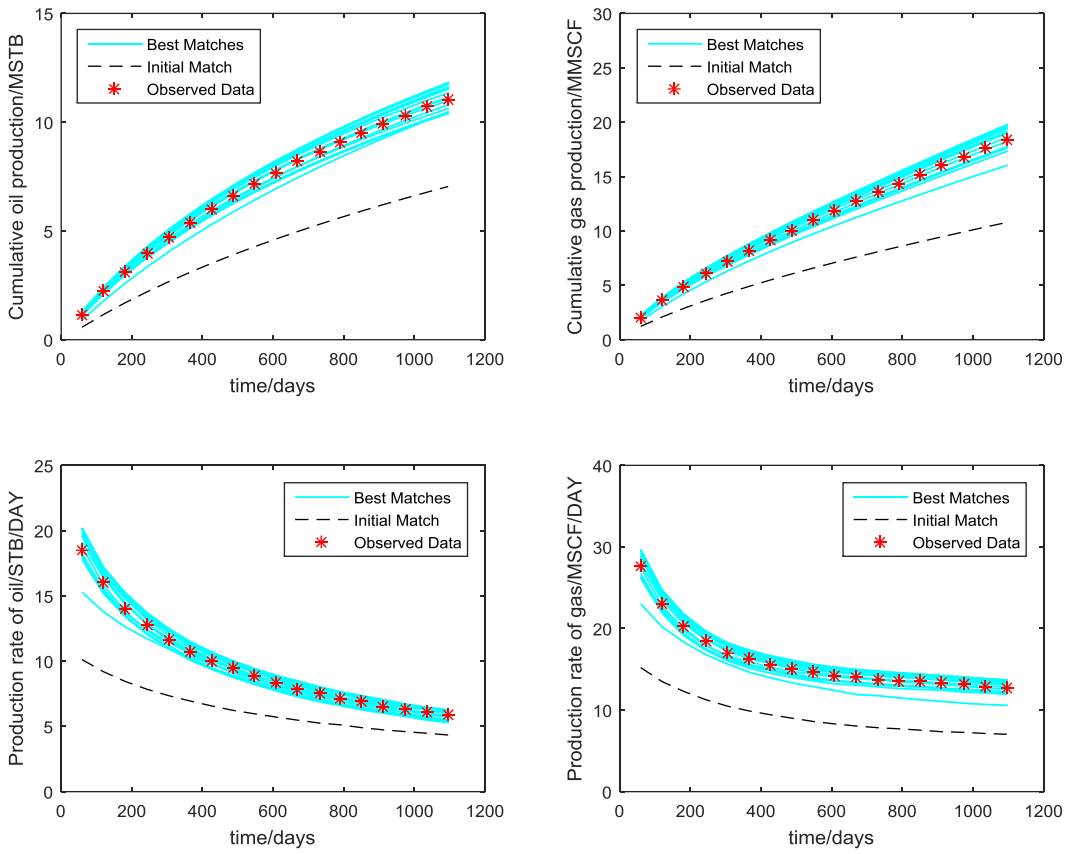

Figure 7.11—History matching result of the well data.

7.5 Summary

In this chapter, the proposed model is applied to work with the modified two-stage MCMC algorithm for history matching. Some results of this part include:

1) The implementation of two-stage MCMC and the use of proxy model prove to be effective in greatly improving the acceptance ratio and reducing the simulation cost. In the example case, a much higher accept ratio is obtained compared to the original MCMC algorithm.
2) It should be noted that the performance of the two-stage MCMC is largely influenced by the quality of the proxy model. Therefore, a larger training dataset, a more advanced experiment design and other parameterization methods are necessary for more complicated cases to build the proxy model.

3) As the problem becomes larger, the cost to generate the proxy model may not be compensated by the benefit, therefore other history matching algorithms may be more appropriate to be used.

CHAPTER VIII [4]

FRACTURED RESERVOIR HISTORY MATCHING WITH ENKF

The two-stage MCMC approach works well with a smaller parameter space. However, as the number of parameters increase, it becomes more and more expensive to generate the proxy model. Also, the accuracy of the proxy suffers when the training dataset is not large enough. Therefore, for larger problems, we implemented the more traditional ensemble approach. By using an explicit model such as cEDFM, the Gaussian distribution of the fracture parameters can be maintained, which is a prerequisite for many data assimilation algorithms. One advantage of the ensemble approach is that the computational cost is almost independent of the number of parameters, which makes it suitable for our case.

8.1 The Ensemble Approach for History Matching

The ensemble approach is the most widely used method in history matching. Among different implementations, the Ensemble Kalman Filter (EnKF) is the most well-studied. EnKF is a Monte Carlo based sequential data assimilation approach. It was first proposed by Evensen, G (2003), and the method consists of two steps: the forecasting step and the assimilation step. Initially, an ensemble is generated by sampling from the prior PDF of the parameter space, and the model-state realizations are created. The model-state realization is defined as:

$$y_n = \begin{Bmatrix} m \\ u_n \\ g_n \end{Bmatrix} \in R^{N_m+N_u+N_g} \quad \text{.....(8.01)}$$

[4] Part of this chapter is reprinted with permission from "Chai, Z., Tang, H., He, Y., Killough, J., & Wang, Y. Uncertainty Quantification of the Fracture Network with a Novel Fractured Reservoir Forward Model." Copyright [2018] by Society of Petroleum Engineers.

where: y_n is the model-state at time step n, m is the model parameters at this time step, u_n is the state variable for the grid blocks, such as pressure, saturation, etc., and g_n is the well data at time step n. In the forecasting stage, reservoir simulation is performed from time step $n-1$ to time step n:

$$y_n{}^{f,i} = F\left(y_{n-1}{}^{a,i}\right) \quad (8.02)$$

In the assimilation step, the model-state is computed as:

$$Y_n{}^{a} = Y_n{}^{f} + K_n\left(d_n - HY_n{}^{f}\right) \quad (8.03)$$

where: K_n is the Kalman gain matrix at time step n, and Y_n is the matrix form of y_n for all cases in the ensemble. The Kalman gain can be estimated from the ensemble by:

$$K_n = P_n{}^{f} H^T \left(HP_n{}^{f} H^T + R\right)^{-1} \quad (8.04)$$

$$\langle y_n{}^{f} \rangle = \frac{1}{N_e} \sum_{i=1}^{N_e} y_n{}^{f,i} \quad (8.05)$$

$$P_n{}^{f} = \frac{1}{N_e - 1} \sum_{i=1}^{N_e} \left[\left(y_n{}^{f,i} - \langle y_n{}^{f} \rangle\right)\left(y_n{}^{f,i} - \langle y_n{}^{f} \rangle\right)^T\right] \quad (8.06)$$

H is a conversion matrix to retrieve g_n from y_n, with elements of only 0 and 1, and R is the covariance matrix of the observation errors. With the cEDFM approach, when applying EnKF, reservoir model needs to be recreated when parameters are updated, because the grid of the model is different at each step. The state variables in the matrix grids can be mapped from the previous time step easily if there is no fracture at this location. However, when fracture exists, and the grid is split, a volumetric average can be first calculated for all state variables. The obtained value is then assigned to the new grid (if there is no fracture in the next time step) or sub-grids (if fracture still presents in the next time step but with different parameter values). For the fracture grid blocks, the state variables need to be estimated, either by averaging the property from the current fracture

grid cells, or by interpolating from the parent matrix grid blocks. However, due to the complexity of the model and the associated computational time for mapping the state variables, it is more practical to rerun the simulation from time 0 at each of the forecasting time steps instead. Therefore, the model-state variables for all the following cases are calculated as:

$$y_n{}^{f,i} = F\left(y_0{}^{a,i}\right) \quad \text{.....(8.07)}$$

where: F is the reservoir simulation from time step 0 to time step n.

8.2 Case Study

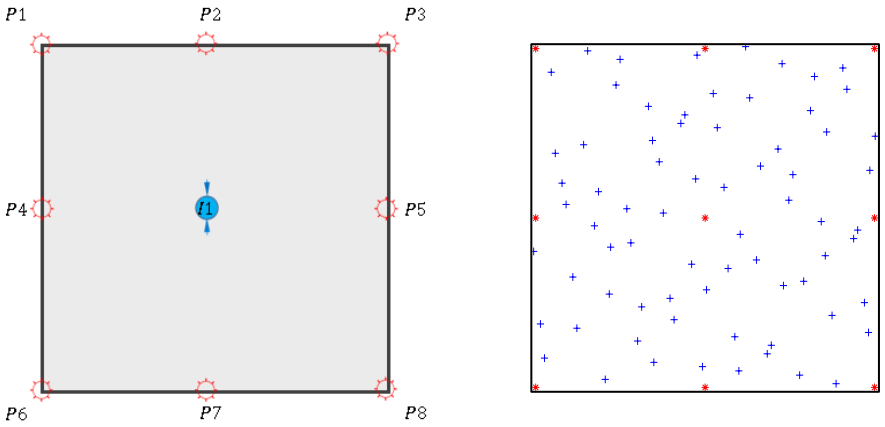

(a) Well location (b) Point-set

Figure 8.1—History matching case: 9-spot well pattern with 1 injector at the center.

8.2.1 Model Parameterization

Here a water flooding case with a 9-spot well pattern is used to illustrate the history matching process with the cEDFM approach. One injection well injects water at a constant BHP of 7000 psi. The rest of the 8 production wells produces oil at a constant BHP of 2500 psi. The wells are as shown in **Figure 8.1 (a)**. For this problem, a vectorized level-set approach is used to describe the distribution of the fractures (both high conductivity flow path and low conductivity

flow barriers). First, a set of quasi-random points is generated with the Halton sequence, as can be seen in **Figure 8.1 (b)**. The use of quasi-random points generally ensures a better coverage of the reservoir domain compared to randomly generated points, as discussed in the work of Ping, J., & Zhang, D. (2013). The well locations are also included in the point-set, as shown in red.

Table 8.1—Reservoir parameters for the history matching case.

ϕ	0.10
k_{matrix}	$5\ md$
$k_{fracture}$	$1 \times 10^{3} md$
$w_{fracture}$	$0.05\ ft$
$k_{barrier}$	$1 \times 10^{-8} md$
$w_{barrier}$	$0.05\ ft$
BHP_{inj}	7000 psi
BHP_{prd}	2500 psi
Pi	5000 psi
T	$100\ F^{o}$
$Reservoir\ composition$	$100\%\ hexane$
Mesh	51×51
Grid Size	30 ft
Reservoir Thickness	50 ft

Each of the nodes is considered as a candidate location that a fracture might pass through. At each of the nodes, the following parameters are defined:

1) The level-set function ψ.
    - ✓ If ≤ 0 : A fracture exists that pass through this node.
    - ✓ If > 0 : No fracture pass through this node.
2) The angle of the fracture θ, $\theta \in [0,180)$.

3) The length of the fracture l.

4) The percentage of the fracture length at two sides of the node.

A node-set size of 80 and an ensemble size of 80 is chosen here for the illustration case. 8 months of production data are used as the observed data, resampled with total time steps of 24. Two cases are tested: Case I has two intersecting high conductivity fracture as the flow path, connecting the injector to two producers at the top corners; Case II has a low conductivity flow barrier in the reservoir that alters the water cut behavior for some of the nearby wells at the bottom right corner. The parameters of the reservoir model are listed in **Table 8.1**.

8.2.2 Case I: Locating Highly Conductive Fractures

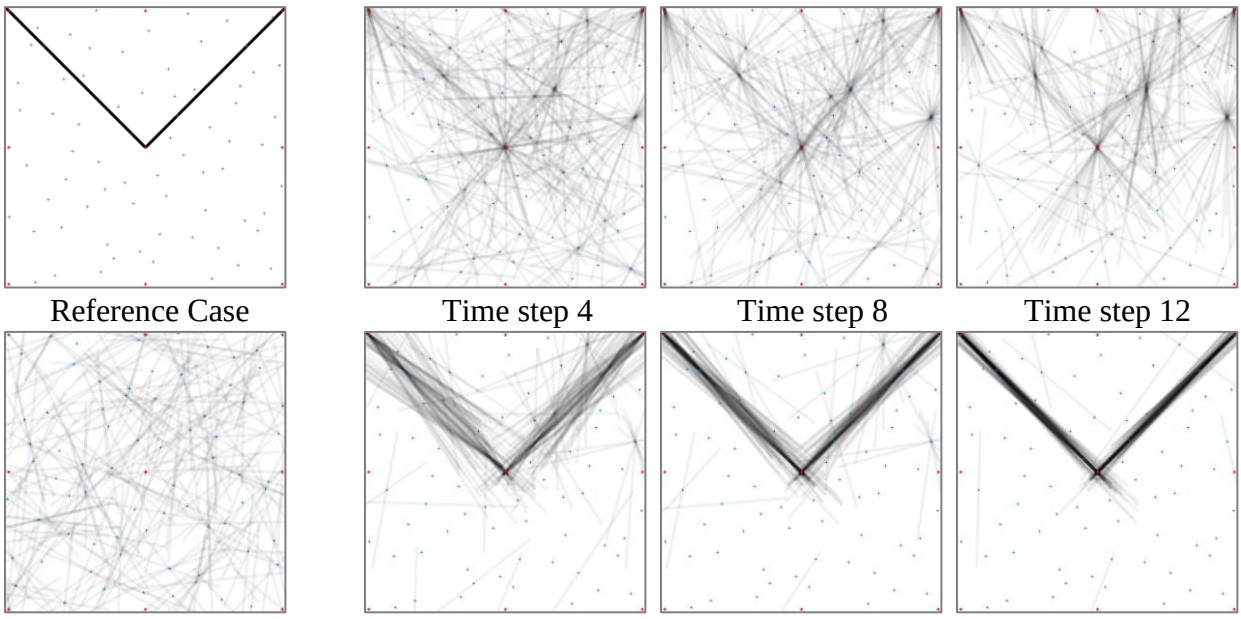

Figure 8.2—Case I: Fracture locations at different assimilation time steps of EnKF.

The top left of **Figure 8.2** shows the location of the fractures of the reference case. On the bottom left the locations of the fractures are shown at the initial time step before any updates to the parameters are made. Well locations are marked in red, while node set location are marked in blue. On the right of **Figure 8.2**, the locations of fractures are shown after different assimilation

steps of EnKF. It can be observed that the solution starts to emerge at around 16 time steps. **Figure 8.3** shows the water saturation profile at different assimilation steps for 3 random realizations chosen from the ensemble. All 3 cases eventually converges to the solution, and the saturation profile generally matches that of the reference case. The history matching result is able to capture the locations of the fracture, and an improved match is obtained for the production rate curves, especially for water production. However, the uncertainty is still obvious among different cases within the ensemble, as shown in **Figure 8.4**.

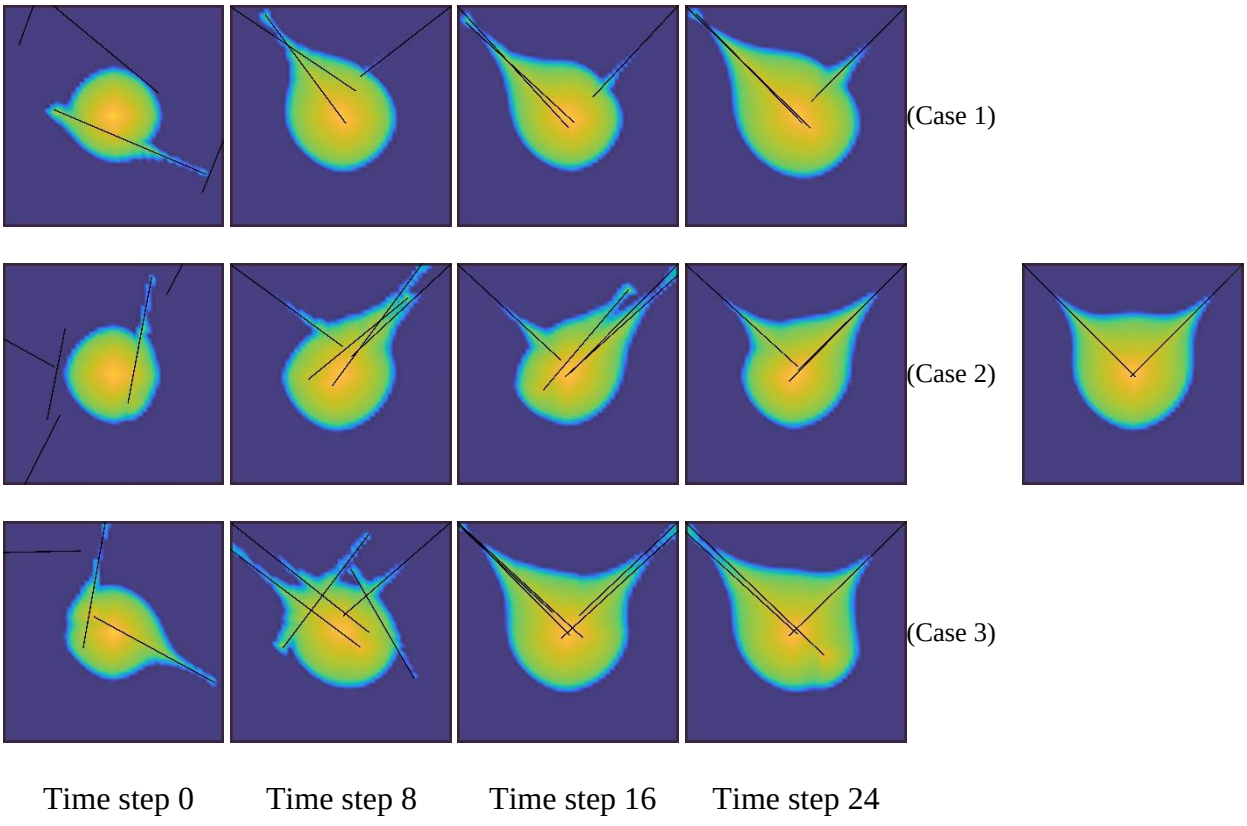

Figure 8.3—Case I: Water saturation at T=12 months for 3 random realizations in the ensemble during different assimilation steps. The reference case is shown on the right.

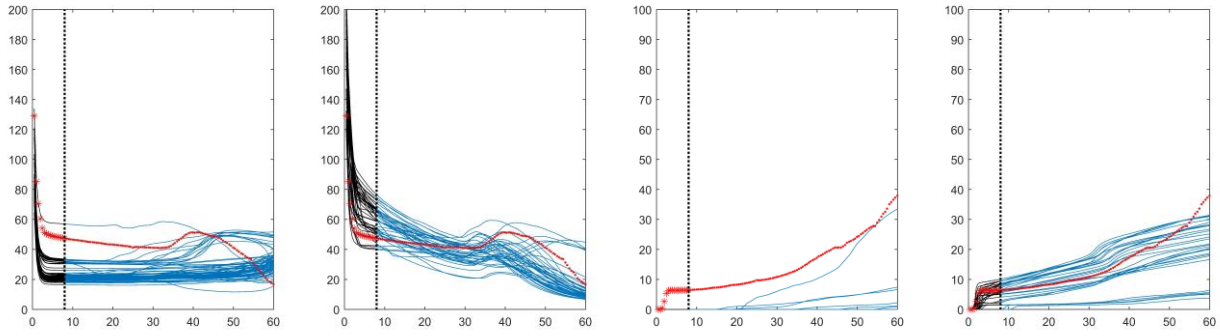

Oil Production Rate (Initial) Oil Production Rate (Updated) Water Production Rate (Initial) Water Production Rate (Updated)

(a) P-1(BBL/Day)

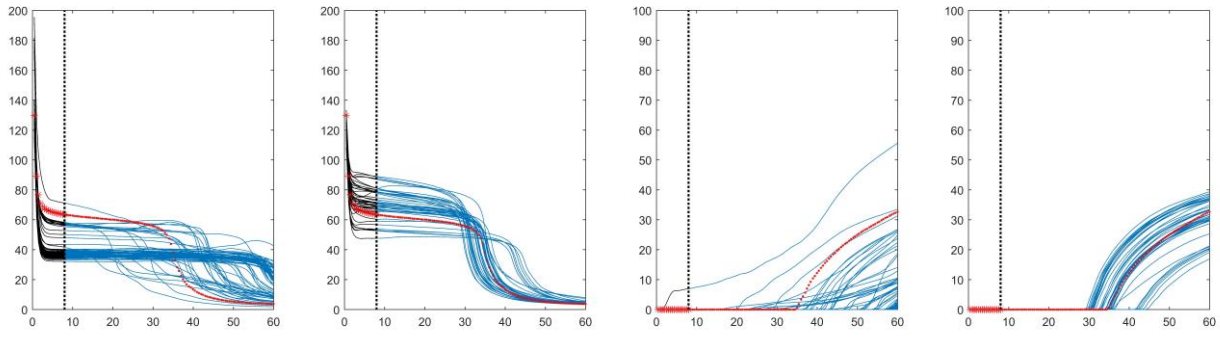

Oil Production Rate (Initial) Oil Production Rate (Updated) Water Production Rate (Initial) Water Production Rate (Updated)

(b) P-2(BBL/Day)

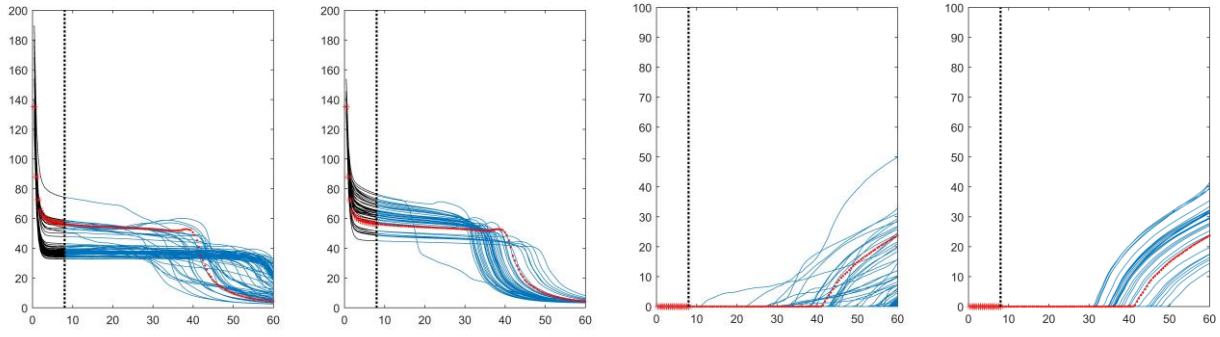

Oil Production Rate (Initial) Oil Production Rate (Updated) Water Production Rate (Initial) Water Production Rate (Updated)

(c) P-7(BBL/Day)

Figure 8.4—Case I: Oil and water production rate before and after history matching. Initial results are shown on the left, and the results afterward are shown on the right. The first 8 months of data are used for history matching, shown in red; model prediction results are shown in blue.

8.2.3 Case II: Locating Impermeable Flow Barriers

In the second case, we try to take advantage of the cEDFM approach and locate the flow barriers within the reservoir due to its improved accuracy for such cases. The reference case can be seen on the upper left of **Figure 8.5**, one flow barrier is separating the injector from 3 of the producers at the bottom right corner. The result after different assimilation time steps for the ensemble is plotted on the right.

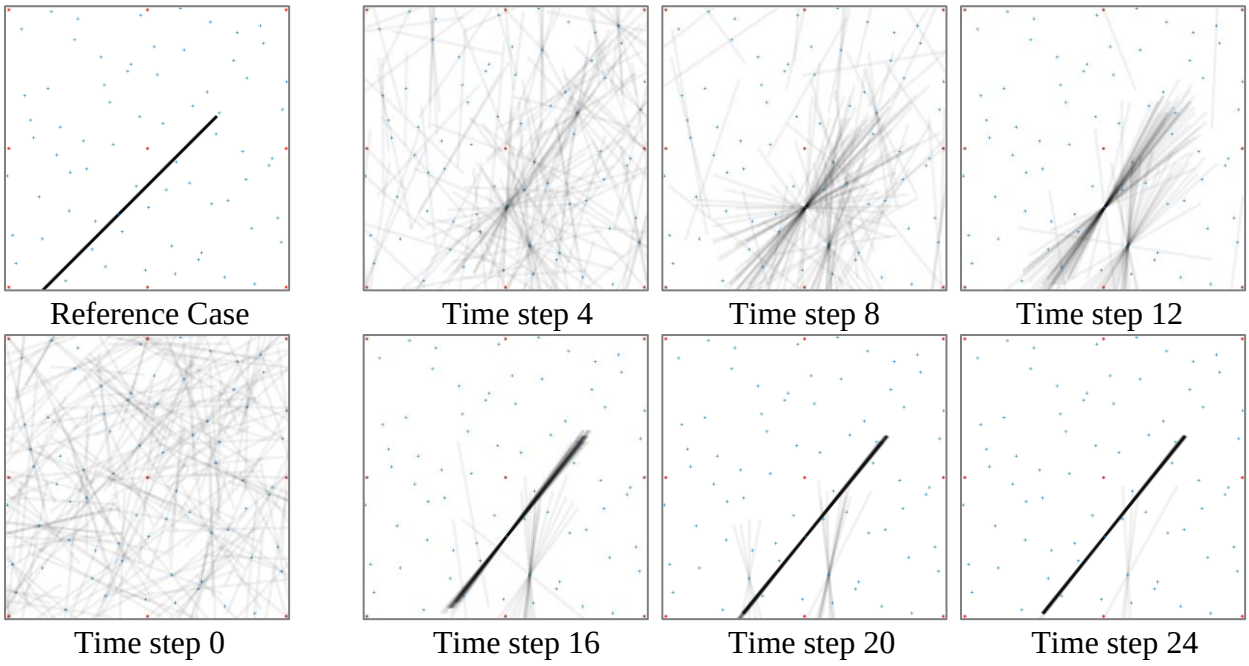

Figure 8.5—Case II: Fracture locations at different assimilation time steps of EnKF.

We can see that a solution can be found with around 12 assimilation steps. Due to the significant sensitivity of the water cut to the location of the flow barriers, this case converges faster than that of case I with highly conductive fractures. From the result at time step 24, we can see the result is much more uniform than case I. As for case I, multiple solutions exist that reaches a similar accuracy.

Figure 8.5 shows the results at different assimilation steps for 3 randomly chosen realizations from the ensemble. The uncertainty is greatly reduced compared to the initial step, as can be seen from **Figure 8.7**. Note that the match of P2 and P5 are better than that of P7, because the production data of the first 8 months are not quite adequate to fully resolve the uncertainty near P7. In general, by using the aforementioned parameterization approach and cEDFM as the forward model, the workflow is able to obtain a good match with the observed data.

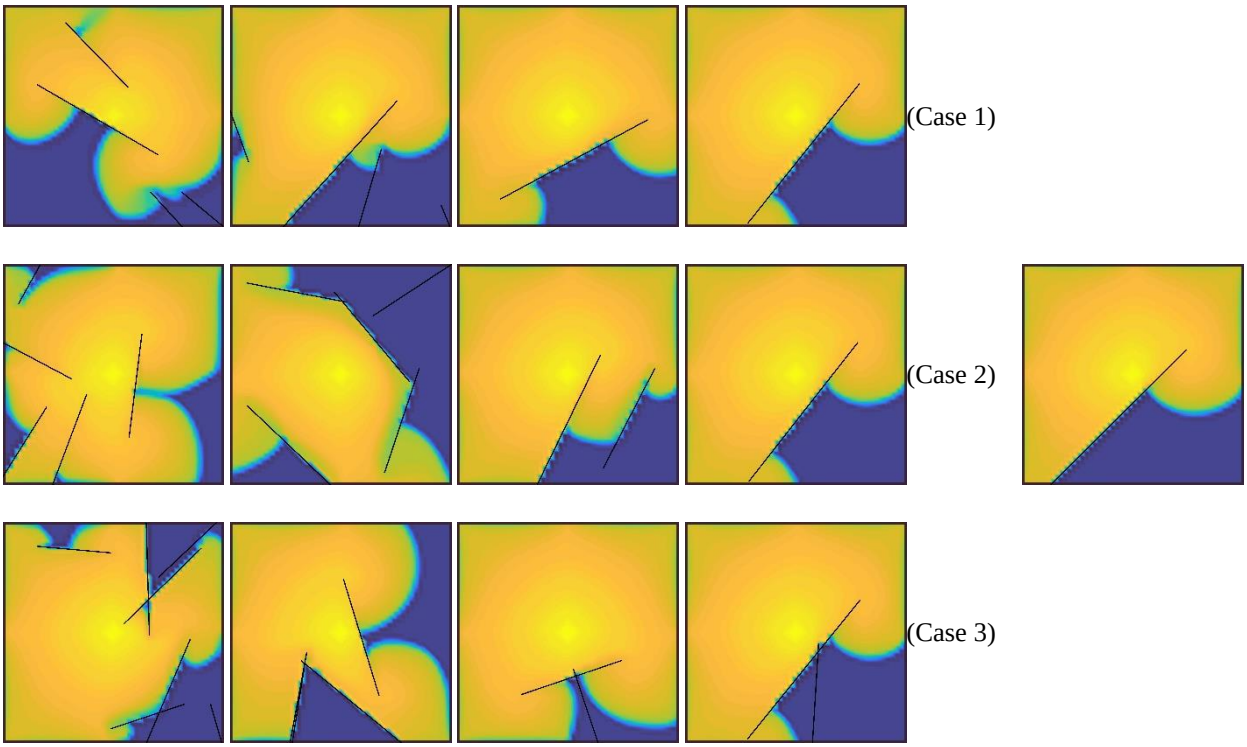

Figure 8.6—Case II: Water saturation at T=12 months for 3 random cases in the ensemble during different assimilation steps. The reference case is shown on the right.

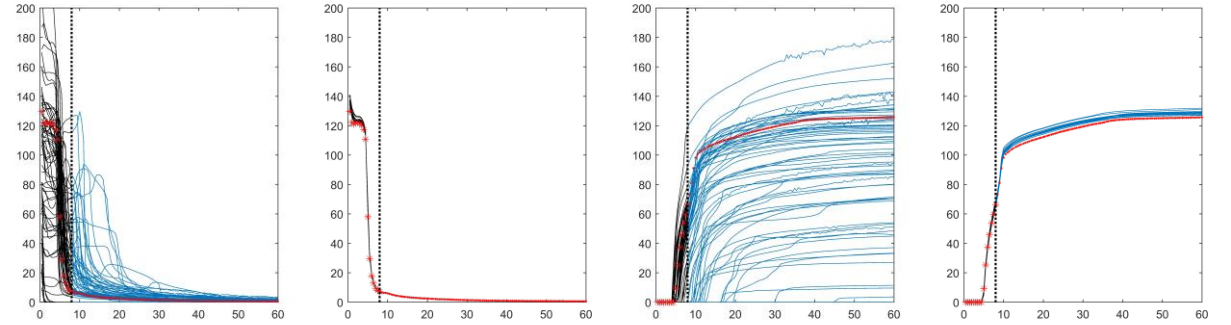

Oil Production Rate (Initial) Oil Production Rate (Updated) Water Production Rate (Initial) Water Production Rate (Updated)

(a) P-2(BBL/Day)

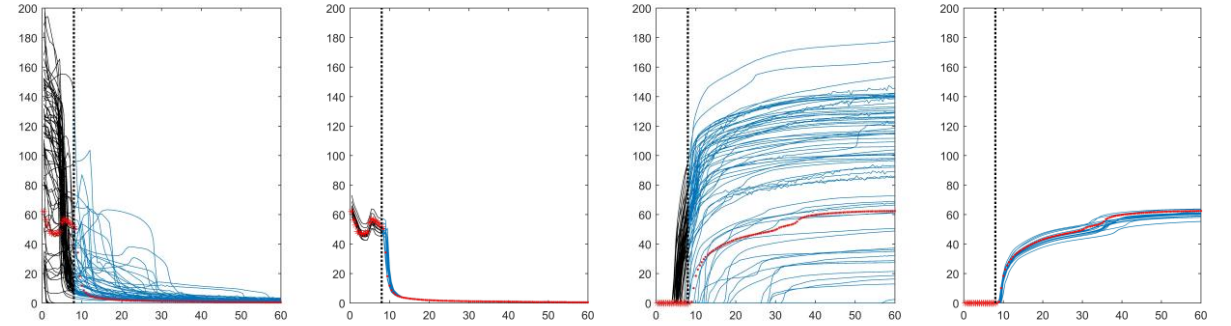

Oil Production Rate (Initial) Oil Production Rate (Updated) Water Production Rate (Initial) Water Production Rate (Updated)

(b) P-5(BBL/Day)

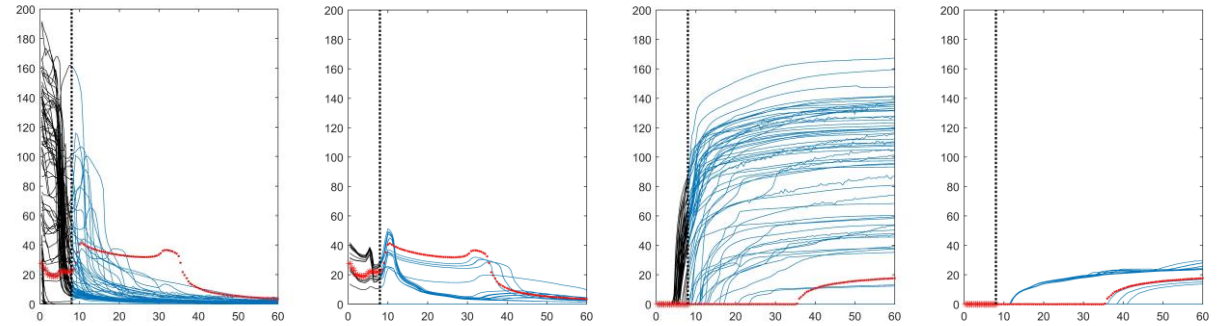

Oil Production Rate (Initial) Oil Production Rate (Updated) Water Production Rate (Initial) Water Production Rate (Updated)

(c) P-7(BBL/Day)

Figure 8.7—Case II: Oil production rate before and after history matching. Initial results are shown on the left, and the results afterward are shown on the right. The first 8 months of data are used for history matching, shown in red; model prediction results are shown in blue.

8.3 Summary

In this chapter, the cEDFM model is incorporated into the EnKF workflow to history match the fracture distribution of the reservoir. A vectorized level-set method is used for the parameterization of the problem. The explicit model can be used directly in history matching without the need of upscaling. Therefore, the validity of Gaussian distribution for the parameters can be maintained, which is a prerequisite for algorithms such as EnKF. Some results are obtained from the numerical examples, including:

1) The cEDFM approach is robust and accurate to be used in reservoir history matching. The two cases indicate that this method is capable to locate the fractures (or flow barriers) efficiently, and the result of history matching obtains good accuracy compared to the reference case.
2) The proposed history matching workflow works for complex cases with a large number of model parameters. For the two illustration cases, 80 candidate nodes are selected with 4 parameters defined for each of the nodes. Therefore, the model has 320 parameters in total. The two reference cases are relatively simple, however as long as the well data can resolve more complex reservoir attributes, the approach would still work. The limitation lies in the inherent characteristics of most history matching problems that under many cases, the observed data cannot fully resolve some of the uncertainties of the reservoir.
3) The history matching case to characterize flow barriers shows a faster convergence and higher confidence compared to the case to characterize highly conductive fractures. This is because flow barriers has a much more definitive influence to the well production behavior, while for highly conductive fractures, multiple solutions might exist that lead to the same result.

CHAPTER IX

DISCUSSIONS & CONCLUSIONS

Modeling and history matching of fractured shale reservoirs have been proved to be challenging due to the complexity of the reservoir and the high computational cost. Special discretization approaches are needed to accurately simulate the effect of different porosity types, especially large-scale fractures, on the production of shale reservoirs. In this work, we developed the cEDFM approach based on the original EDFM concept. It is incorporated with multiple-porosity model to provide a comprehensive approach to simulate fractured shale reservoirs. The two approaches complement each other so that the mass transfer in hydraulic fractures and large-scale natural fractures can be addressed with comparable accuracy as traditional discrete fracture models, while the effect of micro fracture and the different flow mechanisms in shale matrix can be incorporated at the same time. The cEDFM formulation is partially inherited from the original EDFM concept, and LGR near the fractures can be avoided. By performing grid splitting, the cEDFM model obtained improved accuracy compared to the original EDFM approach. The proposed model is validated with fine explicit models and the PEBI model for single-phase and multi-phase flow problems. Compared to the original EDFM, the new model has several advantages, including:

1) Improved accuracy for flow across fractures, especially for low permeable flow barriers; the model shows a more consistent accuracy, even for multi-phase flow problems.
2) The new model is capable to be incorporated into methods such as streamline simulation, while the original EDFM is not compatible with such approaches;
3) The cEDFM model is extended to work with corner point grid blocks to improve the applicability of this method in the field;

4) The original EDFM is restricted by a constant refinement level of the mesh. Here in the proposed model, local grid coarsening is implemented for areas without fractures to further reduce the computational cost.

This model enables the parameters of macro fractures such as strike angle and conductivity to be directly set as history matching parameters, so that the history matching process can be fully automatic. Most existing work on fractured reservoir history matching relies on an upscaling process to transfer the properties of fractures to a dual-porosity type of model, which makes the probability density distribution of parameters non-Gaussian. In this work, no upscaling is necessary to build the reservoir model for simulation, therefore the adequacy to use Gaussian distribution for the fracture parameters is ensured. Two history matching algorithms are implemented with cEDFM as the forward model: the modified two-stage MCMC with a flow proxy, as well as the EnKF algorithm. Through this part of the study, we learned that:

5) The modified two-stage MCMC algorithm can effectively obtain a better match, and the uncertainty of the parameter can be greatly reduced. However, the application is somewhat constraint by the number of parameters. Since a proxy model is used, it is more suited for cases with a smaller number of parameters.
6) The EnKF workflow works well with cEDFM to obtain a much-improved history matching result for more complex problems. The illustration cases have shown that the algorithm can locate the fractures, especially when it forms flow barriers. A relatively large parameter space around a couple of hundred can be solved without much problem.

REFERENCES

Aarseth, E. S., Bourgine, B., Castaing, C., Chiles, J. P., Christensen, N. P., Eeles, M., ... & Jørgensen, K. Z. (1997). Interim guide to fracture interpretation and flow modelling in fractured reservoirs. European Commision Eur 17116 En, 1-203.

Ahmed Elfeel, M., Jamal, S., Enemanna, C., Arnold, D., & Geiger, S. (2013, June). Effect of DFN upscaling on history matching and prediction of naturally fractured reservoirs. In EAGE Annual Conference & Exhibition incorporating SPE Europec. Society of Petroleum Engineers.

Ambrose, R. J., Hartman, R. C., Diaz Campos, M., Akkutlu, I. Y., & Sondergeld, C. (2010, January). New pore-scale considerations for shale gas in place calculations. In SPE Unconventional Gas Conference. Society of Petroleum Engineers.

Blaskovich, F. T., Cain, G. M., Sonier, F., Waldren, D., & Webb, S. J. (1983, January). A multicomponent isothermal system for efficient reservoir simulation. In Middle East Oil Technical Conference and Exhibition. Society of Petroleum Engineers.

Bonet-Cunha, L., Oliver, D. S., Redner, R. A., & Reynolds, A. C. (1998, September). A hybrid Markov chain Monte Carlo method for generating permeability fields conditioned to multiwell pressure data and prior information. SPE Journal, 3(03), 261-271. Society of Petroleum Engineers.

Cao, Y., Yan, B., Alfi, M., & Killough, J. E. (2015, September). A novel compositional model of simulating fluid flow in shale reservoirs-some preliminary tests and results. In SPE Reservoir Characterization and Simulation Conference and Exhibition. Society of Petroleum Engineers.

Chai, Z., Yan, B., Killough, J. E., & Wang, Y. (2018, October). An efficient method for fractured shale reservoir history matching: The embedded discrete fracture multi-continuum approach. Journal of Petroleum Science and Engineering, 160, 170-181.

Chai, Z., Yan, B., Killough, J. E., & Wang, Y. (2016, November). Dynamic embedded discrete fracture multi-continuum model for the simulation of fractured shale reservoirs. In International Petroleum Technology Conference.

Chai, Z., Tang, H., He, Y., Killough, J., & Wang, Y. (2018, September). Uncertainty quantification of the fracture network with a novel fractured reservoir forward model. In SPE Annual Technical Conference and Exhibition. Society of Petroleum Engineers.

Chen, Y., & Oliver, D. S. (2013, May). Levenberg–Marquardt forms of the iterative ensemble smoother for efficient history matching and uncertainty quantification. Computational Geosciences, 17(4), 689-703.

Coats, K. H. (1989, January). Implicit compositional simulation of single-porosity and dual-porosity reservoirs. In SPE Symposium on Reservoir Simulation. Society of Petroleum Engineers.

Dean, R. H., & Lo, L. L. (1988, May). Simulations of naturally fractured reservoirs. SPE Reservoir Engineering, 3(02), 638-648. Society of Petroleum Engineers.

Ding, D. Y., Farah, N., Bourbiaux, B., Wu, Y. S., & Mestiri, I. (2018, August). Simulation of matrix/fracture interaction in low-permeability fractured unconventional reservoirs. SPE Journal. Society of Petroleum Engineers.

El Sgher, M., Aminian, K., & Ameri, S. (2018, January). The impact of stress on propped fracture conductivity and gas recovery in Marcellus shale. In SPE Hydraulic Fracturing Technology Conference and Exhibition. Society of Petroleum Engineers.

Evensen, G. (2003, May). The ensemble Kalman filter: Theoretical formulation and practical implementation. Ocean dynamics, 53(4), 343-367.

Gale, J. F., Laubach, S. E., Olson, J. E., Eichhubl, P., & Fall, A. (2014, August). Natural fractures in shale: A review and new observations. AAPG Bulletin, 98(11), 2165-2216.

Gang, T., & Kelkar, M. G. (2006, January). Efficient history matching in naturally fractured reservoirs. In SPE/DOE Symposium on Improved Oil Recovery. Society of Petroleum Engineers.

Gillespie, P. A., Howard, C. B., Walsh, J. J., & Watterson, J. (1993, January). Measurement and characterisation of spatial distributions of fractures. Tectonophysics, 226(1-4), 113-141.

Heinemann, Z. E., Brand, C., Munka, M., & Chen, Y. M. (1989, January). Modeling reservoir geometry with irregular grids. In SPE Symposium on Reservoir Simulation. Society of Petroleum Engineers.

Hill, A. C., & Thomas, G. W. (1985, January). A new approach for simulating complex fractured reservoirs. In Middle East Oil Technical Conference and Exhibition. Society of Petroleum Engineers.

Hinkley, R., Gu, Z., Wong, T., & Camilleri, D. (2013, November). Multi-porosity simulation of unconventional reservoirs. In SPE Unconventional Resources Conference Canada. Society of Petroleum Engineers.

Jiang, J., & Younis, R. M. (2016, June). Hybrid coupled discrete-fracture/matrix and multicontinuum models for unconventional-reservoir simulation. SPE Journal, 21(03), 1-009. Society of Petroleum Engineers.

Karimi-Fard, M., Durlofsky, L. J., & Aziz, K. (2004, June). An efficient discrete fracture model applicable for general purpose reservoir simulators. Society of Petroleum Engineers.

Kazemi, H., Gilman, J. R., & Elsharkawy, A. M. (1992, May). Analytical and numerical solution of oil recovery from fractured reservoirs with empirical transfer functions (includes associated papers 25528 and 25818). SPE Reservoir Engineering, 7(02), 219-227. Society of Petroleum Engineers.

Kazemi, H., Merrill, L. S., Porterfield, K. L., & Zeman, P. R. (1976, December). Numerical simulation of water-oil flow in naturally fractured reservoirs. Society of Petroleum Engineers.

Lee, S. H., Jensen, C. L., & Lough, M. F. (2000, September). Efficient finite-difference model for flow in a reservoir with multiple length-scale fractures. Society of Petroleum Engineers.

Li, L., & Lee, S. H. (2008, August). Efficient field-scale simulation of black oil in a naturally fractured reservoir through discrete fracture networks and homogenized media. Society of Petroleum Engineers.

Li, R., Reynolds, A. C., & Oliver, D. S. (2001, January). History matching of three-phase flow production data. In SPE reservoir simulation symposium. Society of Petroleum Engineers.

Lim, K. T., & Aziz, K. (1994, November). Matrix-fracture transfer shape factors for dual-porosity simulators. Journal of Petroleum Science and Engineering, 13(3-4), 169-178.

Lu, L., & Zhang, D. (2015, October). Assisted history matching for fractured reservoirs by use of Hough-transform-based parameterization. SPE Journal, 20(05), 942-961. Society of Petroleum Engineers.

Ma, X., Al-Harbi, M., Datta-Gupta, A., & Efendiev, Y. (2008, March). An efficient two-stage sampling method for uncertainty quantification in history matching geological models. SPE Journal, 13(01), 77-87. Society of Petroleum Engineers.

Moinfar, A., Varavei, A., Sepehrnoori, K., & Johns, R. T. (2014, April). Development of an efficient embedded discrete fracture model for 3d compositional reservoir simulation in fractured reservoirs. Society of Petroleum Engineers.

Mustapha, H. (2014, September). A Gabriel-Delaunay triangulation of 2D complex fractured media for multiphase flow simulations. Computational Geosciences, 18(6), 989-1008.

Nejadi, S., Leung, J. Y. W., Trivedi, J. J., & Virues, C. J. J. (2014, September). Integrated characterization of hydraulically fractured shale gas reservoirs production history matching. Society of Petroleum Engineers.

Nelson, R. (2001). Geologic analysis of naturally fractured reservoirs. Elsevier.

Odling, N. E., Gillespie, P., Bourgine, B., Castaing, C., Chiles, J. P., Christensen, N. P., ... & Trice, R. (1999, November). Variations in fracture system geometry and their implications for fluid flow in fractures hydrocarbon reservoirs. Petroleum Geoscience, 5(4), 373-384.

Oliver, D. S., & Chen, Y. (2010, July). Recent progress on reservoir history matching: a review. Computational Geosciences, 15(1), 185-221.

Oliver, D. S., Cunha, L. B., & Reynolds, A. C. (1997, March). Markov chain Monte Carlo methods for conditioning a permeability field to pressure data. Mathematical Geology, 29(1), 61-91.

Ouenes, A., Brefort, B., Meunier, G., & Dupere, S. (1993, January). A new algorithm for automatic history matching: application of simulated annealing method (SAM) to reservoir inverse modeling. Society of Petroleum Engineers.

Ouillon, G., Castaing, C., & Sornette, D. (1996, March). Hierarchical geometry of faulting. Journal of Geophysical Research: Solid Earth, 101(B3), 5477-5487.

Ping, J., Al-Hinai, O., & Wheeler, M. F. (2017, August). Data assimilation method for fractured reservoirs using mimetic finite differences and ensemble Kalman filter. Computational Geosciences, 21(4), 781-794.

Ping, J., & Zhang, D. (2013, August). History matching of fracture distributions by ensemble Kalman filter combined with vector based level set parameterization. Journal of Petroleum Science and Engineering, 108, 288-303.

Pruess, K. & Narasimhan, T.N. (1985, February). A practical method for modeling fluid and heat flow in fractured porous media. Society of Petroleum Engineers.

Sarda, S., Jeannin, L., Basquet, R., & Bourbiaux, B. (2002, April). Hydraulic characterization of fractured reservoirs: simulation on discrete fracture models. Society of Petroleum Engineers.

Sandve, T. H., Berre, I., & Nordbotten, J. M. (2012, May). An efficient multi-point flux approximation method for discrete fracture-matrix simulations. Journal of Computational Physics, 231, 3784–3800.

Schulze-Riegert, R. W., Axmann, J. K., Haase, O., Rian, D. T., & You, Y.-L. (2002, April). Evolutionary algorithms applied to history matching of complex reservoirs. Society of Petroleum Engineers.

Sondergeld, C. H., Ambrose, R. J., Rai, C. S., & Moncrieff, J. (2010, January). Micro-structural studies of gas shales. In SPE Unconventional Gas Conference. Society of Petroleum Engineers.

Suarez-Rivera, R., Burghardt, J., Edelman, E., Stanchits, S., & Surdi, A. (2013, January). Geomechanics considerations for hydraulic fracture productivity. In 47th US Rock Mechanics/Geomechanics Symposium. American Rock Mechanics Association.

Sun, J., & Schechter, D. S. (2014, October). Optimization-based unstructured meshing algorithms for simulation of hydraulically and naturally fractured reservoirs with variable distribution of fracture aperture, spacing, length and strike. In SPE Annual Technical Conference and Exhibition. Society of Petroleum Engineers.

Ţene, M., Bosma, S. B., Al Kobaisi, M. S., & Hajibeygi, H. (2017, May). Projection-based embedded discrete fracture model (pEDFM). Advances in Water Resources, 105, 205-216.

Wang, F. P., & Reed, R. M. (2009, January). Pore networks and fluid flow in gas shales. In SPE Annual Technical Conference and Exhibition. Society of Petroleum Engineers.

Warren, J. E., & Root, P. J. (1963, September). The behavior of naturally fractured reservoirs. Society of Petroleum Engineers.

Wu, Y.-S., & Pruess, K. (1988, February). A multiple-porosity method for simulation of naturally fractured petroleum reservoirs. Society of Petroleum Engineers.

Wu, Z., Reynolds, A. C., & Oliver, D. S. (1998, January). Conditioning geostatistical models to two-phase production data. In SPE Annual Technical Conference and Exhibition. Society of Petroleum Engineers.

Yan, B., Alfi, M., An, C., Cao, Y., Wang, Y., & Killough, J. E. (2016, June). General multi-porosity simulation for fractured reservoir modeling. Journal of Natural Gas Science and Engineering, 33, 777-791.

Yan, B., Wang, Y., & Killough, J. E. (2013, February). Beyond dual-porosity modeling for the simulation of complex flow mechanisms in shale reservoirs. In SPE Reservoir Simulation Symposium. Society of Petroleum Engineers.

Yan, B. (2017). Development of general unstructured reservoir utility and fractured reservoir modeling. Doctoral dissertation, Texas A & M University.

Yang, D., Xue, X., & Chen, J. (2018, April). High resolution hydraulic fracture network modeling using flexible dual porosity dual permeability framework. Society of Petroleum Engineers.

Zhang, J., Kamenov, A., Hill, A. D., & Zhu, D. (2014, August). Laboratory measurement of hydraulic-fracture conductivities in the Barnett shale. SPE Production & Operations, 29(03), 216-227. Society of Petroleum Engineers.